Technische Universität München
TUM School of Life Sciences

Elucidating the fate of freshly added organic matter in soils driven by the microtopography of soil microaggregates

Tianyi Wu

Vollständiger Abdruck der von der TUM School of Life Sciences

der Technischen Universität München zur Erlangung einer

Doktorin der Naturwissenschaften (Dr. rer. nat.)

genehmigten Dissertation.

Vorsitz: Prof. Dr. Jörg Völkel

Prüfende der Dissertation:
1. Prof. Dr. Dr. h.c. Ingrid Kögel-Knabner
2. Prof. Dr. Carsten W. Müller

Die Dissertation wurde am 13. September 2024 bei der Technischen Universität München eingereicht und durch die TUM School of Life Sciences am 27. Januar 2025 angenommen.

I. Summary

The three-dimensional (3D) structure of soil plays a fundamental role in the turnover and storage of soil organic matter (SOM), which is the basis for various ecological soil functions. Microaggregates, soil aggregates smaller than 250 μm, are particularly important in SOM sequestration as they harbor large amounts of mineral-associated organic matter (MAOM) with long turnover times. However, our understanding of OM stabilization within the submicron scale of soil aggregates remains limited due to technological constraints. Conventional analytical methods typically lack either spatial or mass resolution (e.g., IRMS, SEM), hindering further exploration in this area.

The main objective of this thesis was to overall understand the organic matter (OM) sequestration process in soil from bulk to submicron scale.

For agriculture soils, plant litter is the main above-ground OM input with a complex composition. To study the OM sequestration in the soil microstructure, the study went from simple compounds, low-molecular-weight organic compounds (LMWOC) amendment, to complex OM, plant residues, as added OM. The incubation experiments were designed to investigate rapid and 90-day OM sequestration with microbial activities. Stable isotope labelling was used as the basic method. Soil respiration with ^{13}C signatures was monitored, IRMS analysis on soil fractions, ^{13}C compound-specific phospholipid-derived fatty acids (PLFAs), microbial necromass, and enzyme activities were determined in the bulk soil scale for the knowledge of OM sequestration in soil fractions and the C dynamic influenced by microbial activities.

Since larger scale soil functions, for instance, soil fertility and climate change, are controlled at micron or even smaller scale soil structure, revealing submicron scale OM sequestration

was an important goal. Through the combined use of two innovative techniques: Nanoscale Secondary Ion Mass Spectrometry (NanoSIMS) and Helium-based Microscopy (HIM), along with computational approaches, the 3D physical and chemical microstructure of soil aggregates involved in the sequestration of newly added plant-derived OM was elucidated.

The objectives of this thesis were approached through the following projects:

1. Rapid low molecular weight organic compounds (LMWOC) retention in soil MAOM pool. Study 1

Initial soil organic matter (SOM) content, also known as SOM legacy, reflects agriculture soil management and can play a role in newly added OM sequestration. Considering the impact of soil mineralogy and initial SOM content on OM sequestration, two soils with the same mineralogy with different OM content were employed in the first incubation experiment. Two isotope labelled LMWOC (^{13}C labelled D-glucose and ^{13}C and ^{15}N labelled amino acid mixture) were added to soils for a 24 h incubation. Density fractionation was applied to post-incubated soil samples to obtain clay and fine silt-sized fraction. Bulk soil IRMS results demonstrated that smaller size fractions contained a higher amount of added OM, which is due to the larger specific surface area. Soil initial OM loading, which reflects the soil organic carbon (SOC) saturation level, had the main influence on OM retention. Soil low in C was more efficient in retaining added OM than soil with a higher MAOM-C saturation level. The N content of added OM enhanced C recovery, especially in soil with initial low OM content. This innovative approach sheds light on the complex interplay between soil properties and OM sequestration, offering valuable insights for sustainable soil management practices.

2. C turnover in soils and the influence of microbial activities. Study 2

Based on the findings of Study 1, to further understand the fate of OM with different C/N ratios influenced by soil inherit OM legacy, an incubation experiment was conducted using ^{13}C and ^{15}N labeled plant litters vary in C/N ratio as OM input and soils with an C gradient. Gas IRMS was used to measure soil respiration together with isotope information. Although soil with higher OM content was expected to have a higher cumulative CO_2-C respiration, this high value was found in soil with lower C content after amending plant litter. This indicated a more vulnerable OM in SOM-depleted soil. The ^{13}C PLFA, enzyme vectors, and microbial necromass were measured for post-incubated samples. The results demonstrated that with the increase of SOC content, thus C saturation level, plant litter amendments resulted in a less increase of fungi-to-bacteria (F/B) ratio and decreased necromass to SOC ratio. Plant litter with higher N content benefited bacteria over fungi and retained more efficiently in soil. This approach has unveiled unexpected dynamics in soil carbon cycling, highlighting the intricate relationship between SOM content, microbial communities, and plant litter decomposition.

3. 4D presentation of soil microaggregate: OM sequestration on the 3D microstructure of soil aggregates. Study 3

With a better overall understanding of OM sequestration of freshly added simply OM compounds and more complex plant litters, the study moved forward to elucidate the submicron scale OM sequestration as it controls the larger scale soil functions. In this study, soil aggregate fractions were derived from the incubation experiment in Study 2. The dry sieving method was used to separate soil aggregates into three-size fractions. The conventional IRMS measurement showed that soil microaggregates (< 53 μm and 53-250 μm) retained a higher amount of plant-derived OM than macroaggregates (> 250 μm). Smaller soil microaggregates (< 53 μm) from 6 treatments (3 soils with a OM content gradient × 2 plant litters with different C/N ratios) were measured by NanoSIMS and HIM. For this, they were

stabilized on the GaAs wafers with a liquid-free sample preparation method, which maintained the original structure of the microaggregates as much as possible. The relationship between OM and inorganic elements distribution was analyzed using a NanoSIMS instrument with Cs^+ and O^- source, respectively.

The secondary electron (SE) images obtained by HIM were used to construct a 3D architecture of soil microaggregates at sub-µm resolution and to analyze the incidence angle of the surface. This process was based on the computational approaches established in the co-authored study (Study 4). The OM distribution was aligned to the 3D reconstruction, which formed a 4D presentation of a soil microaggregate. The NanoSIMS and HIM results demonstrated that newly formed OM preferentially sequestered at the surface with an incidence angle of 44.60° ± 23.25. The 4D imaging approach allowed direct observation of MAOM on soil microaggregate surfaces at submicron resolution. This study demonstrated that the µm scale architecture of soil microaggregates directly affects the association of OM, and thus presumably determines the fate of fresh OM together with the persistence of MAOM.

This thesis provided a deeper understanding of OM sequestration and C dynamic in soils, spanning from bulk soil to submicron-scale level. 4D reconstruction of soil microaggregates elucidated the OM sequestration on soil microarchitecture and contributed to an insight into submicron scale MAOM formation.

II. Zusammenfassung

Die dreidimensionale (3D) Struktur des Bodens spielt eine grundlegende Rolle für den Umsatz und die Speicherung von organischer Bodensubstanz (SOM), welche die Basis für verschiedene ökologische Bodenfunktionen bildet. Mikroaggregate, also Bodenaggregate mit einer Größe von weniger als 250 µm, sind besonders wichtig für die Sequestrierung von SOM, da sie große Mengen an mineralassoziierter organischer Substanz (MAOM) mit langen Umsatzzeiten enthalten. Unser Verständnis der Stabilisierung von organischer Substanz im Submikronbereich von Bodenaggregaten ist jedoch aufgrund technologischer Beschränkungen weiterhin begrenzt. Herkömmliche Analysemethoden weisen in der Regel entweder eine unzureichende räumliche oder massenspektrometrische Auflösung auf (z. B. IRMS, SEM), was die Erforschung dieses Bereichs erschwert.

Ziel dieser Arbeit war es, den Prozess der Sequestrierung von organischer Substanz (OM) im Boden über verschiedene Maßstäbe hinweg zu verstehen, von der Makro- bis zur Submikron-Skala.

In landwirtschaftlich genutzten Böden ist Pflanzenstreu der wichtigste oberirdische Eintrag von OM, welcher eine komplexe Zusammensetzung aufweist. Um die Bindung von OM in der Bodenmikrostruktur zu untersuchen, ging die Studie von einfachen organischen Komponenten mit niedrigem Molekulargewicht (LMWOC) bis hin zu komplexeren organischen Substanzen wie Pflanzenresten, die als zugeführte OM dienten, aus. Die Inkubationsexperimente zielten darauf ab, sowohl die schnelle als auch die über 90 Tage erfolgende OM-Sequestrierung unter Berücksichtigung mikrobieller Aktivitäten zu untersuchen. Als grundlegende Methode wurde die Markierung mit stabilen Isotopen verwendet. Es wurden die Bodenatmung mit ^{13}C-Signaturen gemessen sowie IRMS-Analysen von Bodenfraktionen, ^{13}C-verbindungsspezifische Phospholipid-Fettsäuren (PLFAs),

mikrobielle Nekromasse und Enzymaktivitäten in der Bodenmasse durchgeführt, um die OM-Sequestrierung in Bodenfraktionen und die von mikrobiellen Aktivitäten beeinflusste Kohlenstoffdynamik zu ermitteln.

Da die Bodenfunktionen in größerem Maßstab, z. B. Bodenfruchtbarkeit und Klimawandel, durch die Bodenstruktur im Mikrometer- oder sogar noch kleineren Maßstab gesteuert werden, war es ein wichtiges Ziel, die OM-Sequestrierung im Submikrometerbereich zu untersuchen. Durch den kombinierten Einsatz von zwei innovativen Techniken – der nanoskaligen Sekundärionen-Massenspektrometrie (NanoSIMS) und der helium-basierten Mikroskopie (HIM) – sowie durch rechnerische Ansätze konnte die dreidimensionale physikalische und chemische Mikrostruktur von Bodenaggregaten, die an der Sequestrierung von neu zugeführtem pflanzlichem OM beteiligt sind, aufgeklärt werden.

Die Ziele dieser Arbeit wurden im Rahmen der folgenden Projekte verfolgt:

1. Schnelle Retention von organischen Komponenten mit niedrigem Molekulargewicht (LMWOC) im MAOM-Pool des Bodens. Studie 1

Der ursprüngliche Gehalt an organischer Substanz (SOM) im Boden, auch als SOM-Vermächtnis bekannt, spiegelt die landwirtschaftliche Bodenbewirtschaftung wider und kann eine Rolle bei der Sequestrierung neu hinzugefügter organischer Substanz (OM) spielen. Um die Auswirkungen der Bodenmineralogie und des anfänglichen SOM-Gehalts auf die OM-Sequestrierung zu untersuchen, wurden im ersten Inkubationsversuch zwei Böden mit identischer Mineralogie, jedoch unterschiedlichem OM-Gehalt verwendet. Zwei isotopenmarkierte LMWOC (^{13}C-markierte D-Glucose und ^{13}C- sowie ^{15}N-markierte Aminosäuremischung) wurden den Böden für eine 24-stündige Inkubation zugesetzt. Die nach der Inkubation entnommenen Bodenproben wurden einer Dichtefraktionierung unterzogen,

um Ton- und feine Schlufffraktionen zu isolieren. Die Ergebnisse der IRMS-Untersuchung zeigten, dass kleinere Fraktionen eine größere Menge des zugesetzten OM enthielten, was auf die größere spezifische Oberfläche zurückzuführen ist. Der anfängliche OM-Gehalt des Bodens, welcher den Sättigungsgrad des organischen Kohlenstoffs (SOC) im Boden widerspiegelt, hatte den größten Einfluss auf die OM-Retention. Böden mit niedrigem C-Gehalt waren bei der Retention des zugesetzten OM effizienter als Böden mit einem höheren MAOM-C-Sättigungsgrad. Der N-Gehalt des zugesetzten OM verbesserte die C-Rückgewinnung, insbesondere in Böden mit ursprünglich niedrigem OM-Gehalt. Dieser innovative Ansatz beleuchtet das komplexe Zusammenspiel zwischen Bodeneigenschaften und OM-Bindung und bietet wertvolle Erkenntnisse für eine nachhaltige Bodenbewirtschaftung.

2. C-Umsatz in Böden und der Einfluss der mikrobiellen Aktivitäten. Studie 2

Aufbauend auf den Ergebnissen der Studie 1 wurde ein Inkubationsexperiment mit ^{13}C- und ^{15}N-markiertem Pflanzenstreu mit unterschiedlichen C/N-Verhältnissen als OM-Eintrag sowie Böden mit einem C-Gradienten durchgeführt, um den Verbleib von OM mit unterschiedlichem C/N-Verhältnis unter dem Einfluss der SOM-Vermächtnisse besser zu verstehen. Die Bodenatmung wurde zusammen mit den Isotopeninformationen mittels Gas-IRMS gemessen. Obwohl erwartet wurde, dass Böden mit höherem OM-Gehalt eine höhere kumulative CO2-C-Atmung aufweisen, wurde dieser hohe Wert in Böden mit niedrigerem C-Gehalt nach der Beimischung von Pflanzenstreu beobachtet. Dies deutet darauf hin, dass OM in SOM-verarmten Böden anfälliger ist. Die ^{13}C-markierten Phospholipid-Fettsäuren (PLFAs), Enzymaktivitäten und mikrobiellen Nekromassen wurden in den nach der Bebrütung entnommenen Proben gemessen. Die Ergebnisse zeigten, dass mit zunehmendem SOC-Gehalt und somit einem höheren C-Sättigungsgrad die Zugabe von Pflanzenstreu zu einem geringeren Anstieg des Verhältnisses von Pilzen zu Bakterien (F/B) und einem geringeren Verhältnis von

Nekromasse zu SOC führte. Pflanzenstreu mit höherem N-Gehalt begünstigte das Wachstum von Bakterien gegenüber Pilzen und wurde effizienter im Boden gehalten. Dieser Ansatz deckte unerwartete Dynamiken im Kohlenstoffkreislauf des Bodens auf und zeigte die komplizierte Beziehung zwischen SOM-Gehalt, mikrobiellen Gemeinschaften und der Zersetzung von Pflanzenstreu.

3. 4D-Darstellung von Bodenmikroaggregaten: OM-Sequestrierung auf der 3D-Mikrostruktur von Bodenaggregaten. Studie 3

Mit einem besseren Verständnis der Sequestrierung von frisch hinzugefügten einfachen OM-Komponenten und komplexeren Pflanzenresten wurde die Studie fortgesetzt, um die OM-Sequestrierung im Submikronbereich zu erforschen, da diese die Bodenfunktionen in größerem Maßstab beeinflusst. In dieser Studie wurden die Bodenaggregatfraktionen aus dem Inkubationsexperiment in Studie 2 abgeleitet. Die Bodenaggregate wurden mithilfe der Trockensiebmethode in drei Größenfraktionen unterteilt. Die konventionelle IRMS-Messung zeigte, dass Bodenmikroaggregate (< 53 µm und 53-250 µm) eine höhere Menge an pflanzlichem OM zurückhalten als Makroaggregate (> 250 µm). Kleinere Bodenmikroaggregate (< 53 µm) aus 6 Behandlungen (3 Böden mit einem OM-Gehaltsgradienten × 2 Pflanzenstreu mit unterschiedlichen C/N-Verhältnissen) wurden mittels NanoSIMS und Helium-Ionen-Mikroskopie (HIM) analysiert. Sie wurden auf GaAs-Wafern stabilisiert, um ihre ursprüngliche Struktur möglichst zu erhalten. Die Beziehung zwischen OM und der Verteilung der anorganischen Elemente wurde mit einem NanoSIMS-Gerät unter Verwendung einer Cs^+- bzw. O^--Quelle analysiert.

Die mit HIM gewonnenen Sekundärelektronenbilder (SE) wurden verwendet, um eine 3D-Architektur von Bodenmikroaggregaten mit einer Auflösung von unter einem Mikrometer zu rekonstruieren und den Einfallswinkel der Oberfläche zu analysieren. Dieser Prozess basierte

auf den in der gemeinsam verfassten Studie (Studie 4) entwickelten rechnerischen Ansätzen. Die OM-Verteilung wurde mit der 3D-Rekonstruktion abgeglichen, was eine 4D-Darstellung eines Bodenmikroaggregats ergab. Die Ergebnisse von NanoSIMS und HIM zeigten, dass sich OM bevorzugt an der Oberfläche mit einem Einfallswinkel von 44,60° ± 23,25° ablagert. Der 4D-Bildgebungsansatz ermöglichte die direkte Beobachtung von MAOM auf Oberflächen von Bodenmikroaggregaten mit submikrometrischer Auflösung. Diese Arbeit zeigte, dass die µm-Skalenarchitektur von Bodenmikroaggregaten die Assoziation von OM direkt beeinflusst und somit vermutlich das Schicksal von frischer OM zusammen mit der Persistenz von MAOM bestimmt.

Diese Dissertation liefert ein tieferes Verständnis der OM-Sequestrierung und der C-Dynamik in Böden, das vom Makroboden bis zur submikrometrischen Ebene reichte. Die 4D-Rekonstruktion von Bodenmikroaggregaten klärte die OM-Sequestrierung in der Bodenmikroarchitektur auf und trug zu einem Einblick in die submikrometrische MAOM-Bildung bei.

III. Acknowledgements

I express my gratitude to my supervisors Prof. Dr. Ingrid Kögel-Knabner, Prof. Dr. Carsten Müller, and Dr. Carmen Höschen for their guidance and full support at each stage of this thesis. They introduced me into soil science and allowed me to explore this world.

I acknowledge Dr. Alexander Ost, Dr. Jean-Nicolas Audinot, and Dr. Tom Wirtz in Luxembourg Institute of Science and Technology for their great scientific and analytical support, especially in HIM-SIMS.

I thank Prof. Dr. Florian Wichern for his great knowledge and support in soil microorganisms, Franz Buegger for IRMS measurements, and Dr. Martin Wiesmeier for all support in soil materials. I am also grateful to Dr. Lingling Shi and Prof. Dr. Michaela Dippold for their help in science and life.

I would like to acknowledge all lab technicians at Soil Science at TUM. Especially Gertraud Harrington and Johann Lugmeier offered great help in NanoSIMS labs, Maria Greiner shared her expertise in density fractionation, Sigrid Hiesch taught me PLFAs and amino sugar extractions, and Franziska Fella was able to do anything at any time.

Special thanks to my colleagues and friends Noelia Garcia-Franco, Evelin Pihlap, Franziska Bucka, Christopher Just, Luis Carlos Colocho Hurtarte, Luís Fernando Januário Almeida, Thiago Inagaki for the adventures we had those years.

I want to thank my family and friends for always being there for me.

Financial support from the Deutsche Forschungsgemeinschaft (DFG) through HO 5121/1-1 and the Luxembourg National Research Fund (FNR) through INTER/DFG/17/11779689 are gratefully acknowledged.

IV. Content

I. Summary I

II. Zusammenfassung V

III. Acknowledgements X

IV. Content XI

V. List of publications and contributions XIII

A. Study 1 XIII

B. Study 2 XIV

C. Study 3 XV

D. Study 4 XVI

VI. List of Figures XVII

VII. List of tables XVIII

VIII. List of abbreviations XIX

1. Introduction 1

1.1. Soil structure, SOC content influence C sequestration 1

1.2. Soil C dynamic influenced by living microorganisms 2

1.3. From bulk analysis to microscale investigation 3

1.4. Objectives and approaches 6

2. Methodology 8

2.1. Study sites and soil sampling 8

2.2. Basic soil properties determination 8

2.3. Isotope labeling experiments and microcosm designs (Study 1-4) 10

2.4. C respiration with $^{13}CO_2$ signatures (Study 2) 14

2.5. Fractionation 16

2.6. Microbiological analyses (Study 2) 17

2.7. ^{13}C and ^{15}N incorporation (Study 1, Study 2, Study 3) 20

2.8. Sample preparation for submicron scale analysis (Study 3, 4) 21
2.9. NanoSIMS (Study 3, Study 4) 22
2.10. HIM (-SIMS) and topography analysis (Study 3, Study 4) 22
2.11. Correlate microscopy analysis of soil microaggregates 23
2.12. Statistical analysis (Study 1, Study 2, Study 3) 24
3. Results and discussion 25
3.1. Rapid OM retention influenced by soil fraction size, soil C content, and the N content of added OM (Study 1) 25
3.2. Soil C dynamic influenced by microbial activities (Study 2) 26
3.3. Microstructure of soil particle controlling OM retention (Study 3, Study 4) 28
3.3.1. OM distribution in aggregate sizes 28
3.3.2. OM hot spot and its relation with inorganic elements 28
3.3.3. Bulk analysis vs surface analysis 29
3.3.4. Incidence angle 44.60°: preferential OM retention hot spot 29
4. Conclusions and outlook 30
5. Appendix 32
6. References 33
7. List of publications 41
Study 1 41
Study 2 52
Study 3 68
Study 4 97

V. List of publications and contributions

A. Study 1

Wu, T., Ost, A. D., Audinot, J. N., Wiesmeier, M., Wirtz, T., Buegger, F., Häusler, W., Höschen, C., & Mueller, C. W. (2022). Association of fresh low-molecular-weight organic compounds with clay-sized mineral fraction in soils of different organic carbon loading. Geoderma, 409, 115657.

Contribution:

I carried out incubation experiment, laboratory analyses, data evaluations, and wrote the manuscript.

Objectives:

To investigate how initial carbon (C) retention in the soil mineral-associated organic matter (MAOM) pool is influenced by soil C loading and the nitrogen (N) availability of the low-molecular-weight organic compounds (LMWOC).

Summary:

The initial C loading, which also reflected the soil C saturation level of the soil, was the main factor influencing freshly added OM retention, as a larger amount of newly added LMWOC was retained in the MAOM pool of low C loading soil than in the high C loading soil. The higher N content of added OM enhanced the OM retention in low C but not high C loading soil, pointing to the significance of N in soils. The smaller MAOM fractions, especially clay-sized fractions, retained more freshly added OM than larger MAOM fractions, indicating the importance of the larger specific mineral surface area in OM sequestration.

B. Study 2

Wu, T., Wichern, F., Wiesmeier, M., Buegger, F., Shi, L., Dippold, M. A., Höschen, C., & Mueller, C. W. (2024). Organic carbon loading of soils determines the fate of added fresh plant-derived organic matter. Geoderma, 443, 116816.

Contribution:

I conducted field work, developed the experiment, carried out incubation, laboratory analysis, evaluated data, and wrote the manuscript.

Objectives:

To better understand how freshly added organic matter (OM) retention is influenced by soil carbon (C) loading, thus soil C saturation level; nitrogen (N) content of the added OM; microbial activities.

Summary:

We highlighted that the soil with lower C loading respired a higher amount of C (0.4 mg/g) after amending plant litter. Thus, fresh OM's 'return on investment' is higher in soils with initial higher C loading. The freshly added plant litter led to a higher fungal-to-bacterial (F/B) ratio in the microbial community, which was more pronounced in soils with lower C loading and with lower N content plant litter.

C. Study 3

Wu, T., Ost, A. D., Wichern, F., Buegger, F., Audinot, J. N., Wirtz, T., Höschen, C., & Mueller, C. W. Microtopography of soil aggregates determines the retention of freshly added organic matter. In preparation for submission.

Contribution:

I conducted sample preparation and laboratory analysis, evaluated data, and wrote the manuscript.

Objectives:

To investigate how microtopography of the soil microaggregate regulates the freshly added organic matter (OM) retention. To study if the OM retention in microaggregates is affected by soil OM content and amended OM carbon-to-nitrogen (C/N) ratio.

Summary:

To study the microstructure of the soil microaggregates, a liquid-free sample preparation method was developed to obtain undisturbed samples. A larger amount of freshly added OM was retained in microaggregates than in macroaggregates after 90 days of incubation. We correlated microaggregate topography, based on Helium Ion Microscopy (HIM) analysis, with freshly added OM distribution in the submicron scale, based on NanoSIMS analysis, thus creating a 4D surface reconstruction of microaggregates of each treatment. We demonstrated that the freshly added OM preferentially retained on the surface of a microaggregate with the incidence angle of 44.60° ± 23.25, regardless of soils and treatments.

D. Study 4

* Co-authored study

Ost, A. D., Wu, T., Hoschen, C., Mueller, C. W., Wirtz, T., & Audinot, J. N. (2021). 4D surface reconstructions to study microscale structures and functions in soil biogeochemistry. Environmental Science & Technology, 55(13), 9384-9393.

Contribution:

I carried out sample preparation, participated in NanoSIMS and HIM-SIMS analysis, interpreted the results, and wrote the manuscript that were related to soil.

Objectives:

Developing a workflow and qualitative description of 4D surface reconstruction combining HIM and NanoSIMS images. Promoting a better understanding of the organic matter sequestration hot spots in relation to the topography of soil microaggregates.

Summary:

This study established the workflow of 4D reconstruction of a micro-scale specimen. The method of combining 3D architecture with surface element distribution has been extended to soil biogeochemistry applications. The topography information was expressed using curvature and incidence angle as a more concrete description.

VI. List of Figures

Figure 1 Location of soil sampling sites (1-3) in Puch Germany. *8*

Figure 2 Microcosm design. Figure from Study 2. ..... *13*

Figure 3 Modified Casagrande device. *17*

Figure 4 Graphical view of Study 2 ..... *26*

Figure 5 HIM images and NanoSIMS results of 6 soil particles. The HIM image, O, C, N, Na, Mg, Al, Si, K, Ca, Fe distribution, and RGB image were shown from left to right. In RGB images, red, green, and blue represent O, C, and N, respectively. *32*

Figure 6 4D presentation of soil microaggregates (Study 3). *32*

VII. List of tables

Table 1 Basic soil properties of soils employed in the studies. *9*

Table 2 Overview of soil property determination methods for Study 1-4. ..... *10*

Table 3 Plant residue information, including C, ^{13}C, N, ^{15}N content, and C/N ratio of oat and pea. *12*

Table 4 PLFA markers and assigned groups. *18*

VIII. List of abbreviations

2-/3-/4D	Two-/three-/four-dimensions
at%	Atom-%
AMC	7-amino-4-methyl coumarin
AMC-L	L-leucine-7-amino-4-methyl coumarin
AMC-T	L-tyrosine-7-amido-4-methyl-coumarin
C	Carbon
C/N	Carbon-to-nitrogen ratio
EC	electrical conductivity
F/B	Fungal-to-bacterial
GaAs (wafer)	Gallium arsenide (wafer)
GC-IRMS	Gas chromatography isotope-ratio mass spectrometry
HCl	Hydrochloric acid
HIM	Helium ion microscopy
ICP-OES	Inductively coupled plasma optical emission spectrometry
IRMS	Isotope-ratio mass spectrometry
KOH	Potassium hydroxide
LMWOC	Low-molecular-weight organic compounds
MAOM	mineral-associated organic matter
MES	2-(N-morpholino)ethanesulfonic acid

MUF	4-methylumbelliferone
MUF-P	4-Methylumbelliferyl-phosphate
N	Nitrogen
$NaPWO_4$	Sodium polytungstate
NanoSIMS	Nano scale secondary ion mass spectrometry
OC	Organic carbon
OM	Organic matter
PLFAs	Phospholipid-derived fatty acids
POM	Particulate organic matter
Si	Silicate
SIMS	Secondary ion mass spectrometry
SOC	Soil organic carbon
SOM	Soil organic matter
SSA	Specific surface area
XRD	X-ray powder diffraction

1. Introduction

1.1. Soil structure, SOC content influence C sequestration

Soils are recognized for being one of the largest C pools on the planet (Schlesinger, 2005; Scharlemann et al., 2014). Soil organic carbon (SOC) plays an important role in many ecological functions, especially in soil fertility and the impact of global climate (Post et al., 1982; Scharlemann et al., 2014; Kopittke et al., 2022). During the last decades, several efforts have been made to investigate the mechanisms behind soil SOC storage and how to optimize them in different land uses and soil types.

Based on turnover time, soil OM (SOM) is commonly divided into different physical pools, such as particulate organic matter (POM) and mineral-associated organic matter (MAOM). The latter is known to be more persistent, presenting lower turnover rates (Christensen, 1992; Lützow et al., 2006; Kögel-Knabner et al., 2008). Persistent forms of SOC have been recognized to be less bioavailable through adsorption into the surface of minerals or protection against decomposers in aggregate structures (Torn et al., 1997; Rasmussen et al., 2018) and these processes are primarily controlled at the micro to nanoscale. Soil aggregates formed by the interaction of soil mineral particles and OM < 250 μm (soil microaggregates) are stable for a longer timescale and, therefore, are known to be more critical in storing SOC (Angers et al., 1997; Six et al., 2000; Trivedi et al., 2017).

It has been proposed that soils have an upper limit in which they are physically capable of storing carbon. Many studies have demonstrated that each soil has an upper limit of storing C, which mainly refers to MAOM-C storage capacity (Hassink, 1997; Six et al., 2002; Stewart et al., 2007; Stewart et al., 2008). This SOC storage capacity can be estimated using linear regressions based on soil properties (Wiesmeier et al., 2019). The maximum amount of carbon soil can store is influenced by climate, topography, parent material, organisms, and soil

properties (Feller and Beare, 1997; Six et al., 2002; Liang et al., 2009; Beare et al., 2014; Wiesmeier et al., 2015). While each soil has a typical carbon storage capacity that remains relatively constant, the carbon and nitrogen content within the soil is constantly cycling in and out, maintaining a dynamic equilibrium. This dynamic nature of soil organic matter (SOM) distinguishes overall SOC storage from SOC retention, as retention is a process that involves both stabilization and destabilization of carbon. Recent research highlights that adding nitrogen-rich organic matter to soils unsaturated with organic carbon can enhance carbon retention (Córdova et al., 2018; Wang et al., 2019). However, adding low-molecular-weight organic carbon can destabilize native SOC, with the amount of carbon loss correlated to the nitrogen content of the added substrate (Blagodatskaya et al., 2007; Chen et al., 2014).

Soils with higher SOC saturation levels are overall considered less efficient for further storing C (Castellano et al., 2015; Guillaume et al., 2022). Nonetheless, direct comparisons between soils with different organic matter loadings in their capacity to store further carbon are rare. Thus, to study the C sequestration on the newly added OM, the initial SOC saturation level needs to be taken into consideration.

1.2. Soil C dynamic influenced by living microorganisms

Fungi and bacteria are the main drivers of soil carbon (C) dynamics. Their activities are influenced by their habitats, particularly the C saturation level (Six et al., 2006; Chenu and Cosentino, 2011; Schimel and Schaeffer, 2012). This affects their life strategies, determining C mineralization, ultimately, and soil respiration. When faced with unbalanced nutrient ratios, these microorganisms adjust their consumption of organic matter sources to meet their energy and growth needs. Therefore, soil C dynamics is determined not only by the amount of available C but also by the amount and availability of nitrogen (N). The C/N ratio of plant litter directly impacts soil C dynamics by influencing the microbial community, with C

availability mainly limiting bacterial growth and N limitations affecting fungal growth more strongly (Gentile et al., 2011; Cotrufo et al., 2013; Nguyen et al., 2016). Soils with different C saturation levels and varying N content in plant litter exhibit significant differences in organic matter mineralization (Rousk and Baath, 2007; Wang et al., 2014). However, the exact mechanisms by which soil C saturation and N availability in plant litter influence the fate of soil C remain unclear.

1.3. From bulk analysis to microscale investigation

While the mechanisms of soil carbon storage vary depending on factors like land use and climate, sorption, and protection within soil aggregates are universally important. To understand further how different soil components influence C storage, the influence of microorganisms and other factors on OM persistence has been widely studied in bulk soil and isolated fractions. Small-size fractions, e.g., clay-sized and fine silt-sized fraction (Christensen, 1992), and microaggregates (Six et al., 2002; Lützow et al., 2006) are seen as major C reservoirs in long-term C storage. However, bulk soil analysis is not sensitive to represent microscale conditions. Traditionally, clay mineral surfaces were considered key, but new microscopy techniques now allow more accurate measurements at the micro to nanoscale. Soil microaggregates are a heterogeneous 3D arrangement of minerals and organic components with different chemical composition (Kögel-Knabner et al., 2008). A better understanding of soil aggregate architecture at the sub-micrometer scale is lacking mainly due to the limitations of analytical technologies and computational approaches (Lehmann et al., 2007; Solomon et al., 2012). Synchrotron radiation-based X-ray techniques such as µ-CT were used in soil studies for soil structure analysis and in-site element composition information (Bucka et al., 2019; Pohl et al., 2021) at a high resolution down to a submicron scale (Lehmann et al., 2008; Solomon et al., 2009; Amelung et al., 2024). However, this analytical method is not capable of

isotope mapping (Lehndorff et al., 2021; Pohl et al., 2021), which limits the possibility of revealing OM formation by isotope labelling. For acquiring isotope distribution in soils, IRMS is commonly used analytical method. Although IRMS enable the isotope measurement of different soil fractions, this method is based on bulk sample analysis and therefore, is not capable for a specific soil particle or a region. Thus, to investigate the form and reform of MAOM at a selected area, NanoSIMS measurement was introduced in soil science.

1.3.1. NanoSIMS: 2D element distribution in sub-µm scale

Secondary Ion Mass Spectrometer (SIMS) system is a surface analysis technique for solid samples. The NanoSIMS 50/50 L (Cameca, France) was designed and manufactured in 1990s (Hillion, 1993) for biological and medical research field. The instrument is equipped with an ion beam with the energy ranging from hundreds of eV to tenth of keV. Under 10^{-8}-10^{-10} Torr vacuum conditions, the ion beam is accelerated on the sample surface and induces secondary species ejection. According to the different mass-to-charge (m/z) ratio, the secondary ions ejected from the surface are differentiated in a mass analyzer, which can detect 7 masses simultaneously. With the high sensitivity in the ppm range, SIMS system enables precise isotope ratio measurements. NanoSIMS has been applied to study cosmochemistry, geology, mineralogy, material science, and biology (Hoppe et al., 2004; Labotka et al., 2004; Stern et al., 2005; Hoppe, 2006; Lechene et al., 2006) but the application of NanoSIMS in soil science measuring ^{13}C and ^{15}N labelled samples only started in early 2000 (Cliff et al., 2002; Herrmann et al., 2007a; Herrmann et al., 2007b).

The NanoSIMS 50L instrument used in this thesis is equipped with two exchangeable sources, cesium (Cs^+) and oxygen (O^-). The Cs^+ source is used for measuring negatively charged secondary ions, e.g. ^{12}C, ^{13}C, ^{14}N, and ^{15}N, and therefore enables the visualization of isotope and element distribution of OM. The inorganic element distribution maps, e.g. ^{23}Na, ^{24}Mg, ^{27}Al,

^{28}Si, ^{39}K, ^{40}Ca, and ^{56}Fe, are generated using O^- source. With high mass resolution and down to 50 nm lateral resolution, NanoSIMS became a powerful tool for studying biogeochemical processes in soil science, for instance, OM incorporation and distribution in soils, microbial transformation of OM, interaction of inorganic element and OM, and specific minerals contributed to OM sequestration (Remusat et al., 2012; Vogel et al., 2014; Mueller et al., 2017; Mueller et al., 2023; Amelung et al., 2024).

NanoSIMS measurement is commonly combined with other microscopic technics to obtain further structure and topography information. Scanning electron microscope (SEM) with resolution down to 1 nm was commonly combined with NanoSIMS measurement to obtain high resolution images (e.g. Mueller et al. (2012), Vogel et al. (2014)) and transmission electron microscopy (TEM) with a resolution of 0.5 nm was combined with NanoSIMS for complementary images (Vidal et al., 2016). Micro-scale 3D structure can be analyzed by atomic force microscopy (AFM) (Fleming et al., 2011; Wirtz et al., 2012; Fleming and Wirtz, 2015). However, AFM is not capable measuring topography of soil microaggregates. For the sample with high aspect ratio, as soil microaggregates, the AFM measuring tip will collide with the sample due to the fast scanning speed (Akhtar et al., 2019). Consider the high spatial resolution, Helium Ion Microscopy (HIM) can overcome topography limitations and combined with NanoSIMS for investigating the topography effect of soil microaggregates on OM sequestration.

1.3.2. Helium Ion Microscopy: sub-nm resolution SE images for 3D reconstruction

With a high spatial resolution down to sub-nanometer scale, Helium Ion Microscopy (HIM) is an ideal technique for surface reconstruction (Hlawacek et al., 2014; Wirtz et al., 2015). By applying the photogrammetry method, the 3D surface of the sample can be reconstructed using SE images from different angles (Eulitz and Reiss, 2015; Vollnhals and Wirtz, 2018).

1.3.3. Need for new computational approaches for 4D presentation

Element distribution on the particle surface can be obtained in a 2D image by overlapping images obtained from different techniques. 3D reconstruction of biological samples and inorganic particles has been developed (Vollnhals and Wirtz, 2018). To further elucidate SOM sequestration on the microaggregate surface, we need a 4D presentation of soil aggregate in the submicron scale combining 3D architecture (reconstructed by HIM SE images) and surface element distribution (obtained by NanoSIMS measurement).

1.4. Objectives and approaches

The main goal of this thesis was to deeper understand the overall OM sequestration of freshly added OM in soils differing in SOM legacy, followed by elucidating the submicron scale OM sequestration on the 3D architecture of soil microaggregates. The impact of soil C content, freshly added OM N content, and the microbial activities on C sequestration and C dynamic was investigated. For topography analysis, a rapid sample preparation method that preserves the sample topography was applied.

To address the primary goal, the objectives were as follows:

A. Investigate the rapid newly added OM retention in soil MAOM fractions influenced by particle size, SOC content, and OM N content (Study 1)

   An incubation experiment for 24 h was conducted for rapid retention of newly added OM study. Soils from the same long-term research field but differing in C content were employed to investigate the influence of SOC content on OM retention. How OM N content influences its retention was explored by using two low-molecular-weight organic compounds (LMWOC) highly enriched in ^{13}C and/or ^{15}N. Clay and fine silt-size fractions were analyzed using IRMS to study the freshly added C retention in fine-sized fractions.

B. Investigate the C dynamic in soil influenced by SOC content, plant residue N content, and microorganisms (Study 2)

   Soils with a C gradient and ^{13}C and ^{15}N labeled plant residues that differ in N content were used for a 90-day incubation study. The total C budget was measured to study plant-derived C retention influenced by SOC and plant N content. The C dynamic influenced by microorganisms was investigated by measuring soil respiration with ^{13}C signatures, ^{13}C compound-specific PLFAs, microbial necromass, and enzyme activities.

C. Investigate the OM sequestration influenced by surface chemical composition of soil microaggregates (Study 3)

   Soil aggregates were measured with NanoSIMS using both cesium and oxygen source for studying the correlation of OM and inorganic element distribution.

D. Elucidating how microtopography of soil aggregates fosters OM sequestration (Study 3)

   The microtopography fostered OM sequestration was elucidated by element distribution from NanoSIMS analysis and surface information from 3D reconstruction.

2. Methodology

2.1. Study sites and soil sampling

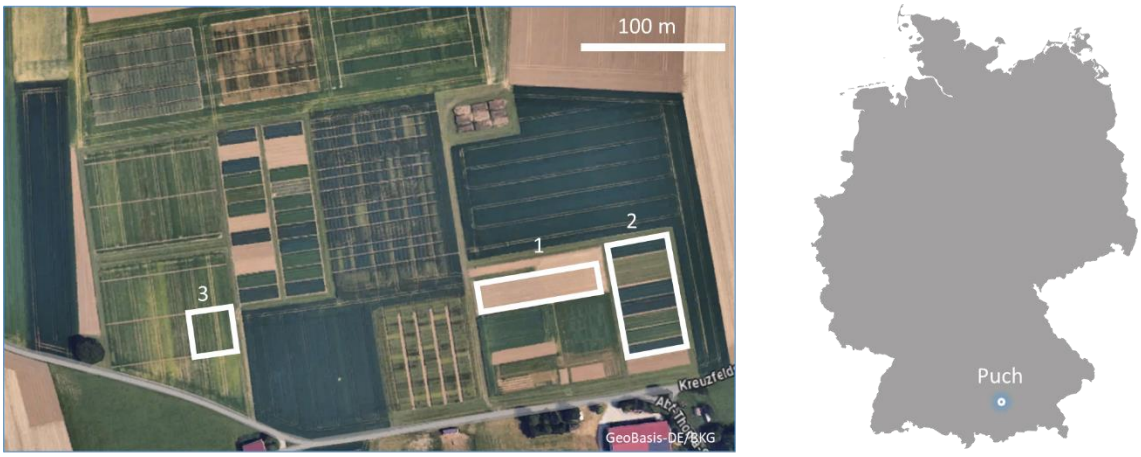

Figure 1 Location of soil sampling sites (1-3) in Puch Germany.

Soils of all studies were sampled from long-term field experimental sites in Puch, Germany (48◦11’37.0”N, 11◦12’57.4”E). The soils were Luvisols derived from loess deposits (IUSS Working Group WRB, 2015). Site 1, 2, and 3 as marked in Figure 1 were under soil management practices bare fallow, three crop rotation, and direct seeding, respectively. We collected the soils from the upper 10 cm at random spots of each sampling site and mixed them thoroughly to form a composite sample. The fresh soil was air-dried at room temperature and subsequently sieved through a 2 mm mesh sieve. After picking out all visible plant residues by hand, the soil was prepared for further experiments and analyses.

2.2. Basic soil properties determination

Basic soil properties and the determination methods were listed in Table 1 and Table 2, respectively.

Table 1 Basic soil properties of soils employed in the studies.

Study	**Soil**	**Soil management**	**Total C content (mg g^{-1})**	**Total N content (mg g^{-1})**	**C/N**	**pH**	**EC**
Study 1, Study 4	Low-C soil	Bare fallow	6.1 ± 0.0	0.7 ± 0.0	8.7 ± 0.0	6.4	54.2
Study 1, Study 4	High-C soil	Direct seeding	17.4 ± 0.3	1.8 ± 0.0	9.9 ± 0.0	7.6	67.2
Study 2, Study 3	Low-C soil	Bare fallow	6.4 ± 0.1	0.8 ± 0.0	8.4 ± 0.1	6.4	54.2
Study 2, Study 3	Medium-C soil	Three crop rotation	12.5 ± 0.0	1.4 ± 0.0	9.0 ± 0.2	6.9	60.8
Study 2, Study 3	High-C soil	Direct seeding	20.7 ± 0.0	2.1 ± 0.0	9.9 ± 0.2	7.6	67.2

Table 2 Overview of soil property determination methods for Study 1-4.

Soil properties	Methods	Study
Soil mineralogy	XRD (Philips PW 1820 diffractometer, Co Kα radiation λ = 1.7902 Å, 2θ rang 2° to 26° in step of 0.02°, counting time 5 s for each step)	1
pH and EC	Soil:deionised water ratio of 1:5 (w/v) water suspension	1
Fe content	ICP-OES (Vista Pro CCD Simultaneous, Varian, Darmstadt, Germany)	1
Texture	H2O2 oxidation to remove OC. Wet sieving followed by X-ray sedimentation measurement (Sedigraph Plus, Micromeritics, Aachen, Germany)	1
SSA	N2-BET (AUTORSORP-1, Quantachrome, Odelzhausen, Germany)	1
C and N content	Dry combustion (Elemental Analyzer, EuroEA, HekaTech, Wegberg, Germany)	1

2.3. Isotope labeling experiments and microcosm designs (Study 1-4)

2.3.1. Soils incubated with low-molecular-weight organic compound (Study 1, Study 4)

To study the fast retention of freshly added substrates in MAOM, a 24-hour incubation was conducted using two soils and two low-molecular-weight (LMW) substrates. To achieve our research goals 1) how soil C loading influences C retention as MAOM, we used soils from bare fallow (sampling site 1 in Figure 1) and direct seeding management (sampling site 3 in Figure 1) due to the larger difference in their SOC content, and 2) how the N availability of the

amendments influence C retention as MAOM glucose (D-Glucose-$^{13}C_6$, Sigma-Aldrich, ≥ 99 atom% ^{13}C) and amino acid (algal amino acid mixture, Sigma-Aldrich, ≥ 98 atom-% ^{13}C and ≥ 98 atom-% ^{15}N) as amendments for their different N content.

Two soils and 3 amendments (glucose, amino acid, and control), with 3 replicates each, totalized 18 microcosms. Five grams (dry weight) of sieved fresh soil was weighed in a 100 mL centrifuge tube (Ultra-Hight Performance, VWR). The LMW amendment was added as a solution to soils at a C input rate of 0.82 mg g^{-1} soil, which was based on the 3.2 t ha^{-1} yr^{-1} mean C input at experimental site Puch. Glucose and amino acid powder were weighed into beakers and subsequently dissolved with 25 mL of deionized water. The solutions were prepared at the concentration of 2.183 mg glucose mL^{-1} and 2.169 mg amino acid mL^{-1}. Each microcosm of LMWOM treatment received 25.2 µl solution, thus 0.273 mg ^{13}C, for each gram of soil. For amino acid treatment, each microcosm also contained 0.18 mg ^{15}N g^{-1} soil. All microcosms, including controls, were adjusted the moisture to 50% water holding capacity with deionized water. To homogenize the soil with a solution in each microcosm, a glass rod was used to stir the sample. Each microcosm was sealed with a lid and left to rest at 20°C in a dark room for 24h. All microcosms were frozen with liquid nitrogen after 24 hours to stop all biological activities. The frozen samples were subsequently freeze-dried.

2.3.2. Soils incubated with plant litters (Study 2, Study 3)

To better understand the C retention of the amendment in soils, we moved further from LMWOM to plant litter as OC input. In this incubation experiment, we used three soils from bare fallow (sampling site 1), three crop rotations (sampling site 2), and direct seeding (sampling site 3) management. These three soils have a carbon gradient from 6.4 to 20.7 mg g^{-1} soil for studying how soils with different C loading, thus different SOC saturation level retain

freshly added OM. ^{13}C and ^{15}N labeled pea and oat plant litter (details in Table 3) were used as an amendment to investigate the influence of N content of added OM on C retention.

Plant powder	**C content (mg g^{-1})**	**^{13}C atom%**	**N content (mg g^{-1})**	**^{15}N atom%**	**C/N**
Oat (*Avena sativa* L.)	440	2.18	15.9	4.0	27.8
Pea (*Pisum sativum* L.)	432	1.69	40.2	2.0	10.7

Table 3 Plant residue information, including C, ^{13}C, N, ^{15}N content, and C/N ratio of oat and pea.

We used a gas-tight Mason Glass jar (473 ml, KoRo) as a microcosm (Figure 2). On the lid of each jar, we installed one stainless steel tube (Swagelok) with a septum (Standard Septa, Wagner& munz) for gas sampling during the incubation. The sample was placed in a polyvinyl chloride (PVC) cylinder (50 mm in height, 45.2 mm inner diameter) with a mono-layer polyester mesh (mesh size 55 μm) fixed at the bottom with an O-ring (nitrile rubber). The cylinder was placed on the metal grid in the glass jar for better gas circulation at the bottom.

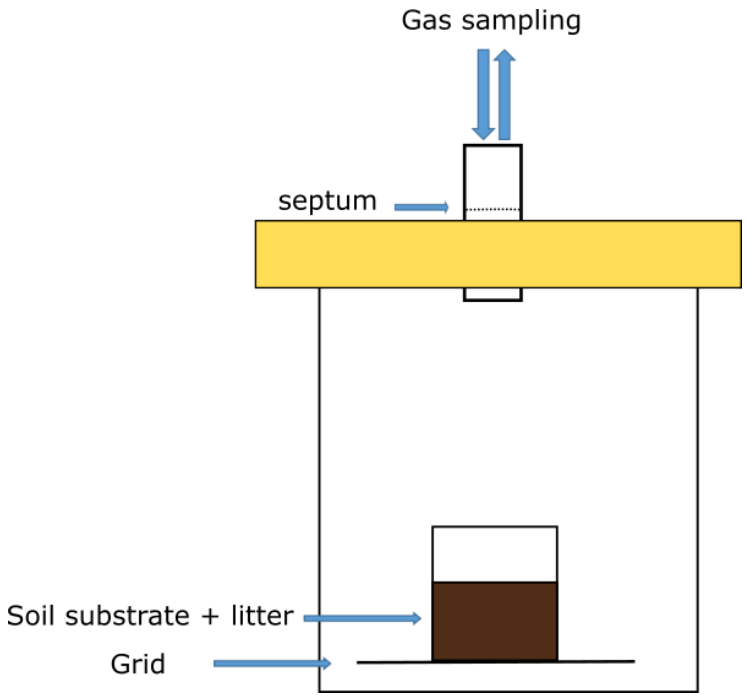

Figure 2 Microcosm design. Figure from Study 2.

We performed a 3 × 3 design, 3 soils and 3 amendments (control, oat, and pea) with 5 replicates for each treatment. The amendment was mixed with 50 g (dry weight) of soil at the rate of 0 mg g^{-1} (control) and 10 mg g^{-1} (equivalent to 13 Mg ha^{-1}) in the cylinder. The starting point of the experiment was considered once the fine droplet of water was added into the cylinder and adjusted to 50% water holding capacity. The start time interval for each sample was set at 1 min, considering the gas sampling during the incubation.

The incubation was conducted in a dark thermostatic room of 22°C. The glass jars were partly opened during the 90 days of incubation to avoid an anaerobic environment. The moisture was controlled every 48 hours. After 90 days, each sample in the cylinder was mixed thoroughly to obtain a homogeneous sample. Approximately 15 grams of each sample was sampled and stored at 4 °C for enzyme and PLFA analyses. The rest of the sample was frozen using liquid nitrogen to stop all microbial activities and freeze-dried to obtain dry material for further analyses.

2.4. C respiration with $^{13}CO_2$ signatures (Study 2)

Soil respiration in the incubation experiment with plant litter addition was monitored together with ^{13}C signatures. The gas was sampled at 24 h, 72 h, 7 days, 14 days, 30 days, 60 days, and 90 days of incubation. A 25 ml gas-tight syringe (Model 1025 TLL, Hamilton) and 12 ml evacuated vials (Exetainer 12 ml, flat bottom, Labco, UK) were used for gas sampling. Each sampling collected 12.5 ml gas from the headspace of the microcosm and injected it into the vial. The syringe was rinsed 3 times using Ar between each gas sampling to avoid contamination.

The microcosms were sealed to start sampling, followed by injecting inert gas (Ar) to avoid negative pressure due to the sampling. The first gas sampling took place directly after injecting the Ar, and the time was noted as t_0. The next 3 sampling points of each microcosm were performed at time t_0 + t, t_0 + 2 t, and t_0 + 3 t, totaling 4 sampling points per microcosm. Between the sampling points, the jar was sealed for a certain time, t, which ranged between 40 and 180 min, depending on the incubation day and the treatment.

The CO_2 concentration and ^{13}C abundance of each sample were determined using GC-IRMS (Delta plus, Thermo Fisher, Dreieich, Germany). The ^{13}C enrichment of the samples was given in atom-%. The respired CO_2 of each microcosm was calculated using a linear regression model based on the CO_2 concentration difference between the 4 sampling points (Equation 1).

$$CO_2(ppm) = k\left(\frac{ppm}{min}\right) * t(min) + A(ppm)$$

Equation 1

The slope k represents the soil respiration rate. A stands for the calculated environmental CO_2 concentration from the liner regression.

With the known cylinder size, the available volume ($VHeadspace$) can be calculated. Therefore, the respiration rate of CO_2 for each microcosm was calculated using Equation 2.

$$Respiration\ CO_2(mg * min^{-1}) = k\left(\frac{ppm}{min}\right) * VHeadspace(mL) * \frac{M_{CO_2}\left(\frac{mg}{mmol}\right)}{M_V\left(\frac{mL}{mmol}\right)} * \left(\frac{10^{-6}}{ppm}\right)$$

Equation 2

The M_{CO_2} and M_V stand for the molar weight of CO_2 and the gas molar volume at 22°C, respectively.

The CO_2-C respiration rate ($Respiration\ CO_2\text{-}C$) and the CO_2-C respiration rate per gram of soil ($R_{CO_2\text{-}C}$) were calculated using Equation 3 and Equation 4, respectively.

$$Respiration\ CO_2\text{-}C\ (mg * min^{-1}) = Respiration\ CO_2\ (mg\ * min^{-1}) * \frac{M_C\left(\frac{mg}{mmol}\right)}{M_{CO_2}\left(\frac{mg}{mmol}\right)}$$

Equation 3

where M_C represents the molar weight of C.

$$R_{CO_2\text{-}C}\ (mg * min^{-1}\ * g^{-1}Soil) = \frac{Respiration\ CO_2\text{-}C\ (mg * min^{-1})}{soil\ mass\ (g)}$$

Equation 4

Soil mass is the soil dry weight per microcosm.

The CO_2-C respiration rate was further normalized to each gram of SOC per gram of soil (Equation 5).

$$Normalized\ R_{CO_2\text{-}C}\ (mg * min^{-1} * g^{-1}SOC\ )$$

$$= \frac{Respiration\ CO_2\text{-}C\ (mg * min^{-1}\ * g^{-1}Soil)}{SOC(mg * g^{-1}Soil)} * \left(\frac{10^3 mg}{g}\right)$$

Equation 5

The cumulative CO_2-C respiration during 90 days of incubation was calculated using integration (OriginPro 2021).

2.5. Fractionation

2.5.1. Density fractionation (Study 1)

To separate MAOM and POM, density fractionation was used in Study 1. Soil sample in Study 3 was also prepared using this method:

a. Weigh approximately 3 g of freeze-dried soil sample;
b. Submerge soil sample in 50 mL $NaPWO_4$ with a density of 1.8 g cm^{-1};
c. Disperse sample using ultrasonic with an energy input of 480 J mL^{-1};
d. Centrifuge the sample at 3500 rpm for 30 min at 20 °C;
e. Separate the floating fraction (POM) from heavy fraction (MAOM);
f. Wash POM and MAOM fractions with deionized water using pressure filtration system (filter pore size 0.45 µm) until the EC below 50 µS cm^{-1};
g. Separate MAOM fraction by sedimentation in deionized water;
h. Freeze-dry all fractions.

2.5.2. Dry aggregate fractionation (Study 3, Study 4)

Dry aggregate fractionation is a time-efficient way of separating aggregates of different sizes. This method is performed by mechanical force and, therefore, keeps the sample undisturbed by liquid. A modified Casagrande device (Mennerich Geotechnik, Hannover, Germany) equipped with a stack of sieves (53 µm and 250 µm) was employed in this method:

a. Weigh 10 g of freeze-dried soil;

b. Transfer the sample to the top sieve of the sieve stack;

c. Set tap frequency of 2 Hz for 1000 cycle

Figure 3 Modified Casagrande device.

2.6. Microbiological analyses (Study 2)

2.6.1. PLFA analysis

The microbial community composition was calculated by measuring PLFA, using the method adapted from Frostegård et al. (1991). We introduced an internal standard (19:0 phospholipid) to each sample followed by adding a mixture of chloroform, methanol, and citric buffer (0.15 M, pH 4.0) (1:2:0.8 v/v/v) to extract the lipids. In sequence, the solution was subsequently transferred to a silica column to remove the neutral-, glycol-, and phospholipids with chloroform, acetone, and methanol. The lipids were then hydrolyzed, methylated, and finally extracted with hexane. The samples were dried under N2 steam and then re-dissolved in toluene with 13:0 fatty acid methyl ester (1 µg μl^{-1}) as the second internal standard. The samples were measured using GC-FID. Based on the external calibration curve, followed by

internal standard corrections (Gunina et al., 2014), we calculated the quantity of each PLFA. The $^{13}C/^{12}C$ of PLFAs was determined using GC-IRMS, then corrected according to Glaser and Amelung (2002). Thus, we calculated plant litter C-incorporation in PLFAs using Equation 6.

$$plant\ litter - C\ incorporation(\%) = \frac{^{13}C\ abundance\ in\ PLFAs}{^{13}C\ input\ in\ the\ soil}$$

Equation 6

We assigned PLFA markers to different groups of microorganisms (see Table 4) according to Sommer et al. (2017) and Lewandowski et al. (2015).

Table 4 PLFA markers and assigned groups.

Microbial group	PLFA markers
Gram-negative (G-) bacteria	16:1ω7c, cy17:0, 18:1ω7c, cy19:0
Gram-positive (G+) bacteria	i15:0, a15:0, i16:0, i17:0
Actinobacteria (Ac)	10Me16:0, 10Me17:0, 10Me18:0
Fungi	18:2ω6,9
Non-specified	a14:0, 14:1w5c, 14:0, 15:0, 16:0, 17:0, 18:3w3,6,9, 18:0, 20:0

2.6.2. Enzymes activities

We analyzed 6 enzyme activities: β-glucosidase (BG), β-xylosidase (BX), β-cellobiohydrolase (BC), chitinase, leucine-aminopeptidase, and acid phosphatase, based on fluorimetric microplate assays (Marx et al., 2001; Marx et al., 2005). The activity of BG, BX, BC, chitinase, leucine-aminopeptidase, and acid phosphatase was measured using 4-methylumbelliferone-b-D-glucoside, 4-methylumbelliferone-7-b-D-xyloside, 4-methylumbelliferone-b-D-cellobioside, AMC-T and AMC-L, and MUF-P, respectively.

Approximately 1 g of soil (dry weight) were suspended in 50 ml of sterile water and dispersed with an ultrasonic disaggregator for 2 min using low-energy sonication (50 J s^{-1}). Aliquots of 50 µl suspension and 50 µl buffer were pipetted to 96-well microplates (black pure Grade® microplates, Brand GmbH, Wertheim, Germany). Afterward, 100 µL of the corresponding substrates at concentrations of 20, 40, 60, 80, 100, 200, and 400 mmol substrate g^{-1} soil were added to the microplates. Subsequently, the fluorescence of the microplates was measured at 0-, 60-, and 120-min with an automated fluorometric plate-reader (excitation wavelength 355 nm, emission 450 nm, Victor3 1420 050 Multi-label Counter; PerkinElmer, Waltham, MA, USA). We used the standard curve to calculate the enzyme activities (German et al., 2011), and used the Michaelis-Menten kinetic equation (Equation 7) to estimate the maximum enzyme activity (Vmax), parameter K_m, and substrate concentration (S) at $V_{max}/2$ reaction rate (Marx et al., 2001).

$$V = (V_{max} * S)/(K_m + S)$$

Equation 7

2.6.3. Microbial necromass

The fungal and bacterial necromass were estimated by measuring 4 soil amino sugars: glucosamine (GlcN), mannosamine, galactosamine, and muramic acid (MurA). We adapted the extraction procedure as described by Liang et al. (2012).

We hydrolyzed 400 mg of the post-incubated sample with 10 ml of 6 M HCl at 105 °C for 8 h. Internal standard was added to the hydrolysate after cooling down the room temperature. Subsequently, the solution was filtered and dried using a rotary evaporator (Heidolph) at 40 °C. The sample was re-suspended with deionized water, followed by adjusting pH to 6.6-6.8 using 1 M KOH to precipitate salt. Each sample was derived using 32 mg ml^{-1} hydroxylamine

hydrochloride and 40 mg ml^{-1} 4-dimethylamino-pyridine in pyridine-methanol (4:1 v/v). The DCM and HCL were used to wash the samples and the upper phase was discarded. The samples were washed with H2O and then dried under an N_2 stream. Prior to the GC-FID measurement, dried extracts were dissolved in 300 µl ethyl acetate/n-hexane (1:1 v/v). The quantity of amino sugars was estimated using calibration curves based on different concentrations of external standards. According to Appuhn and Joergensen (2006), we calculated bacterial and fungal necromass C based on muramic acid and glucosamine content (Equation 8 and Equation 9).

$$Bacterial\ necromass\ C\ (mg\ g^{-1}\ soil) = MurA\ (mg\ g^{-1}\ soil) * 45$$

Equation 8

$$Fungal\ necromass\ C\ (mg\ g^{-1}\ soil) = (mol\ GlcN - 2 * mol\ MuraA) * molar\ weight\ GlcN * 9$$

Equation 9

2.7. ^{13}C and ^{15}N incorporation (Study 1, Study 2, Study 3)

Stable isotope enrichment of samples was measured using an IRMS. The enrichment of ^{13}C and ^{15}N were given in at%. The fraction amendment-derived isotope (f_x) was calculated using the enrichment of the sample (At_{sample}), the control ($At_{control}$), and the amendment ($At_{amendment}$):

$$f_x = \frac{At_{sample}(at\%) - At_{control}(at\%)}{At_{amendment}(at\%) - At_{control}(at\%)}$$

Equation 10

where *x* stands for the isotope ^{13}C or ^{15}N.

The content of amendment-derived C ($C_{amendmentderived}$) and N ($N_{amendmentderived}$) in each fraction was calculated using Equation 11 and Equation 12.

$$C_{amendmentderived}(mg * g^{-1}) = f_C * C(mg * g^{-1})$$

Equation 11

$$N_{amendmentderived}(mg * g^{-1}) = f_N * N(mg * g^{-1})$$

Equation 12

The incorporation ($Incorporation$) of amendment C and N in each fraction were calculated from amendment derived C and N, and the amount of input C and N ($C \vee N_{input}$):

$$Incorporation(\%) = \frac{C \vee N_{amendmentderived}(mg * g^{-1})}{C \vee N_{input}(mg * g^{-1})}$$

The proportion of amendment-derived C or N ($f\%$) in each fraction was calculated as follow:

$$f\% = 100\frac{\% * Incorporation}{\sum\ Incorporation}$$

For C incorporation in each PLFA, we used Equation 10, and Equation 13.

$$Incorporation_{PLFA}(\%) = \frac{f_C * C\% \in PLFA * PLFAcontent(mg * g^{-1})}{C_{input}(mg * g^{-1})}$$

Equation 13

The proportion of C in each PLFA ($C\% \in PLFA$) is based on the chemical formula of each compound.

2.8. Sample preparation for submicron scale analysis (Study 3, 4)

We prepared soil microaggregates in a liquid-free method for NanoSIMS and HIM (-SIMS) analysis. A square-shaped wafer with the size of 7 * 7 mm was used for each sample. Si wafer was used in Study 4, while in Study 3, we used GaAs wafer. We placed a few µg of soil fraction in the middle of the wafer, stabilized it by storing it at -18°C for 20 min, and then moved it to

room temperature. The loose particles were blown away with a compressed air gun. A gold coating of approximately 15 nm was applied to samples before each measurement.

2.9. NanoSIMS (Study 3, Study 4)

We used nanoscale secondary ion mass spectrometry (NanoSIMS) (NanoSIMS 50L, Cameca, France) to acquire the element distribution at submicron scale of soil microaggregates. The Cesium source (Cs+) (16 keV, 2 pA) was used to detect the secondary ion distribution of mass 16 (^{16}O), 24 ($^{12}C^{12}C$), 25 ($^{12}C^{13}C$), 26 ($^{12}C^{14}N$), 27($^{12}C^{15}N$), 43 ($^{27}Al^{16}O$) and 72 ($^{56}Fe^{16}O$) at 256 × 256 pixels, 1 ms/pixel, 40-60 planes and a raster size of 20-25 µm. When the $^{12}C^{13}C/^{12}C^{12}C$ or $^{12}C^{15}N/^{12}C^{14}N$ ratio of measured spot larger than 0.05, it is considered C enriched or N enriched spot, respectively. And therefore, this spot is a newly formed OM spot. The RF plasma oxygen source (O^-) was used to measure the distribution of 23 (Na), 24 (Mg), 27 (Al), 28 (Si), 39 (K), 40 (Ca), and 56 (Fe) at 256 × 256 pixels, 1 ms/pixel, 30-90 planes and a raster size of 10-30 µm.

We applied electron multiplier dead-time correction using OpenMIMS plugin in ImageJ (Gormanns et al., 2012). The sum of images was based on auto-alignment of over 60 measurement planes. The images of each measurement were combined into a tiff file and the RGB image using the distribution of ^{16}O in red, $^{13}C^{12}C/^{12}C^{12}C$ in green, and $^{15}N^{12}C/^{14}N^{12}C$ in blue, with the threshold at 0.05 of the ratio. We carried out machine-learning algorithm segmentation to all RGB images in Ilastik 1.3.3 according to Sommer et al. (2011). The OM-enriched hot spots and the enrichment of each patch were analyzed based on the segmentation masks created with the software Ilastik.

2.10. HIM (-SIMS) and topography analysis (Study 3, Study 4)

In Study 3, Helium Ion Microscopy (HIM) was used to acquire the secondary electron (SE) images of the microaggregates with a spatial resolution of down to 0.5 nm. For 2D analysis, one image per sample was taken at the sample stage perpendicular to the primary beam. At

a stage tilt of 45°, 24 SE images were acquired with a stage rotation step of 15°. Another 15 pictures were taken at a stage tilt of 54°.

In Study 4, HIM with Secondary Ion Mass Spectrometry (SIMS) system was used to acquire SE images and in-situ chemical imaging of ^{23}Na, ^{24}Mg, and ^{39}K on the microaggregates surface.

2.11. Correlate microscopy analysis of soil microaggregates

2.11.1. 2D image correlation

For 2D image correlation, 1 SE image of each microaggregate was required. We performed Laplace fusion in ImageJ, adapted from Vollnhals et al. (2017), to correlate NanoSIMS measurements with HIM images. In brief, we first used the RGB image from the NanoSIMS measurement to correct the SE image using non-linear transformations. A Gaussian blur filter was applied to the corrected SE image of 2048 × 2048 pixels. Next, the image was downscaled to 1024 × 1024 pixels (Image 2), then 512 × 512 pixels (Image 3). At 512 × 512 pixels' resolution, the SIMS image with OM enrichment distribution was added to Image 3. This image was then upscaled to 1024 × 1024 pixels followed by adding Image 2. We followed the same procedure and obtained the image in 2048 × 2048 pixels as the final image.

2.11.2. 3D architecture reconstruction and curvature analysis

3D architecture reconstruction of the soil microaggregates was carried out using Autodesk ReCap Photo. The curvature of microaggregates' surface was determined using MATLAB. Detailed calculation was described by Ost et al. (2021). For each 3D date point k, the curvature (σ_k) was calculated based on its 230 neighbor points using (Wilke, 2002):

$$\sigma_k = \frac{1}{N}\sum_{i=1}^{N}\theta_{k,i}$$

Where $\theta_{k,i}$ stands for the angle between the normal vector of point k and the neighbor. N represents the total amount of neighbor points.

2.11.3. 4D surface analysis

To demonstrate 4D surface information of microaggregates, MeshLab was used to overlay SIMS images on the 3D architecture. We obtained the topography information of enriched OM hot spots and thus, the 3D distribution of OM on the microaggregates.

2.12. Statistical analysis (Study 1, Study 2, Study 3)

All statistical analyses were performed in OriginLab (Origin 2019, Origin 2020 and Origin 2021). The normally test was first carried out on the measured data using Shapiro-Wilk test. The data with normal distribution was tested by ANOVA with Tukey's HSD test as the post hoc test. For the non-normal distributed data, transformations were applied to the raw data followed by the normality test. When the transformed data failed normality test, the Kruskal-Wallis ANOVA was applied to the raw data with Dunn's test as the post hoc test.

3. Results and discussion

3.1. Rapid OM retention influenced by soil fraction size, soil C content, and the N content of added OM (Study 1)

After incubating two OM amendments with different N contents (glucose and amino sugar mixture) and two soils differed in C content (0.6% vs 1.7%), the OM retention on clay- and fine-silt-sized fractions was determined. The IRMS results demonstrated that the recovered OM on clay-sized fractions was 5-10-fold higher than on fine silt-sized fractions in all treatments. Our founding emphasized the importance of fine mineral fractions, especially clay-sized fractions in sequestering OM input in soils (Christensen and Sørensen, 1985; Kaiser and Zech, 2000). By measuring the specific surface area (SSA), we demonstrated that the amount of associated OM on each fraction is positively related to its SSA, which supported the previous findings (Mayer, 1994; Saggar et al., 1996; Sarkar et al., 2018). Clay-sized fractions with greater SSA enabled a larger amount of OM to be retained than fine silt-sized fractions.

As soils are suggested to have a SOC storage limit (Hassink, 1997; Six et al., 2002), we estimated the two soils' saturation level based on their texture according to Feng et al. (2013). Compared to the average C saturation level of Bavarian cropland soils of 50% (Wiesmeier et al., 2019), one soil was depleted in SOC with 33% SOC saturation level, whereas another one had a 75% SOC saturation level. We demonstrated that SOC-depleted soil had greater efficiency retaining added OM compared to high SOC saturation level soil, which is supported by Stewart et al. (2007), who pointed out that soil further than its SOC storage capacity is more efficient in sequestering new OC.

By adding OM with and without N content, we demonstrated that the N content of added OM clearly enhanced the freshly added OM retention in the C-depleted soil but was not obvious in soil with high C content. Double amount of amino acid-derived C than glucose-derived C

was retained in the soil low in C. However, in the high C content soil, only 2% more of amino acid-derived C than glucose-derived C was recovered in fine fractions. The higher N content enhanced SOC content is in agreement with other studies, for instance, Lu et al. (2011) showed in a meta-analysis that N fertilization increased SOC pool at 3.5% for agricultural soils. A positive relationship between the N content of added OM and SOC accumulation was observed in both simple amendments, e.g., glucose with or without N addition (Wang et al., 2019), and more complex OM amendment, e.g., plant litter N content (Córdova et al., 2018). However, higher N content did not increase the added OM retention in the soil MOAM pool. This indicated that further SOC sequestration is controlled by SOC saturation level over N content, which is supported by a model study on agricultural and forest soils (Castellano et al., 2015).

3.2. Soil C dynamic influenced by microbial activities (Study 2)

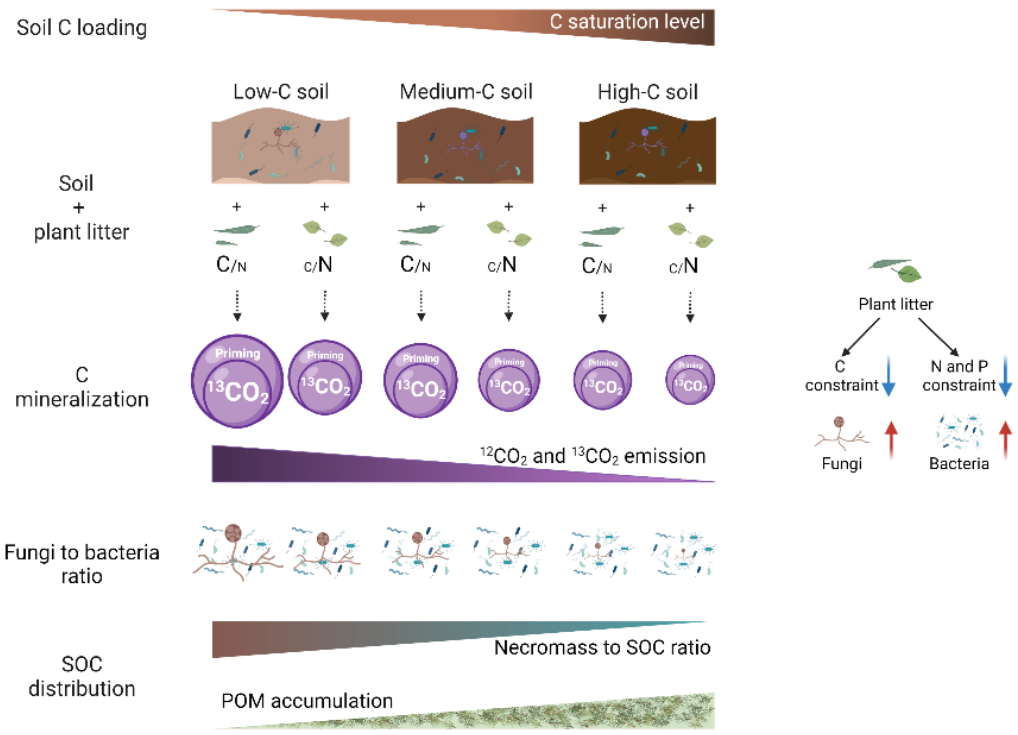

Figure 4 Graphical view of Study 2

Two ^{13}C and ^{15}N enriched plant litters were used as more complex OM amendments for further investigating the C dynamic in soils influenced by microorganisms. Pea and oat litters were chosen due to their different N content (pea > oat). We used 3 agricultural soils that differed in SOC content (ranging from 6.4 - 20.7 mg g^{-1}) due to soil management effects (details are listed in Table 1). All studied soils showed a gain in their C stock in response to plant litter addition. Concerning native SOC content, soil with lower C loading gained a higher proportion of C. Therefore, the relative C sequestration potential was demonstrated to be greater in soils with lower C saturation levels (Stewart et al. (2007), Study 1).

We demonstrated that both plant litter amendments in all three soils induced a positive CO_2 release. This is in line with other studies that demonstrated increasing OM input resulted in higher cumulative CO_2 respiration (Don et al., 2013; Rui et al., 2016; Mendoza et al., 2022). We highlighted our result that with OM amendment, soil with lower C content mineralized a higher proportion of plant litter-derived C and native OM-derived C. The negative correlation between soil C content and cumulative soil respiration indicates a more vulnerable SOM in soil depleted in C. Increase in the proportion of added C to native SOC led to a lower C retention efficiency, which was demonstrated in our study by lower C content soil respired higher amount of CO_2. Nevertheless, plant litter addition led to a positive feedback of soil C content in all soils. Thus, continuous C addition can increase SOC storage, which further enhances the efficiency of freshly added C retention (Stewart et al., 2008; Mendoza et al., 2022; Wu et al., 2022).

Soil respiration is linked with the activities of microorganisms. The increase of respired CO_2 can be attributed to the response of microbial activity to added OM. We demonstrated an increase in the fungi-to-bacteria (F/B) ratio with OM addition by measuring PLFAs. The F/B ratio was negatively related to plant litter N and SOM N content, indicating N benefited

bacterial over fungal growth. With a ^{13}C tracer, we found a larger amount of pea-derived C than oat-derived C recovered in bacteria biomarkers. With the evidence from enzyme analysis that showed C limitation in higher C-content soil and nutrient (N and P) limitation in lower OM-content soil, we can conclude that nutrient availability limits fungal growth and C limits bacterial growth, in line with other studies (Rousk and Baath, 2007; Wang et al., 2014).

3.3. Microstructure of soil particle controlling OM retention (Study 3, Study 4)

3.3.1. OM distribution in aggregate sizes

With a dry aggregate fractionation method modified from Felde et al. (2021), we fractionated post-incubation bulk soils derived from Study 2 into three sizes: macroaggregates (> 250 µm), larger microaggregates (53-250 µm), and smaller microaggregates (< 53 µm). Microaggregates were more critical than macroaggregates in OM storage as more than 70% of plant litter-derived C was found in the microaggregates, which accounted for 39%-49% of soil dry weight.

3.3.2. OM hot spot and its relation with inorganic elements

By 2D elements mapping using NanoSIMS, we obtained the newly added OM hot spot and Na, Mg, Al, Si, K, Ca, and Fe distribution. For each studied soil microaggregate in Study 3, the Cs^+ source for OM distribution and O^- source for inorganic element distribution were applied on the same spot. Previous studies using NanoSIMS pointed out the Fe, Al, Ca, or Mn distribution was correlated to OM storage (Rennert et al., 2014; Rowley et al., 2018; Pohl et al., 2021; Rowley et al., 2023) and the newly formed OM is closely related to Fe, Al, and Ca (Keiluweit et al., 2012; Inagaki et al., 2020; Shabtai et al., 2023). We could not demonstrate any inorganic element directly dominates the sequestration of newly added OM (element mapping is shown in Figure 5). This could probably because our measurement demonstrated element distribution of undisturbed sample surface, whereas the other studies showed the

measurements on samples either prepared using liquid or embedded in resin then cut and polished.

3.3.3. Bulk analysis vs surface analysis

The ^{13}C and ^{15}N enrichment of bulk analysis on microaggregates < 53 µm demonstrated significant differences between soils. However, the differences between these enrichments in microscale analysis cannot be found. This points to the fact that bulk and surface OM sequestration are disconnected. To elucidate how topography influences OM sequestration, we should apply the techniques directly given the in-site information.

3.3.4. Incidence angle 44.60°: preferential OM retention hot spot

The 3D architecture of soil particles was reconstructed using their HIM SE images, as described in Study 4. We introduced the incidence angle to describe the soil sample surface for analyzing the effect of topography in concrete numbers. We correlate OM distribution of soil microaggregates surface with their 3D architecture (Figure 6). The curvature of enriched spots among all microaggregates did not show a significant difference between all three studied soils or with oat or pea litter amendments. We highlighted that the newly added OM is preferentially retained on the soil surface with an incidence angle of around 44.60°, regardless of SOC legacy and OM N content.

Vogel et al. (2014) showed previously that rough surfaces in organo-mineral clusters provide essential reactive interfaces for OM sequestration. Here, we are able to reconstruct the OM distribution on the surface of primary particles and further expressed the surface roughness using incidence angle with concrete numbers. The 3D architecture + surface analysis overcome the limitation of 2D measurement, which precluded precise evaluations of soil microtopography. This advanced the understanding and added more concrete knowledge of OM sequestration in submicron scale.

4. Conclusions and outlook

This thesis focused on the general understanding of the fate of OM, especially on the MAOM formation driven by the 3D architecture of soil particles at the submicron scale. With bulk analysis, the influence of initial SOC content, OM C/N ratio, microorganisms, and soil particle size was studied. Microscale element distribution and topography's effect on OM sequestration were investigated at a resolution down to sub-µm.

In rapid OM retention and a 3-month plant litter retention experiment, we both demonstrated that smaller particle sizes retained a higher amount of added OM. For the MAOM pool of different sizes, clay-sized fractions recovered 5-10 fold freshly added OM compared to fine silt-sized fractions due to the higher SSA in smaller-sized fractions. In aggregates of different sizes, microaggregates demonstrated to be a more critical OM pool than macroaggregates by harboring over 70% of added OM but with less than half of the soil dry weight.

The initial SOC content reflects the soil C saturation level in our studies. Soil with lower C content demonstrated higher C sequestration potential in relation to the initial C loading when adding fresh OM. The OM amendment with higher N content enhanced C retention, especially in C-depleted soil.

The bulk analysis showed the C sequestration potential and C dynamic influenced by microbial activities. Microbial community composition was shifted towards higher F/B ratios with plant litter addition. This shift was more pronounced in soils with lower OM content and plant litter with a higher C/N ratio, indicating that higher C availability benefits fungi over bacteria growth. Moreover, OM amendments accelerated the C mineralization for both native SOM and added OM. The higher N-content plant litter induced less C mineralization, therefore with more material retained in soils. We highlighted that soils with higher OM loading retained a higher amount of freshly added OM, regardless of its already higher SOC saturation level and higher

SOC priming. This indicated that the retained OM addition in SOC depends on the current SOC stock. To obtain a better 'return on investment' of OM in soils, soil management should consider maintaining SOC storage by balancing the fresh C input with the initial SOC stock.

We elucidated how the topography of soil microaggregates influence OM sequestration by reconstructed 4D presentation of soil particles, combining the 3D architecture with surface element distribution. The curvature is introduced to describe the surface with concreate numbers. The surface with an incidence angle around 44.60° was demonstrated to be the preferential site to sequester freshly added OM. This advanced our understanding of MAOM formation on the surface of soil particles, and added specific knowledge of OM sequestration at the submicron scale.

5. Appendix

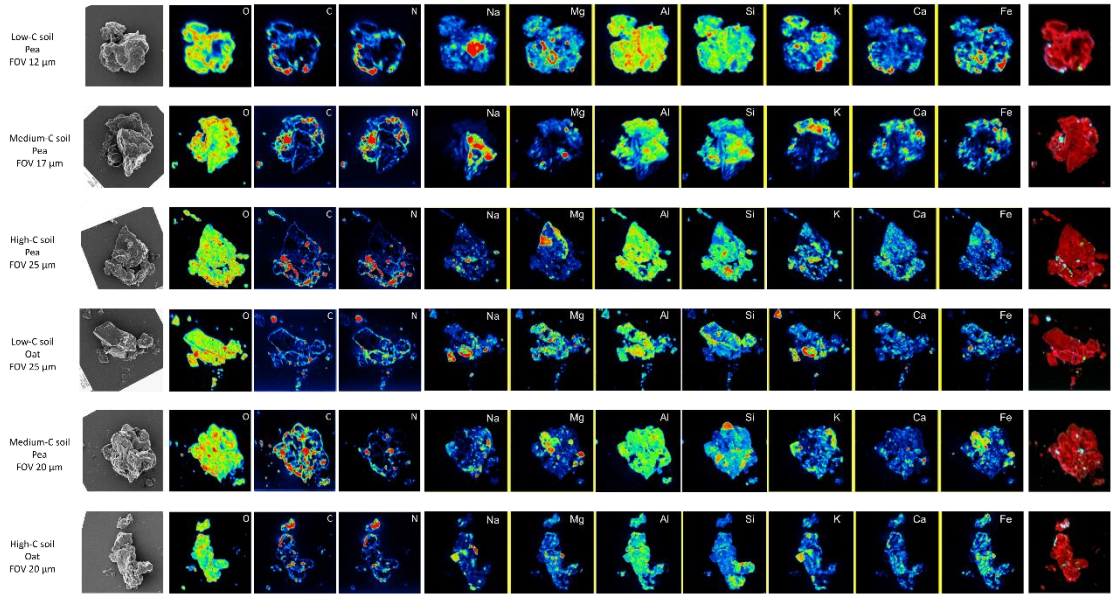

Figure 5 HIM images and NanoSIMS results of 6 soil particles. The HIM image, O, C, N, Na, Mg, Al, Si, K, Ca, Fe distribution, and RGB image were shown from left to right. In RGB images, red, green, and blue represent O, C, and N, respectively.

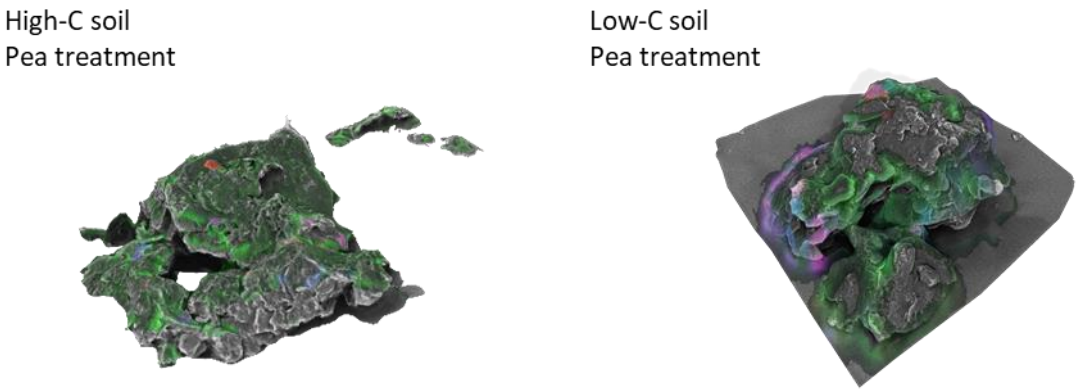

Figure 6 4D presentation of soil microaggregates (*Study 3*).

6. References

Akhtar, I., Rehman, M.A., Choi, W., Kumar, S., Lee, N., Cho, S.-J., Park, H.-H., Park, K.-H., Seo, Y., 2019. Three-dimensional atomic force microscopy for ultra-high-aspect-ratio imaging. Applied Surface Science 469, 582-592.

Amelung, W., Tang, N., Siebers, N., Aehnelt, M., Eusterhues, K., Felde, V.J., Guggenberger, G., Kaiser, K., Kögel-Knabner, I., Klumpp, E., 2024. Architecture of soil microaggregates: Advanced methodologies to explore properties and functions. Journal of Plant Nutrition and Soil Science 187, 17-50.

Angers, D., Recous, S., Aita, C., 1997. Fate of carbon and nitrogen in water-stable aggregates during decomposition of 13C15N-labelled wheat straw in situ. European Journal of Soil Science 48, 295-300.

Beare, M., McNeill, S., Curtin, D., Parfitt, R., Jones, H., Dodd, M., Sharp, J., 2014. Estimating the organic carbon stabilisation capacity and saturation deficit of soils: a New Zealand case study. Biogeochemistry 120, 71-87.

Blagodatskaya, E.V., Blagodatsky, S.A., Anderson, T.H., Kuzyakov, Y., 2007. Priming effects in Chernozem induced by glucose and N in relation to microbial growth strategies. Applied Soil Ecology 37, 95-105.

Bucka, F.B., Kölbl, A., Uteau, D., Peth, S., Kögel-Knabner, I., 2019. Organic matter input determines structure development and aggregate formation in artificial soils. Geoderma 354, 113881.

Castellano, M.J., Mueller, K.E., Olk, D.C., Sawyer, J.E., Six, J., 2015. Integrating plant litter quality, soil organic matter stabilization, and the carbon saturation concept. Global Change Biology 21, 3200-3209.

Chen, R., Senbayram, M., Blagodatsky, S., Myachina, O., Dittert, K., Lin, X., Blagodatskaya, E., Kuzyakov, Y., 2014. Soil C and N availability determine the priming effect: microbial N mining and stoichiometric decomposition theories. Global Change Biology 20, 2356-2367.

Christensen, B.T., 1992. Physical fractionation of soil and organic matter in primary particle size and density separates. Advances in soil science, 1-90.

Christensen, B.T., Sørensen, L.H., 1985. The distribution of native and labelled carbon between soil particle size fractions isolated from long-term incubation experiments. Journal of Soil Science 36, 219-229.

Cliff, J.B., Gaspar, D.J., Bottomley, P.J., Myrold, D.D., 2002. Exploration of inorganic C and N assimilation by soil microbes with time-of-flight secondary ion mass spectrometry. Applied and environmental microbiology 68, 4067-4073.

Córdova, S.C., Olk, D.C., Dietzel, R.N., Mueller, K.E., Archontouilis, S.V., Castellano, M.J., 2018. Plant litter quality affects the accumulation rate, composition, and stability of mineral-associated soil organic matter. Soil Biology and Biochemistry 125, 115-124.

Don, A., Rödenbeck, C., Gleixner, G., 2013. Unexpected control of soil carbon turnover by soil carbon concentration. Environmental Chemistry Letters 11, 407-413.

Felde, V.J., Schweizer, S.A., Biesgen, D., Ulbrich, A., Uteau, D., Knief, C., Graf-Rosenfellner, M., Kögel-Knabner, I., Peth, S., 2021. Wet sieving versus dry crushing: Soil microaggregates reveal different physical structure, bacterial diversity and organic matter composition in a clay gradient. European Journal of Soil Science 72, 810-828.

Feller, C., Beare, M.H., 1997. Physical control of soil organic matter dynamics in the tropics. Geoderma, 69-116.

Feng, W., Plante, A.F., Six, J., 2013. Improving estimates of maximal organic carbon stabilization by fine soil particles. Biogeochemistry 112, 81-93.

Fleming, Y., Wirtz, T., 2015. High sensitivity and high resolution element 3D analysis by a combined SIMS–SPM instrument. Beilstein Journal of Nanotechnology 6, 1091-1099.

Fleming, Y., Wirtz, T., Gysin, U., Glatzel, T., Wegmann, U., Meyer, E., Maier, U., Rychen, J., 2011. Three dimensional imaging using secondary ion mass spectrometry and atomic force microscopy. Applied Surface Science 258, 1322-1327.

Guillaume, T., Makowski, D., Libohova, Z., Bragazza, L., Sallaku, F., Sinaj, S., 2022. Soil organic carbon saturation in cropland-grassland systems: Storage potential and soil quality. Geoderma 406.

Hassink, J., 1997. The capacity of soils to preserve organic C and N by their association with clay and silt particles. Plant and soil.

Herrmann, A.M., Clode, P.L., Fletcher, I.R., Nunan, N., Stockdale, E.A., O'Donnell, A.G., Murphy, D.V., 2007a. A novel method for the study of the biophysical interface in soils using nano-scale secondary ion mass spectrometry. Rapid Communications in Mass Spectrometry: An International Journal Devoted to the Rapid Dissemination of Up-to-the-Minute Research in Mass Spectrometry 21, 29-34.

Herrmann, A.M., Ritz, K., Nunan, N., Clode, P.L., Pett-Ridge, J., Kilburn, M.R., Murphy, D.V., O'Donnell, A.G., Stockdale, E.A., 2007b. Nano-scale secondary ion mass spectrometry—A new analytical tool in biogeochemistry and soil ecology: A review article. Soil Biology and Biochemistry 39, 1835-1850.

Hillion, F., 1993. A new high performance instrument: The Cameca Nano-SIMS50, Proceedings of the 9^< th> SIMS conference, 1993.

Hoppe, P., 2006. NanoSIMS: A new tool in cosmochemistry. Applied Surface Science 252, 7102-7106.

Hoppe, P., Ott, U., Lugmair, G., 2004. NanoSIMS, the new tool of choice: 26Al, 44Ti, 49V, 53Mn, 60Fe, and more. New Astronomy Reviews 48, 171-176.

Inagaki, T.M., Possinger, A.R., Grant, K.E., Schweizer, S.A., Mueller, C.W., Derry, L.A., Lehmann, J., Kögel-Knabner, I., 2020. Subsoil organo-mineral associations under contrasting climate conditions. Geochimica et Cosmochimica Acta 270, 244-263.

Kaiser, K., Zech, W., 2000. Dissolved organic matter sorption by mineral constituents of subsoil clay fractions. Journal of Plant Nutrition and Soil Science 163(5), 531-535.

Keiluweit, M., Bougoure, J.J., Zeglin, L.H., Myrold, D.D., Weber, P.K., Pett-Ridge, J., Kleber, M., Nico, P.S., 2012. Nano-scale investigation of the association of microbial nitrogen residues with iron (hydr) oxides in a forest soil O-horizon. Geochimica et Cosmochimica Acta 95, 213-226.

Kögel-Knabner, I., Guggenberger, G., Kleber, M., Kandeler, E., Kalbitz, K., Scheu, S., Eusterhues, K., Leinweber, P., 2008. Organo-mineral associations in temperate soils: Integrating biology, mineralogy, and organic matter chemistry. Journal of Plant Nutrition and Soil Science 171, 61-82.

Kopittke, P.M., Berhe, A.A., Carrillo, Y., Cavagnaro, T.R., Chen, D., Chen, Q.-L., Román Dobarco, M., Dijkstra, F.A., Field, D.J., Grundy, M.J., He, J.-Z., Hoyle, F.C., Kögel-Knabner, I.,

Lam, S.K., Marschner, P., Martinez, C., McBratney, A.B., McDonald-Madden, E., Menzies, N.W., Mosley, L.M., Mueller, C.W., Murphy, D.V., Nielsen, U.N., O'Donnell, A.G., Pendall, E., Pett-Ridge, J., Rumpel, C., Young, I.M., Minasny, B., 2022. Ensuring planetary survival: the centrality of organic carbon in balancing the multifunctional nature of soils. Critical Reviews in Environmental Science and Technology, 1-17.

Labotka, T.C., Cole, D.R., Fayek, M., Riciputi, L.R., Stadermann, F.J., 2004. Coupled cation and oxygen-isotope exchange between alkali feldspar and aqueous chloride solution. American Mineralogist 89, 1822-1825.

Lechene, C., Hillion, F., McMahon, G., Benson, D., Kleinfeld, A.M., Kampf, J.P., Distel, D., Luyten, Y., Bonventre, J., Hentschel, D., 2006. High-resolution quantitative imaging of mammalian and bacterial cells using stable isotope mass spectrometry. Journal of biology 5, 1-30.

Lehmann, J., Solomon, D., Kinyangi, J., Dathe, L., Wirick, S., Jacobsen, C., 2008. Spatial complexity of soil organic matter forms at nanometre scales. Nature Geoscience 1, 238-242.

Lehndorff, E., Rodionov, A., Plümer, L., Rottmann, P., Spiering, B., Dultz, S., Amelung, W., 2021. Spatial organization of soil microaggregates. Geoderma 386, 114915.

Liang, A., Yang, X., Zhang, X., McLaughlin, N., Shen, Y., Li, W., 2009. Soil organic carbon changes in particle-size fractions following cultivation of Black soils in China. Soil and Tillage Research 105, 21-26.

Lu, M., Zhou, X., Luo, Y., Yang, Y., Fang, C., Chen, J., Li, B., 2011. Minor stimulation of soil carbon storage by nitrogen addition: A meta-analysis. Agriculture, Ecosystems & Environment 140, 234-244.

Lützow, M.v., Kögel-Knabner, I., Ekschmitt, K., Matzner, E., Guggenberger, G., Marschner, B., Flessa, H., 2006. Stabilization of organic matter in temperate soils: mechanisms and their relevance under different soil conditions - a review. European Journal of Soil Science 57, 426-445.

Mayer, L.M., 1994. Relationships between mineral surfaces and organic carbon concentrations in soils and sediments. Chemical Geology 114 (3-4), 347-363.

Mendoza, O., De Neve, S., Deroo, H., Li, H., Sleutel, S., 2022. Do interactions between application rate and native soil organic matter content determine the degradation of exogenous organic carbon? Soil Biology and Biochemistry 164.

Mueller, C.W., Hoeschen, C., Koegel-Knabner, I., 2023. Understanding of soil processes at the microscale—Use of NanoSIMS in soil science, In: Michael, J.G., Margaret, O. (Eds.), Encyclopedia of Soils in the Environment (Second Edition), Second Edition ed. Academic Press, Oxford, pp. 670-680.

Mueller, C.W., Kölbl, A., Hoeschen, C., Hillion, F., Heister, K., Herrmann, A.M., Kögel-Knabner, I., 2012. Submicron scale imaging of soil organic matter dynamics using NanoSIMS – From single particles to intact aggregates. Organic Geochemistry 42, 1476-1488.

Mueller, C.W., Remusat, L., Rumpel, C., 2017. Characterization of biogeochemical processes at the microscale: Concepts and applications of NanoSIMS. Terrestrial Ecosystem Research Infrastructures, 193-212.

Pohl, L., Kölbl, A., Uteau, D., Peth, S., Häusler, W., Mosley, L., Marschner, P., Fitzpatrick, R., Kögel-Knabner, I., 2021. Porosity and organic matter distribution in jarositic phyto tubules of sulfuric soils assessed by combined μCT and NanoSIMS analysis. Geoderma 399, 115124.

Post, W.M., Emanuel, W.R., Zinke, P.J., Stangenberger, A.G., 1982. Soil carbon pools and world life zones. Nature 298, 156-159.

Rasmussen, C., Heckman, K., Wieder, W.R., Keiluweit, M., Lawrence, C.R., Berhe, A.A., Blankinship, J.C., Crow, S.E., Druhan, J.L., Hicks Pries, C.E., 2018. Beyond clay: towards an improved set of variables for predicting soil organic matter content. Biogeochemistry 137, 297-306.

Remusat, L., Hatton, P.-J., Nico, P.S., Zeller, B., Kleber, M., Derrien, D., 2012. NanoSIMS study of organic matter associated with soil aggregates: advantages, limitations, and combination with STXM. Environmental Science & Technology 46, 3943-3949.

Rennert, T., Händel, M., Höschen, C., Lugmeier, J., Steffens, M., Totsche, K., 2014. A NanoSIMS study on the distribution of soil organic matter, iron and manganese in a nodule from a S tagnosol. European Journal of Soil Science 65, 684-692.

Rousk, J., Baath, E., 2007. Fungal and bacterial growth in soil with plant materials of different C/N ratios. FEMS Microbiol Ecol 62, 258-267.

Rowley, M.C., Grand, S., Verrecchia, É.P., 2018. Calcium-mediated stabilisation of soil organic carbon. Biogeochemistry 137, 27-49.

Rowley, M.C., Nico, P.S., Bone, S.E., Marcus, M.A., Pegoraro, E.F., Castanha, C., Kang, K., Bhattacharyya, A., Torn, M.S., Peña, J., 2023. Association between soil organic carbon and calcium in acidic grassland soils from Point Reyes National Seashore, CA. Biogeochemistry 165, 91-111.

Rui, Y., Murphy, D.V., Wang, X., Hoyle, F.C., 2016. Microbial respiration, but not biomass, responded linearly to increasing light fraction organic matter input: Consequences for carbon sequestration. Scientific Report 6, 35496.

Saggar, S., Parshotam, A., Sparling, G.P., Feltham, C.W., Hart, P.B.S., 1996. 14C-labelled ryegrass turnover and residence times in soils varying in clay content and mineralogy. Soil Biology and Biochemistry, 12.

Sarkar, B., Singh, M., Mandal, S., Churchman, G.J., Bolan, N.S., 2018. Clay Minerals—Organic Matter Interactions in Relation to Carbon Stabilization in Soils, The Future of Soil Carbon, pp. 71-86.

Scharlemann, J.P.W., Tanner, E.V.J., Hiederer, R., Kapos, V., 2014. Global soil carbon: understanding and managing the largest terrestrial carbon pool. Carbon Management 5, 81-91.

Schlesinger, W.H., 2005. Biogeochemistry.

Shabtai, I.A., Wilhelm, R.C., Schweizer, S.A., Höschen, C., Buckley, D.H., Lehmann, J., 2023. Calcium promotes persistent soil organic matter by altering microbial transformation of plant litter. Nature Communications 14, 6609.

Six, J., Conant, R.T., Paul, E.A., Paustian, K., 2002. Stabilization mechanisms of soil organic matter: Implications for C saturation of soils. Plant and soil 241(2), 155-176.

Six, J., Elliott, E.T., Paustian, K., 2000. Soil macroaggregate turnover and microaggregate formation: a mechanism for C sequestration under no-tillage agriculture. Soil Biology and Biochemistry 32, 2099-2103.

Solomon, D., Lehmann, J., Kinyangi, J., Liang, B., Heymann, K., Dathe, L., Hanley, K., Wirick, S., Jacobsen, C., 2009. Carbon (1s) NEXAFS spectroscopy of biogeochemically relevant reference organic compounds. Soil Science Society of America Journal 73, 1817-1830.

Stern, R.A., Fletcher, I.R., Rasmussen, B., McNaughton, N.J., Griffin, B.J., 2005. Ion microprobe (NanoSIMS 50) Pb-isotope geochronology at< 5 µm scale. International Journal of Mass Spectrometry 244, 125-134.

Stewart, C.E., Paustian, K., Conant, R.T., Plante, A.F., Six, J., 2007. Soil carbon saturation: concept, evidence and evaluation. Biogeochemistry 86, 19-31.

Stewart, C.E., Plante, A.F., Paustian, K., Conant, R.T., Six, J., 2008. Soil Carbon Saturation: Linking Concept and Measurable Carbon Pools. Soil Science Society of America Journal 72, 379-392.

Torn, M.S., Trumbore, S.E., Chadwick, O.A., Vitousek, P.M., Hendricks, D.M., 1997. Mineral control of soil organic carbon storage and turnover. Nature 389, 170-173.

Trivedi, P., Delgado-Baquerizo, M., Jeffries, T.C., Trivedi, C., Anderson, I.C., Lai, K., McNee, M., Flower, K., Pal Singh, B., Minkey, D., 2017. Soil aggregation and associated microbial communities modify the impact of agricultural management on carbon content. Environmental microbiology 19, 3070-3086.

Vidal, A., Remusat, L., Watteau, F., Derenne, S., Quenea, K., 2016. Incorporation of 13C labelled shoot residues in Lumbricus terrestris casts: A combination of transmission electron microscopy and nanoscale secondary ion mass spectrometry. Soil Biology and Biochemistry 93, 8-16.

Vogel, C., Mueller, C.W., Hoschen, C., Buegger, F., Heister, K., Schulz, S., Schloter, M., Kogel-Knabner, I., 2014. Submicron structures provide preferential spots for carbon and nitrogen sequestration in soils. Nat Commun 5, 2947.

Wang, Q., Chen, L., Yang, Q., Sun, T., Li, C., 2019. Different effects of single versus repeated additions of glucose on the soil organic carbon turnover in a temperate forest receiving long-term N addition. Geoderma 341, 59-67.

Wang, Q., Wang, S., He, T., Liu, L., Wu, J., 2014. Response of organic carbon mineralization and microbial community to leaf litter and nutrient additions in subtropical forest soils. Soil Biology and Biochemistry 71, 13-20.

Wiesmeier, M., Munro, S., Barthold, F., Steffens, M., Schad, P., Kögel-Knabner, I., 2015. Carbon storage capacity of semi-arid grassland soils and sequestration potentials in northern China. Global Change Biology 21, 3836-3845.

Wiesmeier, M., Urbanski, L., Hobley, E., Lang, B., von Lützow, M., Marin-Spiotta, E., van Wesemael, B., Rabot, E., Ließ, M., Garcia-Franco, N., Wollschläger, U., Vogel, H.-J., Kögel-Knabner, I., 2019. Soil organic carbon storage as a key function of soils - A review of drivers and indicators at various scales. Geoderma 333, 149-162.

Wirtz, T., Fleming, Y., Gerard, M., Gysin, U., Glatzel, T., Meyer, E., Wegmann, U., Maier, U., Odriozola, A.H., Uehli, D., 2012. Design and performance of a combined secondary ion mass spectrometry-scanning probe microscopy instrument for high sensitivity and high-resolution elemental three-dimensional analysis. Review of Scientific Instruments 83.

Wu, T., Ost, A.D., Audinot, J.-N., Wiesmeier, M., Wirtz, T., Buegger, F., Häusler, W., Höschen, C., Mueller, C.W., 2022. Association of fresh low-molecular-weight organic compounds with clay-sized mineral fraction in soils of different organic carbon loading. Geoderma 409.

7. List of publications

Study 1

Wu, T., Ost, A. D., Audinot, J. N., Wiesmeier, M., Wirtz, T., Buegger, F., Häusler, W., Höschen, C., & Mueller, C. W.

Association of fresh low-molecular-weight organic compounds with clay-sized mineral fraction in soils of different organic carbon loading

Geoderma 409 (2022) 115657

https://doi.org/10.1016/j.geoderma.2021.115657

Geoderma 409 (2022) 115657

Contents lists available at ScienceDirect

Geoderma

journal homepage: www.elsevier.com/locate/geoderma

Association of fresh low-molecular-weight organic compounds with clay-sized mineral fraction in soils of different organic carbon loading

Tianyi Wu [a,*], Alexander D. Ost [b,c], Jean-Nicolas Audinot [b], Martin Wiesmeier [a,d], Tom Wirtz [b], Franz Buegger [e], Werner Häusler [a], Carmen Höschen [a], Carsten W. Mueller [f]

[a] Soil Science, TUM School of Life Sciences, Technical University of Munich, D-85354 Freising-Weihenstephan, Germany
[b] Advanced Instrumentation for Nano-Analytics (AINA), Materials Research and Technology Department (MRT), Luxembourg Institute of Science and Technology (LIST), L-4362 Belvaux, Luxembourg
[c] University of Luxembourg, L-4365 Esch-sur-Alzette, Luxembourg
[d] Bavarian State Research Center for Agriculture, Institute for Organic Farming, Soil and Resource Management, D-85354 Freising, Germany
[e] Institute of Biochemical Plant Pathology, Helmholtz Zentrum München, German Research Center for Environmental Health, D-85764 Neuherberg, Germany
[f] Department of Geosciences and Natural Resource Management, University of Copenhagen, DK-1350 Copenhagen, Denmark

ARTICLE INFO

Handling Editor: Daniel Said-Pullicino

Keywords:
Carbon saturation
Soil C loading
N content
Stable isotope tracing
C retention
Low-molecular-weight organic compounds

ABSTRACT

Although the association of minerals and organic matter (OM) in soil plays an important role in the sequestration of C, the factors driving the initial formation of mineral-associated OM (MAOM), and thus the retention of new C input in soils are not yet fully understood. In this study, we investigated how the soil C loading and the differences in the N content of low-molecular-weight organic compound (LMWOC) input foster the rapid C retention in the soil's fine mineral fractions (clay and fine silt-sized fraction). Two topsoils (0–10 cm) with different C loading due to different long-term management (direct seeding vs. bare fallow) derived from an agricultural research trial were used for the short-term incubation experiment. In a 24-hour incubation experiment, we used two labeled substrates (without N, glucose, > 99% ^{13}C and with N, amino acid mixture, > 98% ^{13}C, > 98% ^{15}N) to investigate how the different N content delivered by the LMWOC input determine the fate of newly formed OM in the MAOM pool. Our results show that the soil with low C loading and thus a low C saturation level retained more freshly added LMWOC in the fine MAOM pool compared to the high C-loading soil, demonstrating that the soil C loading is a major factor controlling the retention of freshly added OM at the early stage of MAOM formation. The LMW OM containing N significantly enhanced the recovery of freshly added LMWOC in the low C-loading soil but not in the high C-loading soil. This points to the great importance of the N availability for the retention of freshly added OM in soils. Our study showed that the level of the native OM content affects the fast retention of freshly added OM in the clay-sized fraction to a greater extent than the N availability of the OM substrate.

1. Introduction

Soils store large amounts of organic matter (OM) and represent the largest terrestrial carbon (C) pool (Scharlemann et al., 2014; Schlesinger, 2005). Considerable work has been done to understand soil organic carbon (SOC) stabilization mechanisms (Basile-Doelsch et al., 2020), as the persistence of C in soils is of great significance concerning global climate change and agricultural services (Lal, 2004). The amount of more persistent soil C is mainly regulated by the interaction of OM with mineral surfaces and the reduced bioaccessibility within soil aggregates, namely as mineral-associated organic matter (MAOM) and as OM occluded within soil aggregates (Christensen, 1992; JASTROW, 1996; von Lützow et al., 2007). The MAOM was demonstrated to have rather longer turnover times and thus sustain the persistence of C in soils (von Lützow et al., 2007). Therefore, the interaction of OM and mineral surfaces (organo-mineral interaction) is considered as one of the main factors that control soil C storage. Accordingly, a major focus was put on the study of the cycling and fate of MAOM in recent years (Kleber et al.,

* Corresponding author.
E-mail addresses: tianyi.wu@tum.de (T. Wu), alexander.ost@list.lu (A.D. Ost), jean-nicolas.audinot@list.lu (J.-N. Audinot), Martin.Wiesmeier@lfl.bayern.de (M. Wiesmeier), tom.wirtz@list.lu (T. Wirtz), buegger@helmholtz-muenchen.de (F. Buegger), haeusler@wzw.tum.de (W. Häusler), carmen.hoeschen@wzw.tum.de (C. Höschen), cm@ign.ku.dk (C.W. Mueller).

https://doi.org/10.1016/j.geoderma.2021.115657
Received 8 July 2021; Received in revised form 5 December 2021; Accepted 7 December 2021
Available online 16 December 2021

Table 1
Basic soil characteristics of low-C and high-C soil before incubation, including C and N contents, C to N ratio, pH-values and electrical conductivity (EC) measured in H_2O.

Soil	Total C content (mg g^{-1})	Total N content (mg g^{-1})	C/N	pH	EC	Fe content (mg g^{-1})
Low-C	6.1 ± 0.0	0.7 ± 0.0	8.7 ± 0.0	6.4	54.2	9.8 ± 0.2
High-C	17.4 ± 0.3	1.8 ± 0.0	9.9 ± 0.0	7.6	67.2	14.2 ± 0.2

2015; Lehmann and Kleber, 2015).

To better understand the fate and the properties of MAOM, physical fractionation using density and particle size is commonly applied to differentiate between different SOM fractions (Kögel-Knabner et al., 2008; Poeplau et al., 2018). It was shown that the amount of persistent SOM correlates with the amount of fine mineral particles (<20 μm) (Feller and Beare, 1997) and the type of clay minerals (Denef et al., 2004), for instance, 2:1 layer silicate sequestrated a higher amount of organic compounds than 1:1 layer silicate (Saidy et al., 2013; Wang and Xing, 2005). As more than half of the total OM in temperate arable soils is concentrated in the clay-sized fraction (<2 μm) (Christensen, 2001), it is crucial to better understand the OM cycling in the fine mineral fractions. In many soils, the fine-sized mineral fraction contributes considerably more to SOM preservation compared to particulate OM (Kleber et al., 2015; Leifeld et al., 2009; Torn et al., 2013). Partly this is due to the high specific surface area (SSA) of the fine-sized mineral fraction that was demonstrated to positively correlate with the amount of stored SOC (Hassink, 1997; Six et al., 2002).

Although the SSA plays an important role in SOM storage via organo-mineral associations, the OM input determines the accumulation of SOM in general (Kaiser and Guggenberger, 2003). Soil OM content and its composition is mainly driven by the quantity and also N content of the plant-derived OM input (Dungait et al., 2012; Grandy and Neff, 2008). The mass ratio of C to N of most plant litter is above 20 (Paul, 2016; Zhang et al., 2019), while that of MAOM is between 8 and 13 (Hassink et al., 1993; von Lützow et al., 2007), which resembles the C/N ratio of microorganisms of around 8 and thus the increased amount of microbial transformed OM, including microbial biomass and necromass (microbial residues) (Buckeridge et al., 2020; Liang et al., 2019; Miltner et al., 2012). Experiments studying short-term effects of OM substrate often focus more on the low-molecular-weight organic compounds (LMWOC) absorbed within the soils and the direct microbial uptake and mineralization (Creamer et al., 2014; Fischer et al., 2010). The rapid microbial transformation of plant-derived OM and its fate as MAOM in fine-sized soil mineral fractions is less understood.

The soil OC content was suggested to be directly linked to the N content of the OM input material (Jilling et al., 2020; Kleber et al., 2007; Kopittke et al., 2020). Studies on the relation of N addition and alterations of SOC stocks demonstrated that in both short-term incubation and long-term field experiments SOC stocks increased when additional N was applied (Cotrufo et al., 2013; Kirchmann et al., 2004; Wang et al., 2019). In contrast, other studies showed that the SOC content is not always significantly related to N addition (Brown et al., 2014; Campbell et al., 1991; Reicosky et al., 2002). Other authors also pointed out that although the N content of OM input is an important factor, the overall accumulation of SOC seems to be more controlled by the quantity of the OM input (Gentile et al., 2011; Lu et al., 2011).

A concept of soil C saturation was proposed, which suggested that an upper limit of C content exists for the soil C pool and this capacity limits the further increase of more persistent SOC with OM input (Six et al., 2002). The research of C saturation effects on agricultural soils indicated that the C input by aboveground crop residues (e.g. litter, straw) roots and rhizodeposition is usually too low to show a considerable saturation effect, although it was demonstrated that the total SOC pool has an upper limit (Stewart et al., 2007; Stewart et al., 2008). Soil OC in agricultural soils is mainly stored in mineral fractions < 20 μm and thus the capacity to store OC is mainly determined by the soil texture (Hassink, 1997). According to the author, the maximal soil C storage is dependent on climate, topography, parent material, organisms and soil properties, which can be expressed in various linear regressions of the maximum SOC content (Wiesmeier et al., 2019). Thus, for a specific soil texture the SOC storage can be estimated using the appropriate equation according to the climate, land use and clay type (Eq. (5) in this case). Each soil has a typical OC storage capacity, the amount of which generally remains static. However, the soil C and N contents are constantly circulating out into the environment, to be replaced by new C and N. In this way, they maintain a dynamic equilibrium (Six et al., 2004). This idea of the dynamic behavior of SOM addresses the point that the overall SOC storage is different from SOC retention (Chenu et al., 2018) since C retention is a process (Lal et al., 2015). Soil C retention depends on both C stabilization and destabilization. Recent studies on SOC retention focusing on MAOM demonstrated a more efficient C retention with the input of higher N availability compared to low N available OM (Cotrufo et al., 2013). However, this occurs only when the soil is unsaturated with OC in the MAOM fraction (Castellano et al., 2015; Lavallee et al., 2020). Studies on the destabilization of native SOC due to the addition of LMWOC demonstrated that the amount of soil C lost correlated with the N content of the added LMWOC substrate (Blagodatskaya et al., 2007; Keiluweit et al., 2015).

Yet, it is not well understood how the N content of OM input controls the rates of the rapid C retention in the MAOM pool, and how the SOC loading affects the short-term retention of freshly added C. Many studies focused on long-term experimental field trials but only a few pieces of information exist about the SOC stock on a very short timescale. Short-term incubation studies have been primarily concerned with microbial activities involving the LMWOC, and consequently missed the rapid LMWOC retention as MAOM on soil fine fractions.

Here, we performed a short-term experiment applying two LMWOC substrates on agricultural soils with different SOC saturation levels as a result of different long-term management. The objectives were to investigate how soil C loading and the N availability of the LMWOC impact the initial retention of C in the MAOM pool. We hypothesized that (1) the soil carbon saturation level influences the short-term retention of LMWOCs, and (2) the soil C loading and the N content of the substrate control the recovery of newly added OM in MAOM.

2. Materials and methods

2.1. Soil samples

To compare soils with different degrees of C loading, we sampled agricultural soils from long-term field experiments maintained by the Bavarian State Research Center for Agriculture (LfL). The experimental sites are located in Puch (southern Germany, 48°11′37.0″N, 11°12′57.4″E) at an elevation of 550 m a.s.l. with a mean annual temperature of 8.8 °C and mean annual precipitation of 872 mm. The experiments comprised sites under different crop rotations and tillage systems with a wide SOC gradient as a result of different C inputs over several decades. For this study we selected a site (10 × 15 m) with a typical rotation including winter wheat (Triticum aestivum), grain maize (Zea mays), winter rapeseed (Brassica napus) and spring barley (Hordeum vulgare) under direct seeding started in 1992 and a bare fallow (5 × 50 m) experiment started in 1953, where no crops were cultivated and potential C input by germinating plants was prevented by monthly plowing. The two experimental sites are in close vicinity and comparable in terms of soil mineralogy (see Fig. A.1 in appendices). Soils were characterized as Luvisols derived from Loess deposits (IUSS Working Group WRB, 2015). Soil samples were taken from the upper 10 cm of the Ap horizon from 20 random locations of each plot and thoroughly mixed to form composite samples. The fresh soil material was

Table 2
Soil texture of low-C and high-C soil before incubation, demonstrating as distribution of clay, silt and sand.

Fractions	Clay (%)	Fine silt (%)	Medium silt (%)	Coarse silt (%)	Fine sand (%)	Medium sand (%)	Coarse sand (%)
Particle size (μm)	< 2	2–6.3	6.3–20	20–63	63–200	200–630	630–2000
Low-C soil	28.6	11.1	22.8	25.4	7.0	3.8	1.3
High-C soil	38.8	10.1	18.5	17.4	8.1	5.3	1.8

air-dried at room temperature and subsequently sieved to 2 mm and macroscopic plant residues were picked out by hand. Basic soil characteristics and texture of the two soils are given in Table 1 and Table 2.

Soil pH and electrical conductivity were measured in the soil suspension (soil to water ratio of 1:5 (w/v)) after shaking for 1 h and sitting for 1 h. The Fe was extracted by citrate bicarbonate dithionite procedure according to Holmgren (1967), and measured by using inductively coupled plasma optical emission spectrometry (ICP-OES, Vista Pro CCD Simultaneous, Varian, Darmstadt, Germany).

For soil texture analyses, all soils were treated with 30%–H_2O_2 to remove OC, and subsequently with 0.0025 M sodium pyrophosphate ($Na_4P_2O_7$) to ensure dispersion of primary particles. Subsequently, ultrasonic dispersion was performed in 0.0025 M $Na_4P_2O_7$ suspension at 450 J ml^{-1}. Wet sieving was used to separate the particle size classes 630–2000 μm, 200 – 630 μm, 63 – 200 μm and < 63 μm. The suspensions < 63 μm were freeze-dried and an aliquot was analyzed after resuspending in 0.0025 M $Na_4P_2O_7$ using x-ray absorption (Sedigraph III Plus (Micromeritics, Aachen, Germany).

Carbon and nitrogen contents of both bulk soil materials were determined before the experiment in duplicate by dry combustion using a CN elemental analyzer (HEKAtech, Wegberg, Germany). The soil under bare fallow revealed C and N contents of 6.4 mg g^{-1} and 0.8 mg g^{-1}, respectively, and the soil managed by direct seeding revealed C and N contents of 17.9 mg g^{-1} and 1.9 mg g^{-1}, respectively. In the following we refer to bare fallow as low-carbon (low-C) and to direct seeding as high-carbon (high-C) soil. As the studied soils show no differences in clay mineralogy (Fig. A1, in appendix), it can be assumed that the formation processes of mineral-associated OM are comparable between the soils.

2.2. Low-molecular-weight organic substrate experiment

To elucidate the direct incorporation of freshly added substrates with differing C/N ratios we used two low-molecular-weight (LMW) substrates, both enriched in ^{13}C and one enriched in ^{15}N (D-Glucose-$^{13}C_6$, Sigma-Aldrich, ≥ 99 atom% ^{13}C and algal amino acid mixture, Sigma-Aldrich, ≥ 98 atom-% ^{13}C and ≥ 98 atom-% ^{15}N). This approach allowed us to trace the fate of C and N into soil microstructures of the two soil materials with different C loading. The glucose was chosen as an extreme substrate that contained no N. The amino acid mixture was chosen due to its N being delivered together with C, whilst the mixture of 16 amino acids weakened the impact of a certain group of amino acids.

The amount of C input with these substrates was based off of the mean C input (3.2 t ha^{-1} yr^{-1}) at the research site Puch (Wiesmeier et al., 2014a). This was done under the assumption that the majority of the C input localizes in the top 10 cm of the soil with a bulk density of 1.3 g cm^{-3}, thus accordingly the calculated C input is 0.82 mg g^{-1} soil. In brief, five grams (dry weight) of sieved fresh soil were filled into a 100 mL centrifuge tube (Ultra-High Performance, VWR). Each treatment including the control was set up with 3 replicates. To allow homogeneous mixing of the glucose and amino acid with the soils, the LMW substrates were added as solutions. The LMW substrates were weighed into beakers and dissolved into 25 mL deionized water to obtain the solution of 2.183 mg glucose mL^{-1} and 2.169 mg amino acid mL^{-1}, respectively. For the treatment setup, 25.2 μL solution, containing 0.273 mg ^{13}C, was added into the tube for each gram of soil. Furthermore, the amino acid treated soil obtained 0.18 mg ^{15}N g^{-1} soil via the substrate addition. All substrate-amended soil samples were brought to the moisture level of 50% field capacity. The same volume of deionized water was added to the control group to adjust the moisture to the same level as the LMWOC amended soils. In each setup, a glass rod was used to stir and homogenize the mixture. The tubes were sealed subsequently with lids and were kept in dark at 20 °C for 24 h. After 24 h all samples were freeze-dried to directly disrupt any biological activity and yield dry soil material.

2.3. Density fractionation

To obtain the clay-sized mineral-associated OM fraction, a density fractionation procedure adapted from Golchin et al. (1994) was used. The procedure ensured a good separation of particulate organic matter (POM) and mineral-associated organic matter (MAOM), to avoid any bias from translocated POM in the later-to-be analyzed microaggregate MAOM samples.

In brief, approximately three grams of freeze-dried soil sample were used for the soil fractionation. The soil samples were submerged in 50 mL sodium polytungstate (NaPWO4) with a density of 1.8 g cm^{-3} and dispersed using an ultrasonicator with an energy input of 480 J mL^{-1}. After centrifugation (3500 rpm, 30 min, 20 °C), the floating light particulate OM (POM) fraction was collected via a vacuum system. Both light fraction and heavy fraction (MAOM) were washed with deionized water using a pressure filtration (0.45 μm filter pore size) to remove excess salt until the electric conductivity dropped below 50 μS cm^{-1}. The heavy fraction was separated into three size fractions - clay (<2 μm), fine silt (2–6.3 μm) and silt and sand (>6.3 μm) - by sedimentation and subsequently freeze-dried.

2.4. Chemical and mineralogical analysis

The ^{13}C and ^{15}N enrichment, as well as the total carbon (C) and nitrogen (N) concentrations of bulk soils and soil fractions after the adsorption experiment, were measured by an Isotope ratio mass spectrometer (IRMS, Delta V Advantage, Thermo Fisher, Dreieich, Germany), coupled to an elemental analyzer (EuroEA, Eurovector, Pavia, Italy). The enrichment is given in atom-% (at%).

The multi-point BET method (Chiou et al., 1993; Heister, 2014) was used to determine the specific surface area (SSA) of clay and fine silt-sized MAOM fractions. Nitrogen was employed as an adsorbate. The samples were outgassed at 40 °C for 23 h and then measured at 77 K.

X-ray powder diffraction (XRD) was carried out on a Philips PW 1820 diffractometer, using Co Kα radiation (λ = 1.7902 Å) for all clay and fine silt-sized mineral fractions. The freeze-dried powder samples (random powder preparation) were measured from 2° to 26° 2θ in steps of 0.02° 2θ with a counting time of 5 s for each step. The mineralogy was assigned according to Moore and Reynolds Jr (1989). Each mineral phase was determined by semiquantitative evaluation in accordance with Niederbudde (1973) and Stanjek and Häusler (2000).

2.5. Calculations and statistical analysis

In the clay and fine silt-sized fractions, the ^{13}C excess and ^{15}N excess were calculated using Eq. (1):

$$Excess_x(at\%) = At_{fraction}(at\%) - At_{control}(at\%) \quad (1)$$

The x stands for the isotopes ^{13}C or ^{15}N. The $Excess_x$ represents the ^{13}C excess or ^{15}N excess. $At_{fraction}$ and $At_{control}$ represent the ^{13}C at% or ^{15}N

Table 3
Total C and N contents and C to N ratios of bulk soil, clay and fine silt-sized fractions of low-C soil and high-C soil after 24 h of incubation.

		Total C content (mg *g^{-1})			Total N content (mg *g^{-1})			C to N ratio		
Soil		Control	Glucose	Amino acid	Control	Glucose	Amino acid	Control	Glucose	Amino acid
Low-C	Bulk soil	6.1 ± 0.0	6.6 ± 0.1	6.7 ± 0.1	0.7 ± 0.0	0.7 ± 0.0	0.8 ± 0.0	8.7 ± 0.0	8.9 ± 0.1	8.1 ± 0.0
	Clay	23.8 ± 0.6	23.6 ± 0.3	23.1 ± 0.1	3.4 ± 0.1	3.3 ± 0.0	3.4 ± 0.1	7.0 ± 0.1	7.1 ± 0.1	6.8 ± 0.1
	Fine silt	7.2 ± 1.2	8.4 ± 0.7	9.2 ± 0.9	0.9 ± 0.2	1.0 ± 0.1	1.1 ± 0.2	8.4 ± 0.5	8.2 ± 0.3	8.3 ± 0.4
High-C	Bulk soil	17.4 ± 0.3	18.7 ± 0.5	19.0 ± 0.1	1.8 ± 0.0	1.9 ± 0.0	2.0 ± 0.0	9.9 ± 0.0	10.0 ± 0.2	9.7 ± 0.1
	Clay	39.8 ± 4.6	38.7 ± 1.7	39.3 ± 0.4	4.9 ± 0.4	4.8 ± 0.1	4.7 ± 0.1	8.0 ± 0.4	8.3 ± 0.1	8.3 ± 0.2
	Fine silt	24.4 ± 0.6	27.3 ± 1.4	30.0 ± 0.2	2.1 ± 0.1	2.3 ± 0.1	2.6 ± 0.2	11.6 ± 0.4	11.3 ± 0.4	11.6 ± 0.2

Table 4
The SOC saturation level of the low-C and high-C soil used for the incubation experiment. The calculation of the SOC saturation level was adapted from Wiesmeier et al. (2019).

	Fraction < 6.3 μm (%)	SOC capacity (mg *g^{-1})	SOC content of fraction < 6.3 μm (mg *g^{-1})	SOC saturation level
Low-C soil	40	14	4.8	33%
High-C soil	49	17	12.9	75%

at% values of the size fraction and control, respectively.

The substrate-derived isotope in each fraction was calculated using Eq. (2):

$$f_x = Excess_x(at\%)/At_{substrate}(at\%) - At_{control}(at\%) \quad (2)$$

The fx represents the proportion ^{13}C or ^{15}N derived from the substrate. $At_{substrate}$ and $At_{control}$ represent the ^{13}C at% or ^{15}N at% values of the substrate and control, respectively.

The amount of substrate derived ^{13}C ($Substrate_x$) in each fraction was calculated using Eq. (3):

$$Substrate_x(mg*g^{-1}) = f_x*c\ (mg*g^{-1}) \quad (3)$$

where the c is the C content of the fraction, using mg *g^{-1} as the unit.

The recovery of ^{13}C (R_x) of the bulk soil in each fraction was calculated using Eq. (4):

$$R_x(\%) = Substrate_x(mg*g^{-1})*f(\%)/C_{input}(mg*g^{-1}) \quad (4)$$

where the f is the content of the size fraction and C_{input} is the C input of the bulk soil, expressed in mg *g^{-1}.

The recovery of ^{15}N is calculated with the same principle.

The estimation of the SOC storage capacity was adapted from Feng et al. (2014) and Wiesmeier et al. (2019) using Eq. (5):

$$Capacity_{SOC} = 1.68 + 0.32*ff < 6.3\mu m \quad (5)$$

The $ff < 6.3\mu m$ represents the content of the mineral fractions smaller than 6.3 μm, determined by soil texture analysis.

The C content in the fraction smaller than 6.3 μm in the soil samples was calculated according to Eq. (6):

$$C\%_{<6.3\mu m}(mg*g^{-1}) = C\%_{Clay}(mg*g^{-1})*f_{Clay}\% + C\%_{Finesilt}(mg*g^{-1})*f_{Finesilt}\% \quad (6)$$

Where $C\%_{Clay}$ and $C\%_{Finesilt}$ stand for the C content of clay and fine silt-sized fractions, using mg *g^{-1} as the unit. The $f_{Clay}\%$ and $f_{Finesilt}\%$ represent the clay and fine silt-sized fraction content of the soil.

The SOC saturation level ($L_{Saturation}$) of the soils was calculated using Eq. (7):

$$L_{Saturation}(\%) = C\%_{<6.3\mu m}\ (mg*g^{-1})/Capacity_{SOC}(mg*g^{-1})*100(\%) \quad (7)$$

A one-way analysis of variance (ANOVA) with Tukey test was carried out using Origin 2020 (OriginLab) for statistical analysis of the IRMS and BET datasets. Tow treatments in two soils were treated as 4 samples in the statistical analysis. Differences between subsamples within each fraction were tested separately. The differences were considered significant when $p < 0.05$. Other data, except the soil texture, are presented as mean values of the three replicates with standard deviation. The soil texture was measured using a larger quantity of the homogenized bulk soil that was used for the incubation experiments without replicates and thus no standard deviation is given.

3. Results

3.1. Total carbon and nitrogen content

After 24 h of incubation, total C and N contents were measured for the recovered fine mineral fractions. Since the amount of the LMW substrates (0.27 mg C *g^{-1} dry soil) was low compared to the native SOM, all incubated soils showed no change in their total C and N content (Table 3), due to the OM addition. The C-to-N ratio of the incubated soils was 8.7 (low-C soil) and 9.9 (high-C soil). In both soils, the clay fractions showed higher C contents than the fine silt fractions. The clay fractions ($n = 3$) of the low-C soil contained 23.5 ± 0.5 mg *g^{-1}C and 3.4 ± 0.1 mg *g^{-1}N (Table 3) after the 24 h incubation. The C and N contents of the fine silt-sized fraction of the low-C soil were 8.3 ± 1.24 mg *g^{-1} and 1.0 ± 0.2 mg *g^{-1}, respectively. The high-C soil contained 39.2 ± 2.3 mg *g^{-1}C and 4.8 ± 0.3 mg *g^{-1}N in the clay-sized fraction while it contained 27.2 ± 2.8 mg *g^{-1}C and 2.4 ± 0.3 mg *g^{-1}N in the fine silt-sized fraction.

3.2. SOC saturation level

The bulk soil capacity to store SOC was estimated according to Feng et al. (2014) using Eq. (5). The calculated capacity for low-C soil and high-C soils is 14 mg C and 17 mg C of each gram of soil (Table 4), respectively. The SOC content in the fine mineral fraction (<6.3 μm) of the low-C soil was 4.8 mg *g^{-1}, while the high-C soil contained 12.9 mg *g^{-1} SOC. The calculation of the SOC saturation level (Eqs. (6) and (7)) demonstrates that the low-C soil has a low saturation of 33%, while the SOC saturation of the high-C soil reaches 75% of the calculated potential SOC storage capacity.

3.3. Recovery of substrate-derived ^{13}C and ^{15}N in MAOM fractions

The ^{13}C excess and ^{15}N excess were calculated based on the ^{13}C and ^{15}N contents in the clay and fine silt-sized OM fractions according to Eq. (1) (Fig. 1, A, B). For both clay and fine silt-sized MAOM of low-C soil and high-C soil, it could be demonstrated that the glucose and amino acid addition lead to a significant enrichment in ^{13}C (Fig. 1, A). For the ^{13}C excess of fine silt-sized MAOM of the low-C soil, no significant differences were detectable both for glucose and the amino acid treatment, with a ^{13}C excess of around 0.7%. For the high-C soil a lower ^{13}C excess compared to the low-C soil was demonstrated for all MAOM fractions (Fig. 1, A). Except for the glucose treatment of the low-C soil, the clay-sized fraction showed a greater ^{13}C excess and ^{15}N excess (Fig. 1, B) than the fine silt-sized fraction. For the low-C soil MAOM fractions, the clay-

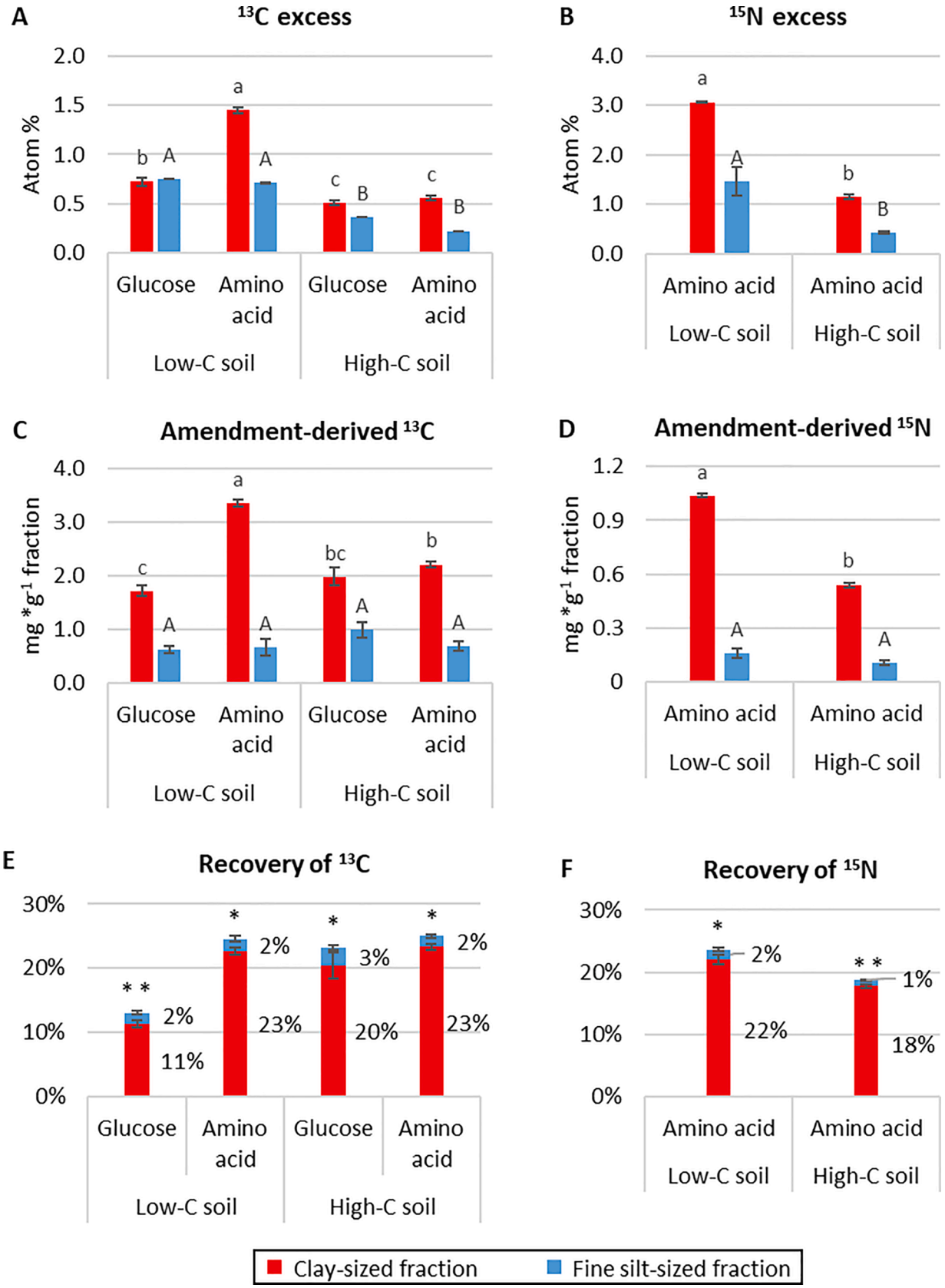

Fig. 1. ^{13}C excess (A), ^{15}N excess (B), substrate-derived ^{13}C (C) and ^{15}N (D) of clay and fine silt-sized MAOM of low-C and high-C soils after 24 h incubation with glucose or amino acid addition. The recovery of ^{13}C (E) and ^{15}N (F) of clay and fine silt-sized fractions of low-C and high-C soils after 24 h incubation with glucose or amino acid addition. Lowercase letters, capital letters and asterisks (*) represent significant differences ($P < 0.05$) between clay-sized MAOM fractions, fine silt sized MAOM and clay plus fine silt-sized MAOM, respectively.

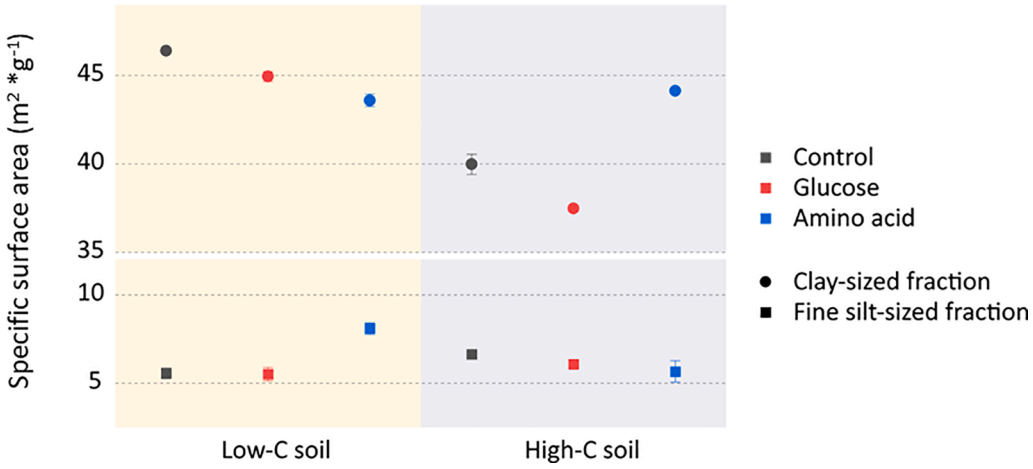

Fig. 2. BET analysis on clay and fine silt-sized fractions of each treatment.

sized fraction amended with amino acids showed a ^{13}C excess of 1.4%, which was twice the glucose-amended soil fractions (0.7%). For both soils, a two-times higher ^{15}N excess was demonstrated for the clay-sized MAOM fractions (3.1% for low-C soil, 1.1% for high-C soil) compared to the fine silt-sized MAOM fractions (1.5% for low-C soil, 0.4% for high-C soil).

The substrate-derived ^{13}C and ^{15}N demonstrated a higher amount for the clay-sized MAOM than the fine silt-sized MAOM (Fig. 1, C, D). In both low-C and high-C soils amended with glucose and amino acid, the substrate-derived ^{13}C ranged between 1.7 and 3.3 mg $*g^{-1}$ on clay-sized MAOM fractions but that of fine silt MAOM fractions were below 1 mg $*g^{-1}$ (Fig. 1, C). In the amino acid amended soils, 1.0 mg $*g^{-1}$ (low-C soil) and 0.5 mg $*g^{-1}$ (high-C soil) of the substrate-derived ^{15}N retained on the clay-sized MAOM, 5 times higher than the fine-silt MAOM (0.2 mg $*g^{-1}$ for low-C soil, 0.1 mg $*g^{-1}$ for high-C soil).

After 24 h of incubation, the total recovery of the substrate-derived ^{13}C in the bulk soils of all treatments ranged between 45% – 53% (data not shown). The MAOM of the clay-sized fraction retained a larger amount of substrate-derived C and N than the fine silt fraction. In the low-C soil, 11% of the glucose-derived C was retained in the clay-sized fraction, while 20% glucose-derived C was retained in the clay-sized fraction of the high-C soil. The recovery of fresh amino acid derived ^{13}C in the clay fraction of both soils was 23%. However, only 2–3% of substrate-derived C was recovered in the fine silt-sized fractions (2–6.3 μm) for both glucose and amino acid substrates.

3.4. The specific surface area of fine-sized mineral fractions

The specific surface area (SSA) of clay and fine silt-sized fractions of each treatment (Fig. 2) were determined by BET analyses (Mayer, 1994b). For the clay-sized fractions of the control treatments, the SSA of the low-C soil (46.4 $m^2 *g^{-1}$) was 6.4 $m^2 *g^{-1}$ larger than the SSA of the high-C soil. However, the SSA of the fine silt-sized fractions of the low-C soil was 1 $m^2 *g^{-1}$ lower than that of the high-C soil (6.6 $m^2 *g^{-1}$). The SSA of the clay-sized fractions ranged between 35 and 47 $m^2 *g^{-1}$, and the SSA of fine silt-sized fractions are considerably lower, ranging between 5 and 10 $m^2 *g^{-1}$. The SSA for both clay and fine silt-sized fractions of both treatments of the low-C soil are significantly different ($P < 0.05$). For the high-C soil, significant differences ($P < 0.01$) in the SSA were found for the clay-sized fractions between both treatments, whereas no significant differences were found for the fine silt-sized fractions between treatments. The addition of glucose led to a decrease of the SSA compared to the control in the clay and fine silt-sized fractions of both soils. For the clay-sized fractions of the low-C soil, the SSA follows the order, $SSA_{Control} > SSA_{Glucose} > SSA_{A.A.}$. However, the amino acid substrate resulted in an increased SSA of the fine silt-sized fraction of the low-C soil and the clay-sized fraction of the high-C soil.

4. Discussion

4.1. Rapid MAOM formation after addition of low molecular weight OC

The freshly added LMWOC was recovered in both analyzed MAOM fractions, associated with fine silt and clay-sized minerals. Due to the very short timescale of the experiment, we assumed that the OM recovered as new MAOM-associated C was mainly due to the direct association of the added LMWOC with the mineral surfaces and to a lower extent by microbially transformed OM. If this assumption holds true, the amino acid derived OM $^{13}C/^{15}N$ ratios post-incubation would be close to the original amino acid $^{13}C/^{15}N$ value (2.91). We assumed clay minerals as the main mineral factor that determines MAOM formation due to the rather low contents of dithionite extractable Fe in the soils (9.8 mg$*g^{-1}$ for low-C soil and 14.2 mg$*g^{-1}$ for high-C soil, respectively, Table 1) (McKeague and Day, 1966).

However, we demonstrated that the substrate-derived $^{13}C/^{15}N$ ratio (between 3.28 and 6.29) (Table A2, in appendices) of the MAOM was higher than the $^{13}C/^{15}N$ ratio of the substrate itself (2.91), thus clearly pointing to the fact that after 24 h of substrate addition, part of the new MAOM is already microbially transformed. This assumption is supported by the results of a short-term glucose substrate experiment by Geyer et al. (2020), who found 30% of amended C was recovered as microbial residues in bulk soils after only six hours. Moreover, this assumed rapid microbial transformation is more pronounced in the soil with a high C loading. This is shown by $^{13}C/^{15}N$ ratios of the amino acid derived OM in the low-C soil (3.28) being lower (closer to the original amino acid $^{13}C/^{15}N$ value) than its counterpart in the high-C soil (4.16). Our finding is in accordance with other studies, that demonstrated such rapid microbial transformation. For instance, in an incubation experiment amending ^{14}C glucose and ^{15}N-NH_4 to a Vertisol and Alfisol Ladd et al. (1996) demonstrated that after three days of incubation the organic $^{14}C/^{15}N$ ratio was higher in the soil that contained more C. Poirier et al. (2013) also reported similar results for a 51-day incubation experiment by studying the effects of maize residue on the fate of the fresh OM in soils with differences in stored C (topsoil vs. subsoil). The authors demonstrated that the residue-derived C/N ratios were closer to the original residue's C/N ratio in the soil with lower C content compared to the soil with higher C content.

This supports our assumption that the retention of fresh OM as MAOM in the fine-sized fractions of soils with different C loadings is driven by different pathways, which can be due to the microbial activity. In addition, differences in the microbial community structure between the two soils might have fostered the reported differences in the fate of

the freshly added OM. The C-rich soils sustain a higher microbial activity, which also may lead to higher amounts of microbial-derived MAOM. This is in accordance with studies that used glucose addition to study the correlations between glucose-derived C and microbial biomass. For instance, Van Veen et al. (1985) found that native biomass C was highly correlated with glucose-derived biomass C after 44 and 66 weeks of glucose addition. In a four-week incubation experiment by Creamer et al. (2016), the authors demonstrated that the initial amount of soil microbial biomass was one of the main drivers for the formation of new SOC.

As the low-C soil and high-C soil have differences in their pH (6.4 and 7.6, respectively), we have to consider the potential role of soil pH on the retention of the amino acid derived OM. Decreasing soil pH promotes the adsorption of basic amino acids over acidic and neutral ones in the soil (Gao et al., 2018; Henrichs and Sugai, 1993; Vinolas et al., 2001), as negatively charged mineral surfaces enhance the sorption of positively charged molecules. However, we demonstrated that the amino acid derived OM was more efficiently retained in clay-sized fractions of the soil with lower pH than the soil with higher pH, whereas the amount of the amino acid derived OM retained on the fine silt-sized fraction of two soils did not show a significant difference. It can be assumed that soil pH is highly unlikely a dominant controlling factor for the retention of the added amino acids. Otherwise, the reduced amount of retained amino acid derived OM should have been demonstrated in both fine-sized fractions between the two soils. As stated above, we also assume that the added amino acid has been rapidly transformed by microorganisms and thus the retention of microbial-derived OM might be less affected by differences in soil pH. We thus demonstrate that even on very short timescales, the contribution of microbial transformed OM to the formation of MAOM should not be overlooked.

4.2. C loading impacts short-term fresh organic matter retention in fine-sized fractions

Our results indicated that the fine-sized mineral fractions (<6.3 μm) of the low-C soil are clearly depleted in SOC (Table 4, with a much lower C loading of 33% compared to the mean saturation level of Bavarian cropland soils of 50% (Wiesmeier et al., 2014b). In contrast to the low-C soil, the saturation level of the high-C soil of 75% is well above this average SOC saturation level reported by Wiesmeier et al. (2014b). This demonstrates the significant differences in cropland SOC storage dominated by MAOM, as regulated by long-term differences in C input. Based on the two soils in our study, it was shown that soils deficient in SOC are more efficient in retaining fresh OM compared to already well-saturated soils. This was indicated by the higher isotopic enrichment of the OM in the fine mineral fractions of the low-C soil, compared to those of the high-C soil (Fig. 2, A, B). Our findings on SOC saturation level and fresh OM retention potential are in agreement with Stewart et al. (2007), who showed that soils far below their specific SOC storage capacity show a greater efficiency in sequestering new C. The difference in the SOC loading of the low-C and high-C soil resulted in clear differences in the retention of freshly added OM, thus the initial soil C loading is decisive for the retention of newly added OM also in the short-term. Thus, as pointed out in the long-term perspective (Chenu et al., 2018; Lavallee et al., 2020), we can now demonstrate that the OC saturation level of the MAOM is also important for the overall SOC sequestration rate at an early stage.

We recovered around 50% of fresh OM in the bulk soil for all samples. These amounts of recovered freshly added OM are in the range of values (~60% for glucose and ~80% for amino acid in bulk soil) reported for other short-term experiments (24 h), in which glucose was amended to temperate forest soils (Typic Dystrudepts of the Gloucester series) (Geyer et al., 2020) and amino acids were added to forest soils (Jones and Kielland, 2002). The newly added OM that retained in the bulk soil but was not recovered as MAOM in the analyzed fine-sized mineral fractions were probably retained as MAOM in the fraction > 6.3 μm. Besides that, a considerable amount might also be still in the dissolved OM phase or be associated with particulate OM. The retention of fresh OM occurred primarily in the clay-sized fraction (up to 23% of the added OM) (Fig. 1, E, F), which illustrates the high importance of the fine mineral fractions (clay-sized minerals) for the sequestration of rather labile OM inputs in soils (Christensen and Sørensen, 1985; Kaiser and Zech, 2000). The retention of substrate-derived OM in the clay-sized fraction was substantially above the level recovered in the fine silt-sized fraction. This distinct difference can be suggested to be due to the differences in the specific surface area (SSA) of both fractions. The mineral surface area was previously shown to closely correlate with the amount of associated OM (Mayer, 1994a; Saggar et al., 1996; Sarkar et al., 2018) and the SSA decreases with the increasing particle size (Keil et al., 1994). The clay-sized fractions with greater SSA provide a larger number of reactive sites available for the sorption of OM, and therefore, retained more fresh OM than the fine silt-sized fractions. We assume that the freshly added LMWOC in the low-C soil is likely to bind with free mineral surfaces via organo-mineral interactions rather than with existing MAOM via organo-organo interactions (Possinger et al., 2020). This is supported by Gao et al. (2018), who demonstrated that minerals with dissolved organic matter coating suppressed the further adsorption of acidic amino acid. The higher C content of the MAOM can thus be the reason for the high-C soil being less efficient in retaining amino acid than the low-C soil. A higher soil C loading results in fewer possible interactions of free mineral surfaces with OM, with this type of interaction being considered as the main factor in the persistence of SOM (Lützow et al., 2006; Sollins et al., 1996).

4.3. Does N content of substrate determine short-term fresh OM retention in clay fractions?

In the low-C soil, the N-rich substrate led to twice as much retained freshly added LMWOM as the substrate without N, thereby indicating the importance of N content of freshly added OM for soil C sequestration. With the addition of glucose (N-free substrate), the high-C soil, which also contained more N, retained more substrate-derived OM than the low-C soil (Fig. 1, C, E). This suggests the initial soil N content might be a limiting factor in the sequestration of fresh OM inputs in the MAOM pool. The fact that a high N content enhanced fresh OM sequestration is in accordance with studies that tested the effects of the addition of N on the SOC stock. In a glucose tracing study with and without N addition using soils from a temperate forest, Wang et al. (2019) demonstrated a higher increase of SOC when glucose was added together with N. The positive effect of higher N availability on SOM formation was not only demonstrated using LMWOM but also with more complex natural plant litter. A positive relation was observed between the N content of added plant litter and C accumulation in the soil MAOM pool (Córdova et al., 2018). This is nicely corroborated by a *meta*-analysis spanning over 257 soils under various land uses, in which Lu et al. (2011) showed a significant increase of the soil C pool (3.5% for agricultural soils) due to N fertilization.

Depending on the soil C loading, the recovery of fresh OM differed considerably between the two LMW substrates (Fig. 1, C to F). We show that the N content of the substrate determines the retention of fresh OM in the low-C soil (Fig. 2, C), which leads to the assumption that, for degraded soils with low C saturation, the addition of OM with higher N contents supports the build-up of mineral-associated OM. However, the substrate with high N content (amino acids) did not enhance the recovery of fresh OM in the clay-sized MAOM fraction (Fig. 1, E). Although the high-C soil contains more clay-sized minerals, which was previously shown to be positively related to the retention of OM (Guillaume et al., 2022; Hassink, 1997), in the present study this did not lead to a higher retention of fresh LMWOC, which demonstrates a decoupling of the retention of fresh LMWOC in the form of MAOM in C saturated soils. In accordance with our results, Creamer et al. (2014) observed no

enhancement in glucose-derived SOC with N addition. The authors used an agricultural soil with very low clay content (1.7%) and thus a higher saturation level of OC in the MAOM pool. Based on our findings for the retention of fresh OM in a highly saturated soil, we assume that as soon as soils reach a C storage level that is close to the saturation level (Stewart et al., 2007), the N content of the input is no longer decisive for the build-up of new MAOM. Although studies reported the addition of N increased the C stock in the MAOM pool (Diekow et al., 2005), in soil microaggregates (Kirkby et al., 2014) and at the bulk soil scale (Hyvönen et al., 2008), we question this relationship between the substrate N content and the amount of stored freshly added OM at the scale of functional SOM pools. The importance of the N content of the organic substrate for the sequestration of freshly added OM can be assumed to be lower at higher N availability in native MAOM. Mineral-associated OM as an important microbial N source is also suggested by Guillaume et al. (2022). The authors demonstrated that cropland soils with lower MAOM C saturation level showed a stronger N depletion in their particulate OM than grassland soils. In our study, the N-rich substrate did not significantly impact the storage of fresh OM in the high-C soil, indicating the soil C loading; and thus the soil C saturation level, as an important regulator in retaining freshly added OM. We suggest that C retention in the MAOM pool of soils with high C contents is primarily controlled by the soil C saturation level rather than by the N content of the OM input. This is supported by a model study on agricultural and forest soil (Castellano et al., 2015), demonstrating that the N availability of litter input affected SOC storage based on the SOC saturation level.

On the other hand, the chemical structure of the added LMWOC can be assumed to foster the different retention of the added OM in the soil, as the functional groups of OM influence their adsorption (Henrichs and Sugai, 1993). Glucose adsorbs to soil minerals through the hydroxyl (R-OH) groups and the sorption of amino acid occurs mainly by amino (R-NH_2) or carboxyl (R-COOH) groups (Johnston and Tombacz, 2002; Thompson and Goyne, 2012) and thus, the sorption of amino acid depends on the soil pH. The negative charge of clay minerals does not change with pH. The lower pH indicates a possible higher positive charge on mineral surfaces, which would not benefit the cation absorption. A larger amount of basic amino acid absorbed in soil compared to neutral and acidic ones, which was reported at the soil pH at 6.9 (Jones and Hodge, 1999). This indicates that acidic amino acids would be stronger sorbed in the studied low-C soil. As acidic amino acid makes up 50% of the used amino acid mixture, this might have led to the lower amount of amino acid retained in the soil with higher pH. Beyond the properties of the fine-sized soil minerals, the composition of the MAOM might also directly affect the sorption of the amino acid (Gao et al., 2018). The authors demonstrated that the amount of absorbed amino acids varied on the mineral surface coated with O horizon-derived dissolved OM and leaf litter-derived dissolved OM. As due to the different management the studied fine-sized mineral fractions showed different C/N ratios, one can assume that this is also a driver for the demonstrated differences in the retention of fresh OM.

As the specific surface area of the mineral fractions is negatively related to the sorption of OM (Kaiser and Guggenberger, 2000), we expected a decrease in SSA with adding fresh LMWOC. We also expected the high-C soil to present a lower SSA than the low-C soil due to a higher surface coverage with SOM. Although the amino acid substrate was highly retained in the clay-sized fraction of the high-C soil, demonstrated by the isotopic enrichment of the OM (Fig. 2, A), we observed an increase of the clay SSA due to the LMWOC addition. This could potentially indicate a loss of native MAOC that could be accelerated due to increased N availability due to the addition of amino acids. This assumption is supported by Blagodatskaya et al. (2007), who found a higher native C lost under C-limiting conditions but not under N-limiting conditions. This points to a possible increased microbial consumption of native C fostered by the low C/N input material.

5. Conclusions

Our short-term incubation experiment indicated that the short-term recovery of freshly added low-molecular-weight organic compounds (LMWOC) in the MAOM pool is controlled by the soil C saturation level and the N content of the added substrate. The freshly added OM retained preferentially in the smaller MAOM fractions, especially in the clay-sized fractions, pointing to the importance of the specific mineral surface area for C sequestration. We demonstrate that N-rich substrate only has a positive effect on the retention of fresh OM as MAOM in soils with low C saturation level. Therefore, we state that the initial soil organic matter content (especially N content) affects the sequestration of fresh OM to a greater extent than the N content of the OM substrate.

Declaration of Competing Interest

The authors declare that they have no known competing financial interests or personal relationships that could have appeared to influence the work reported in this paper.

Acknowledgments

We would like to thank the technicians, Maria Greiner, Franziska Fella and Jürgen Kler for supporting the laboratory work at TUM and LfL. This work was supported by the Deutsche Forschungsgemeinschaft (DFG) (grant number HO 5121/1-1) and the National Research Fund Luxembourg (FNR) (grant number INTER/DFG/17/11779689).

Appendices

Mass distribution

Table A1
Mass distribution of particulate organic matter (POM) and each mineral fraction using density fractionation (density of 1.8 g/cm^3).

	POM (mg *g^{-1})	Mineral fraction (mg *g^{-1})		
		< 2 µm	**2 - 6.3 µm**	**> 6.3 µm**
Low-C soil	2 ± 1.5	184 ± 5.3	69 ± 3.7	745 ± 9.3
High-C soil	14 ± 9.1	281 ± 9.1	73 ± 2.6	632 ± 14.8

Mineralogy

Using X-ray diffraction (XRD) analysis, it was possible to demonstrate similar mineralogy of the clay and fine silt fractions for both soils (Fig. A1); thus showing a high level of comparability between the fine-sized mineral fractions. The XRD spectra of all clay and fine silt fractions show major peaks that indicate four minerals: illite, chlorite, kaolinite and quartz. The overlapped peak of kaolinite and chlorite is located between 14° to 15° 2θ and a mixed layer of clay minerals is found between 7° to 10° 2θ. The content of main clay mineral phases in both soils follows the order: illite > chlorite > kaolinite. For each size fraction the proportion of every mineral phase is similar in the two soils, whereas the proportion of mineral phases between silt and clay is slightly different.

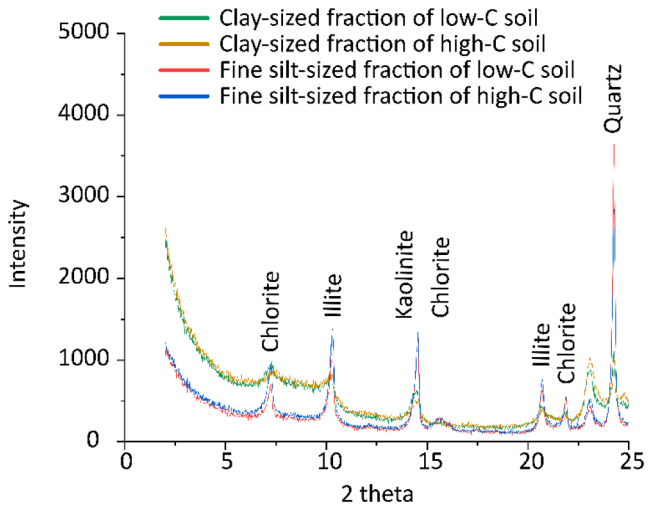

Fig. A1. XRD results of clay and fine silt-sized fractions of bare fellow (low-C) and direct seeding (high-C) soil.

Amino acid derived $^{13}C/^{15}N$ ratio

Table A2
The amino acid $^{13}C/^{15}N$ ratio and the amino acid derived $^{13}C/^{15}N$ ratio of clay-sized MAOM fractions of low-C and high-C soil after 24 hours incubation.

	Clay-sized fraction		Fine silt-sized fraction		Amino Acid
	Low-C Soil	**High-C Soil**	**Low-C Soil**	**High-C Soil**	
$^{13}C/^{15}N$ ratio	3.28 ± 0.01	4.16 ± 0.09	4.08 ± 0.21	6.29 ± 0.17	2.91

Amino acid mixture

Table A3
Relative composition of algal amino acid mixture.

Amino acid	Relative composition %	Amino acid	Relative composition %
ASP	40.6	**MET**	0.6
THR	3.9	**ILE**	1.3
SER	5.1	**LEU**	3.8
GLU	9.2	**TYR**	1.2
PRO	2.6	**PHE**	0.8
GLY	12.1	**HIS**	0
ALA	13	**LYS**	2.1
VAL	2.3	**TRP**	0

References

Basile-Doelsch, I., Balesdent, J., Pellerin, S., 2020. Reviews and syntheses: The mechanisms underlying carbon storage in soil. Biogeosciences 17 (21), 5223–5242.

Blagodatskaya, E.V., Blagodatsky, S.A., Anderson, T.H., Kuzyakov, Y., 2007. Priming effects in Chernozem induced by glucose and N in relation to microbial growth strategies. Appl. Soil Ecol. 37, 95–105.

Brown, K.H., Bach, E.M., Drijber, R.A., Hofmockel, K.S., Jeske, E.S., Sawyer, J.E., Castellano, M.J., 2014. A long-term nitrogen fertilizer gradient has little effect on soil organic matter in a high-intensity maize production system. Glob. Change Biol. 20, 1339–1350.

Buckeridge, K.M., La Rosa, A.F., Mason, K.E., Whitaker, J., McNamara, N.P., Grant, H.K., Ostle, N.J., 2020. Sticky dead microbes: Rapid abiotic retention of microbial necromass in soil. Soil Biology and Biochemistry.

Campbell, C.A., Lafosd, G.P., Zestser, R.P., Biederbeck, V., 1991. Influence of fertilizer and straw baling on soil organic matter in a thin black chernozem in western Canada. Soil Biol. Biochem. 23, 443–446.

Castellano, M.J., Mueller, K.E., Olk, D.C., Sawyer, J.E., Six, J., 2015. Integrating plant litter quality, soil organic matter stabilization, and the carbon saturation concept. Glob. Change Biol. 21, 3200–3209.

Chenu, C., Angers, D.A., Barré, P., Derrien, D., Arrouays, D., Balesdent, J., 2018. Increasing organic stocks in agricultural soils: Knowledge gaps and potential innovations. Soil Tillage Res. 188, 41–52.

Chiou, C.T., Rutherford, D.W., Manes, M., 1993. Sorption of nitrogen and ethylene glycol monoethyl ether (EGME) vapors on some soils, clays, and mineral oxides and determination of sample surface areas by use of sorption data. Environ. Sci. Technol. 27.

Christensen, B.T., 1992. Physical fractionation of soil and organic matter in primary particle size and density separates. Adv. Soil Sci. 1–90.

Christensen, B.T., 2001. Physical fractionation of soil and structural and functional complexity in organic matter turnover. Eur. J. Soil Sci. 52 (3), 345–353.

Christensen, B.T., Sørensen, L.H., 1985. The distribution of native and labelled carbon between soil particle size fractions isolated from long-term incubation experiments. J. Soil Sci. 36, 219–229.

Córdova, S.C., Olk, D.C., Dietzel, R.N., Mueller, K.E., Archontouilis, S.V., Castellano, M. J., 2018. Plant litter quality affects the accumulation rate, composition, and stability of mineral-associated soil organic matter. Soil Biol. Biochem. 125, 115–124.

Cotrufo, M.F., Wallenstein, M.D., Boot, C.M., Denef, K., Paul, E., 2013. The Microbial Efficiency-Matrix Stabilization (MEMS) framework integrates plant litter decomposition with soil organic matter stabilization: do labile plant inputs form stable soil organic matter? Glob. Change Biol. 19, 988–995.

Creamer, C.A., Jones, D.L., Baldock, J.A., Farrell, M., 2014. Stoichiometric controls upon low molecular weight carbon decomposition. Soil Biol. Biochem. 79, 50–56.

Creamer, C.A., Jones, D.L., Baldock, J.A., Rui, Y., Murphy, D.V., Hoyle, F.C., Farrell, M., 2016. Is the fate of glucose-derived carbon more strongly driven by nutrient availability, soil texture, or microbial biomass size? Soil Biol. Biochem. 103, 201–212.

Denef, K., Six, J., Merckx, R., Paustian, K., 2004. Carbon Sequestration in Microaggregates of No-Tillage Soilswith Different Clay Mineralogy. Soil Sci. Soc. Am. J. 68 (6), 1935–1944.

Diekow, J., Mielniczuk, J., Knicker, H., Bayer, C., Dick, D.P., Kögel-Knabner, I., 2005. Carbon and nitrogen stocks in physical fractions of a subtropical Acrisol as influenced by long-term no-till cropping systems and N fertilisation. Plant Soil 268, 319–328.

Dungait, J.A.J., Hopkins, D.W., Gregory, A.S., Whitmore, A.P., 2012. Soil organic matter turnover is governed by accessibility not recalcitrance. Glob. Change Biol. 18, 1781–1796.

Feller, C., Beare, M.H., 1997. Physical control of soil organic matter dynamics in the tropics. Geoderma 69–116.

Feng, W., Plante, A.F., Aufdenkampe, A.K., Six, J., 2014. Soil organic matter stability in organo-mineral complexes as a function of increasing C loading. Soil Biol. Biochem. 69, 398–405.

Fischer, H., Ingwersen, J., Kuzyakov, Y., 2010. Microbial uptake of low-molecular-weight organic substances out-competes sorption in soil. Eur. J. Soil Sci. 61, 504–513.

Gao, J., Jansen, B., Cerli, C., Helmus, R., Mikutta, R., Dultz, S., Guggenberger, G., Vogel, C., Kalbitz, K., 2018. Organic matter coatings of soil minerals affect adsorptive interactions with phenolic and amino acids. Eur. J. Soil Sci. 69, 613–624.

Gentile, R., Vanlauwe, B., Six, J., 2011. Litter quality impacts short-but not long-term soil carbon dynamics in soil aggregate fractions. Ecol. Appl. 21 (3), 695–703.

Geyer, K., Schnecker, J., Grandy, A.S., Richter, A., Frey, S., 2020. Assessing microbial residues in soil as a potential carbon sink and moderator of carbon use efficiency. Biogeochemistry.

Golchin, A., Oades, J.M., Skjemstad, J.O., Clarke, P., 1994. Soil Structure and Carbon Cycling. Soil Res. 1043–1068.

Grandy, A.S., Neff, J.C., 2008. Molecular C dynamics downstream: the biochemical decomposition sequence and its impact on soil organic matter structure and function. Sci. Total Environ. 404, 297–307.

Guillaume, T., Makowski, D., Libohova, Z., Bragazza, L., Sallaku, F., Sinaj, S., 2022. Soil organic carbon saturation in cropland-grassland systems: Storage potential and soil quality. Geoderma 406.

Hassink, J., 1997. The capacity of soils to preserve organic C and N by their association with clay and silt particles. Plant Soil.

Hassink, J., Bouwman, L., Zwart, K., Bloem, J., Brussaard, L., 1993. Relationships between soil texture, physical protection of organic matter, soil biota, and C and N mineralization in grassland soils. In: Soil Structure/Soil Biota Interrelationships. Elsevier, pp. 105–128.

Heister, K., 2014. The measurement of the specific surface area of soils by gas and polar liquid adsorption methods—Limitations and potentials. Geoderma 216, 75–87.

Henrichs, S.M., Sugai, S.F., 1993. Adsorption of amino acids and glucose by sediments of Resurrection Bay, Alaska, USA: functional group effects. Geochim. Cosmochim. Acta 57, 823–835.

Holmgren, G.G., 1967. A rapid citrate-dithionite extractable iron procedure. Soil Sci. Soc. Am. J. 31, 210–211.

Hyvönen, R., Persson, T., Andersson, S., Olsson, B., Ågren, G.I., Linder, S., 2008. Impact of long-term nitrogen addition on carbon stocks in trees and soils in northern Europe. Biogeochemistry 89, 121–137.

Jastrow, J.D., 1996. Soil aggregate formation and the accrual of particulate and mineral-associated organic matter. Soil Biol. Biochem. 28 (4-5), 665–676.

Jilling, A., Kane, D., Williams, A., Yannarell, A.C., Davis, A., Jordan, N.R., Koide, R.T., Mortensen, D.A., Smith, R.G., Snapp, S.S., Spokas, K.A., Stuart Grandy, A., 2020.

Rapid and distinct responses of particulate and mineral-associated organic nitrogen to conservation tillage and cover crops. Geoderma 359.
Johnston, C.T., Tombacz, E., 2002. Surface chemistry of soil minerals. Soil Mineral. Environ. Appl. 7, 37–67.
Jones, D., Hodge, A., 1999. Biodegradation kinetics and sorption reactions of three differently charged amino acids in soil and their effects on plant organic nitrogen availability. Soil Biol. Biochem. 31, 1331–1342.
Jones, D.L., Kielland, K., 2002. Soil amino acid turnover dominates the nitrogen flux in permafrost-dominated taiga forest soils. Soil Biol. Biochem. 34, 209–219.
Kaiser, K., Guggenberger, G., 2000. The role of DOM sorption to mineral surfaces in the preservation of organic matter in soils. Org Geochem. 31, 711–725.
Kaiser, K., Guggenberger, G., 2003. Mineral surfaces and soil organic matter. Eur. J. Soil Sci. 54 (2), 219–236.
Kaiser, K., Zech, W., 2000. Dissolved organic matter sorption by mineral constituents of subsoil clay fractions. J. Plant Nutr. Soil Sci. 163 (5), 531–535.
Keil, R.G., Tsamakis, E., Fuh, C.B., Giddings, J.C., Hedges, J.I., 1994. Mineralogical and textural controls on the organic composition of coastal marine sediments: Hydrodynamic separation using SPLITT-fractionation. Geochim. Cosmochim. Acta 58.
Keiluweit, M., Bougoure, J.J., Nico, P.S., Pett-Ridge, J., Weber, P.K., Kleber, M., 2015. Mineral protection of soil carbon counteracted by root exudates. Nat. Clim. Change 5, 588–595.
Kirchmann, H., Haberhauer, G., Kandeler, E., Sessitsch, A., Gerzabek, M.H., 2004. Effects of level and quality of organic matter input on carbon storage and biological activity in soil: Synthesis of a long-term experiment. Global Biogeochem. Cycles 18.
Kirkby, C.A., Richardson, A.E., Wade, L.J., Passioura, J.B., Batten, G.D., Blanchard, C., Kirkegaard, J.A., 2014. Nutrient availability limits carbon sequestration in arable soils. Soil Biol. Biochem. 68, 402–409.
Kleber, M., Eusterhues, K., Keiluweit, M., Mikutta, C., Mikutta, R., Nico, P.S., 2015. In: Mineral–Organic Associations: Formation, Properties, and Relevance in Soil Environments, pp. 1–140.
Kleber, M., Sollins, P., Sutton, R., 2007. A conceptual model of organo-mineral interactions in soils: self-assembly of organic molecular fragments into zonal structures on mineral surfaces. Biogeochemistry 85, 9–24.
Kögel-Knabner, I., Guggenberger, G., Kleber, M., Kandeler, E., Kalbitz, K., Scheu, S., Eusterhues, K., Leinweber, P., 2008. Organo-mineral associations in temperate soils: Integrating biology, mineralogy, and organic matter chemistry. J. Plant Nutr. Soil Sci. 171, 61–82.
Kopittke, P.M., Dalal, R.C., Hoeschen, C., Li, C., Menzies, N.W., Mueller, C.W., 2020. Soil organic matter is stabilized by organo-mineral associations through two key processes: The role of the carbon to nitrogen ratio. Geoderma 357.
Ladd, J., Van Gestel, M., Monrozier, L.J., Amato, M., 1996. Distribution of organic 14C and 15N in particle-size fractions of soils incubated with 14C, 15N-labelled glucose/NH4, and legume and wheat straw residues. Soil Biol. Biochem. 28, 893–905.
Lal, R., 2004. Soil Carbon Sequestration Impacts on Global Climate Change and Food Securit. Science 304 (5677), 1623–1627.
Lal, R., Negassa, W., Lorenz, K., 2015. Carbon sequestration in soil. Curr. Opin. Environ. Sustain. 15, 79–86.
Lavallee, J.M., Soong, J.L., Cotrufo, M.F., 2020. Conceptualizing soil organic matter into particulate and mineral-associated forms to address global change in the 21st century. Glob. Change Biol. 26 (1), 261–273.
Lehmann, J., Kleber, M., 2015. The contentious nature of soil organic matter. Nature 528, 60–68.
Leifeld, J., Zimmermann, M., Fuhrer, J., Conen, F., 2009. Storage and turnover of carbon in grassland soils along an elevation gradient in the Swiss Alps. Glob. Change Biol. 15, 668–679.
Liang, C., Amelung, W., Lehmann, J., Kastner, M., 2019. Quantitative assessment of microbial necromass contribution to soil organic matter. Glob Change Biol. 25, 3578–3590.
Lu, M., Zhou, X., Luo, Y., Yang, Y., Fang, C., Chen, J., Li, B., 2011. Minor stimulation of soil carbon storage by nitrogen addition: A meta-analysis. Agric. Ecosyst. Environ. 140, 234–244.
Lützow, M.V., Kögel-Knabner, I., Ekschmitt, K., Matzner, E., Guggenberger, G., Marschner, B., Flessa, H., 2006. Stabilization of organic matter in temperate soils: mechanisms and their relevance under different soil conditions - a review. Eur. J. Soil Sci. 57, 426–445.
Mayer, L.M., 1994a. Relationships between mineral surfaces and organic carbon concentrations in soils and sediments. Chem. Geol. 114 (3–4), 347–363.
Mayer, L.M., 1994b. Surface area control of organic carbon accumulation in continental shelf sediments. Geochim. Cosmochim. Acta 58.
McKeague, J., Day, J., 1966. Dithionite-and oxalate-extractable Fe and Al as aids in differentiating various classes of soils. Can. J. Soil Sci. 46, 13–22.
Miltner, A., Bombach, P., Schmidt-Brücken, B., Kästner, M., 2012. SOM genesis: microbial biomass as a significant source. Biogeochemistry 111, 41–55.
Moore, D.M., Reynolds Jr, R.C., 1989. X-ray Diffraction and the Identification and Analysis of Clay Minerals. Oxford University Press (OUP).
Niederbudde, E., 1973. Beziehungen zwischen K-Fixierungsvermögen und Dreischicht-Tonmineralen in Bodenprofilen auf Löß. Zeitschrift für Pflanzenernährung und Bodenkunde 135, 196–208.
Paul, E.A., 2016. The nature and dynamics of soil organic matter: Plant inputs, microbial transformations, and organic matter stabilization. Soil Biol. Biochem. 98, 109–126.
Poeplau, C., Don, A., Six, J., Kaiser, M., Benbi, D., Chenu, C., Cotrufo, M.F., Derrien, D., Gioacchini, P., Grand, S., Gregorich, E., Griepentrog, M., Gunina, A., Haddix, M., Kuzyakov, Y., Kühnel, A., Macdonald, L.M., Soong, J., Trigalet, S., Vermeire, M.-L., Rovira, P., van Wesemael, B., Wiesmeier, M., Yeasmin, S., Yevdokimov, I., Nieder, R., 2018. Isolating organic carbon fractions with varying turnover rates in temperate agricultural soils – A comprehensive method comparison. Soil Biol. Biochem. 125, 10–26.
Poirier, V., Angers, D.A., Rochette, P., Whalen, J.K., 2013. Initial soil organic carbon concentration influences the short-term retention of crop-residue carbon in the fine fraction of a heavy clay soil. Biol. Fertil. Soils 49, 527–535.
Possinger, A.R., Zachman, M.J., Enders, A., Levin, B.D.A., Muller, D.A., Kourkoutis, L.F., Lehmann, J., 2020. Organo-organic and organo-mineral interfaces in soil at the nanometer scale. Nat Commun 11, 6103.
Reicosky, D.C., Evans, S.D., Cambardella, C.A., Allmaras, R.R., Wilts, A.R., Huggins, D.R., 2002. Continuous corn with moldboard tillage: Residue and fertility effects on soil carbon. J. Soil Water Conserv. 57 (5), 277–284.
Saggar, S., Parshotam, A., Sparling, G.P., Feltham, C.W., Hart, P.B.S., 1996. 14C-labelled ryegrass turnover and residence times in soils varying in clay content and mineralogy. Soil Biol. Biochem. 12.
Saidy, A.R., Smernik, R.J., Baldock, J.A., Kaiser, K., Sanderman, J., 2013. The sorption of organic carbon onto differing clay minerals in the presence and absence of hydrous iron oxide. Geoderma 209–210, 15–21.
Sarkar, B., Singh, M., Mandal, S., Churchman, G.J., Bolan, N.S., 2018. Clay Minerals—Organic Matter Interactions in Relation to Carbon Stabilization in Soils. The Future of Soil Carbon 71–86.
Scharlemann, J.P.W., Tanner, E.V.J., Hiederer, R., Kapos, V., 2014. Global soil carbon: understanding and managing the largest terrestrial carbon pool. Carbon Manage. 5, 81–91.
Schlesinger, W.H. (2005) Biogeochemistry.
Six, J., Bossuyt, H., Degryze, S., Denef, K., 2004. A history of research on the link between (micro)aggregates, soil biota, and soil organic matter dynamics. Soil Tillage Res. 79, 7–31.
Six, J., Conant, R.T., Paul, E.A., Paustian, K., 2002. Stabilization mechanisms of soil organic matter: Implications for C saturation of soils. Plant Soil 241 (2), 155–176.
Sollins, P., Homann, P., Caldwell, B.A., 1996. Stabilization and destabilization of soil organic matter: mechanisms and controls. Geoderma 74.
Stanjek, H., Häusler, W., 2000. Quantifizierung silikatischer Tonminerale im Textur-und Pulverpräparat mit MACCLAYFIT. Berichte der Deutschen Ton-und Tonmineralgruppe eV 7, 256–265.
Stewart, C.E., Paustian, K., Conant, R.T., Plante, A.F., Six, J., 2007. Soil carbon saturation: concept, evidence and evaluation. Biogeochemistry 86, 19–31.
Stewart, C.E., Plante, A.F., Paustian, K., Conant, R.T., Six, J., 2008. Soil Carbon Saturation: Linking Concept and Measurable Carbon Pools. Soil Sci. Soc. Am. J. 72, 379–392.
Thompson, A., Goyne, K., 2012. Introduction to the sorption of chemical constituents in soils. Nature Education Knowledge 4, 7.
Torn, M., Kleber, M., Zavaleta, E., Zhu, B., Field, C., Trumbore, S.E., 2013. A dual isotope approach to isolate soil carbon pools of different turnover times. Biogeosciences 10, 8067–8081.
Van Veen, J., Ladd, J., Amato, M., 1985. Turnover of carbon and nitrogen through the microbial biomass in a sandy loam and a clay soil incubated with [14C (U)] glucose and [15N](NH4) 2SO4 under different moisture regimes. Soil Biol. Biochem. 17, 747–756.
Vinolas, L., Healey, J., Jones, D., 2001. Kinetics of soil microbial uptake of free amino acids. Biol. Fertil. Soils 33, 67–74.
von Lützow, M., Kögel-Knabner, I., Ekschmitt, K., Flessa, H., Guggenberger, G., Matzner, E., Marschner, B., 2007. SOM fractionation methods: Relevance to functional pools and to stabilization mechanisms. Soil Biol. Biochem. 39, 2183–2207.
Wang, K., Xing, B., 2005. Structural and sorption characteristics of adsorbed humic acid on clay minerals. J. Environ. Qual. 34, 342–349.
Wang, Q., Chen, L., Yang, Q., Sun, T., Li, C., 2019. Different effects of single versus repeated additions of glucose on the soil organic carbon turnover in a temperate forest receiving long-term N addition. Geoderma 341, 59–67.
Wiesmeier, M., Hübner, R., Dechow, R., Maier, H., Spörlein, P., Geuß, U., Hangen, E., Reischl, A., Schilling, B., von Lützow, M., Kögel-Knabner, I., 2014a. Estimation of past and recent carbon input by crops into agricultural soils of southeast Germany. Eur. J. Agron. 61, 10–23.
Wiesmeier, M., Hubner, R., Sporlein, P., Geuss, U., Hangen, E., Reischl, A., Schilling, B., von Lutzow, M., Kogel-Knabner, I., 2014b. Carbon sequestration potential of soils in southeast Germany derived from stable soil organic carbon saturation. Glob. Change Biol. 20, 653–665.
Wiesmeier, M., Urbanski, L., Hobley, E., Lang, B., von Lützow, M., Marin-Spiotta, E., van Wesemael, B., Rabot, E., Ließ, M., Garcia-Franco, N., Wollschläger, U., Vogel, H.-J., Kögel-Knabner, I., 2019. Soil organic carbon storage as a key function of soils - A review of drivers and indicators at various scales. Geoderma 333, 149–162.
Zhang, J., He, N., Liu, C., Xu, L., Chen, Z., Li, Y., Wang, R., Yu, G., Sun, W., Xiao, C., Chen, H.Y.H., Reich, P.B., 2019. Variation and evolution of C: N ratio among different organs enable plants to adapt to N-limited environments. Glob. Change Biol. 26 (4), 2534–2543.

Study 2

Wu, T., Wichern, F., Wiesmeier, M., Buegger, F., Shi, L., Dippold, M. A., Höschen, C., & Mueller, C. W.

Organic carbon loading of soils determines the fate of added fresh plant-derived organic matter

Geoderma 443 (2024) 116816

https://doi.org/10.1016/j.geoderma.2024.116816

Geoderma 443 (2024) 116816

Contents lists available at ScienceDirect

Geoderma

journal homepage: www.elsevier.com/locate/geoderma

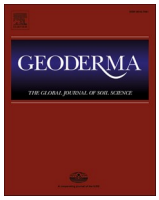

Organic carbon loading of soils determines the fate of added fresh plant-derived organic matter

Tianyi Wu [a,*], Florian Wichern [b], Martin Wiesmeier [a,c], Franz Buegger [d], Lingling Shi [e], Michaela A. Dippold [e,f], Carmen Höschen [a], Carsten W. Mueller [g,h]

[a] Soil Science, Research Department Life Science Systems, TUM School of Life Sciences, Technical University of Munich, 85354 Freising-Weihenstephan, Germany
[b] Soil Science and Plant Nutrition, Faculty of Life Sciences, Rhine-Waal University of Applied Sciences, Marie-Curie-Str. 1, 47533 Kleve, Germany
[c] Institute for Agroecology and Organic Farming, Bavarian State Research Center for Agriculture, 85354 Freising, Germany
[d] Research Unit Environmental Simulation, Helmholtz Zentrum München, German Research Center for Environmental Health, 85764 Neuherberg, Germany
[e] Geo-Biosphere Interactions, Department of Geosciences, University of Tuebingen, 72076 Tuebingen, Germany
[f] Biogeochemistry of Agroecosystems, Department of Crop Science, University of Goettingen, 37075 Goettingen, Germany
[g] Institute of Ecology, Chair of Soil Science, Technische Universität Berlin, 10587 Berlin, Germany
[h] Department of Geosciences and Natural Resource Management Geography, University of Copenhagen, 1350 Copenhagen, Denmark

ARTICLE INFO

Handling Editor: C. Rumpel

Keywords:
Soil respiration
Stable isotope tracing
Soil microorganisms
Plant litter nitrogen content
Priming effect, PLFA

ABSTRACT

It is crucial to promote soil carbon sequestration while reducing CO_2 emissions to mitigate climate change. However, the extent of increasing actual soil carbon storage depends on the amount and composition of organic matter input, including its fate during decomposition and soil organic matter (SOM) formation via microbial transformation. With respect to the need to increase carbon sequestration in soil and sustain soil fertility, it is of great interest to better understand how soils with different organic matter content react to amendment with fresh organic matter. Here, we incubated three agricultural soils representing a gradient in C content, adding two different ^{13}C labeled plant residues varying in carbon-to-nitrogen ratio. Carbon mineralization was monitored together with the analysis of the $^{13}CO_2$ signatures. After the incubation, ^{13}C compound-specific PLFAs, microbial necromass, and enzyme activities were analyzed. This study demonstrates that the carbon return on investment, thus the amount of retained fresh carbon in relation to the amount of added organic matter, clearly depends on the amount of native soil carbon. Notably, the addition of fresh organic matter to carbon-deficient soils leads to a higher specific CO_2 release compared to soils with high carbon loading, which can be attributed to the differences in the soil microorganisms' response. The CO_2 release of the soil with the lowest C-content was 2.1 and 2.0 mg g^{-1} soil for treatment with oat and pea litter addition, respectively, whereas for the soil with the highest C-content, CO_2 release was 1.7 mg g^{-1} soil for oat treatment and 1.6 mg g^{-1} soil for pea treatment. Thus, higher SOC contents sustain a higher 'return on investment' for the fresh carbon that is amended to soils. With plant litter amendments the microbial community shifted towards a higher fungi-to-bacteria ratio (F/B). This shift in the microbial community was more pronounced (F/B ranging from 0.04 to 0.11) with the addition of oat litter (low quality) compared to pea litter (high quality). Hence, it is important to consider the fate of organic amendments with different N availability when aiming to rebuild soil carbon stocks in degraded soils. Soil management should focus on sustaining soil carbon in balance with current carbon stocks to avoid the vicious circle of soils losing carbon in conjunction with increased greenhouse gas release.

1. Introduction

Soils are vital as the largest terrestrial carbon (C) pool in global C-cycling and storage (Post et al., 1982; Scharlemann et al., 2014). Moreover, with accelerating climate change, promoting sustainable C sequestration in soils is an essential tool to store atmospheric carbon dioxide (CO_2), maintain soil multi-functionalities such as in food and fiber production or biodiversity conservation, and adapt to climate change (Kopittke et al., 2022).

Agricultural land use has drastically reduced soil C stocks over

* Corresponding author.
E-mail address: tianyi.wu@tum.de (T. Wu).

https://doi.org/10.1016/j.geoderma.2024.116816
Received 1 April 2023; Received in revised form 17 January 2024; Accepted 12 February 2024
Available online 1 March 2024

millennia (Sanderman et al., 2017). Thus, agricultural soils are depleted in soil organic matter (SOM), particularly in areas with a long history of intensive cultivation (Don et al., 2011; Stewart et al., 2008). Furthermore, studies have shown that a soil organic C (SOC) content of 2 % is the critical minimum threshold for soil productivity (Stockmann et al., 2015; Zvomuya et al., 2008). It is assumed that soils have a specific capacity to store a certain amount of C, which has been suggested to be defined by the amount of fine-sized soil minerals (Hassink, 1997). Based on the concept of a distinct storage capacity of soil C, soils reach C saturation with increasing amounts of stored C (Hassink, 1997; Stewart et al., 2007), with limits defined by the amount of fine-sized minerals. Thus, soils maintaining low-C saturation levels, which we also refer to as soil C loading here, exhibit a greater potential to sequester additional amounts of C. Soil management has thus to focus on either increasing soils' SOC stock, if depleted, or maintaining SOC stocks in cases of soils at high-C saturation level. As plant residues represent the main C input to soils, the key to managing soil C stocks is to know how soils with different organic matter (OM) content and thus C saturation levels react to plant litter input. And it is crucial to better understand how soils tend to convert fresh plant-derived C into more persistent SOC forms based on their C loading, and thus contribute to long-lasting soil C storage.

The amount of SOC, which is stored either as particulate OM (POM) or as mineral-associated OM (MAOM), is the result of the decomposition of plant-derived OM, mainly fresh rather easily bioavailable POM, and the parallel formation of more persistent SOM forms (Angst et al., 2023). The activity and distribution of soil microorganisms control the fate of fresh OM and, consequently, the overall soil C flow, which regulates the ratio between C mineralization (soil respiration) and persistent SOM formation. This process is achieved by building up microbial biomass, and its subsequent entombing as microbial necromass C (Liang et al., 2017; Schimel and Schaeffer, 2012). Due to its pronounced association with MAOM, necromass C is one of the main components of rather persistent SOC (Angst et al., 2021; Hall et al., 2020). Although factors such as the quantity of plant litter input and its nitrogen (N) content have been studied extensively in their effect on C mineralization (Brown et al., 2014; Dungait et al., 2012; Mendoza et al., 2022; Nguyen et al., 2016), knowledge on how the C saturation of soil affects the fate of freshly added C remains scarce.

Fungi and bacteria, the major groups of soil microbiota, are the main drivers of soil C dynamics (Six et al., 2006). Microbial habitats, which vary in C saturation level, influence the soil microorganisms' life strategies by fostering certain densities of microorganisms that a specific soil environment can support (r- vs. K-strategy) (Andrews and Harris, 1986). Thus, the life strategy of microorganisms determines C mineralization, which is reflected in soil respiration. At stoichiometric imbalanced conditions, fungi and bacteria adjust the consumption of OM sources in relation to their demand for C and nutrients to meet their needs for energy and growth. Therefore, in addition to the amount of available soil C as an energy source, the amount of N and its availability determines soil C dynamics. The carbon-to-nitrogen ratio (C/N) of plant litter input thus directly affects soil C dynamic through its impact on the microbial community (Cotrufo et al., 2013; Gentile et al., 2011; Nguyen et al., 2016). It was shown that C availability limits especially bacterial growth, whereas N limitations stronger affect fungal growth (Rousk and Baath, 2007; Wang et al., 2014). Consequently, soils comprising different C saturation levels and the addition of plant litter with varying N content lead to significant differences in the mineralization of organic matter (Parkin et al., 1997; Wang et al., 2013). However, the mechanism by which soil C saturation and the N availability of the plant litter input influence the fate of soil C is not well elucidated.

To address the mentioned research gaps, we incubated three agricultural soils with clearly differing C saturation levels together with plant residues, either with narrow or wide C to N ratio and thus a different N availability. The work is based on the following hypotheses: 1) although gains in C storage is highest in soils with low C stocks, C return on investment is higher in soils with higher C saturation level and, thus, soils with higher C loading; and 2) plant litter rich in N promotes C retention in soils. The study's findings provide potential strategies to steer the use of plant OM amendments to keep or even increase soil C storage and thus sustain soil multi-functionality, including climate change mitigation. Furthermore, it is one important key to supporting future management strategies for sustaining or increasing SOM loading, especially in view of the recovery of C-depleted soils in agroecosystems.

2. Material and methods

2.1. Soil samples

To compare soil with different OM loadings, three agricultural soils, including bare fallow, three-field crop rotation, and direct seeding, were used in this study. These three soils with a SOC gradient were collected from a long-term field experiment in Puch (southern Germany, 48°11′37.0″N, 11°12′57.4″E), which is maintained by the Bavarian State Research Center for Agriculture (LfL). All experimental sites are located at an elevation of 550 m a.s.l. with a mean annual temperature of 8.8 °C and a mean annual precipitation of 872 mm. All three soils are characterized as Luvisols derived from loess deposits (IUSS Working Group WRB, 2015) and share the same soil mineralogy due to the same parent material and the close vicinity of the plots. There were no carbonates detectable in the soils from the same experimental plots as demonstrated in a the previous study (Wu et al., 2022).

Soil material used for the incubation experiment was sampled from the upper 10 cm of the Ap horizon at random locations within each plot (five spots per plot) and mixed thoroughly to form a composite sample. As the focus was on the mechanistic understanding of the actual fate of added plant OM on soil material differing in C loading, the composite samples represent the specific management plot. The fresh soil samples were air-dried at room temperature and sieved with a 2 mm mesh size. All visible plant residues were picked out by hand. Sub-samples were taken from each soil to determine basic soil properties (Table 1). Based on the SOC contents, we referred to the soil of bare fallow as low-C soil, three-field crop rotation as medium-C soil, and soil of the direct seeding fields as high-C soil in the following study. The initial SOC level of each soil is referred to as C loading.

The total C and N contents of bulk soils pre- and post-incubation combined with ^{13}C enrichment were measured using an isotope ratio mass spectrometer (IRMS, Delta V Advantage, Thermo Fisher, Dreieich, Germany) that was coupled to an elemental analyzer (EuroEA, Eurovector, Pavia, Italy). The enrichment value is given in atom-% (at%).

2.2. Plant residues used as organic input

Since C and N are intricately linked in the fate and turnover of SOM, we used two ^{13}C-labeled plant residues differing in C/N ratio (Table 2) to study the dynamic of OM. Oat and pea plants were chosen due to their difference in C/N ratio. Plants were grown in an arable soil in the greenhouse at Rhine-Waal University and ^{13}C-leaf labeled with multiple pulses over ten days using ^{13}C-glucose solution (2 % w/v) starting four weeks after planting. This labelling approach has been shown to efficiently label plants with ^{15}N (Kanders et al., 2017) with values being in the range of other approaches albeit like all labelling approaches having some shortcomings, which have been discussed elsewhere (e.g. Hupe et al. (2016), Wichern et al. (2008), Wichern et al. (2011), and Kanders et al. (2017)). To this end, one leaf was forced into a 2 ml vial containing the sterile solution. Upon complete uptake, an additional ^{13}C-glucose solution was added to the vial. After another two weeks, the labeled leaf was removed (not further considered in this experiment), and plant stems and leaves were harvested, air-dried, and finely ground to be used in this study. We ground and homogenized the plant material prior to the experiment so that similar material was applied to all soils in each treatment. Although the plants were not homogenously labelled, it likely not strongly affected the outcome of our experiment.

Table 1
Soil characteristics of bare fallow (low-C soil), three crop rotation (medium-C soil), and direct seeding (high-C soil). The particle size distribution was determined by texture analysis, as given by Wu et al. (2022). EC stands for electrical conductivity. The SOC storage capacity for those three soil was calculated according to Feng et al. (2013) and Wiesmeier et al. (2019).

Soil	Total C content (mg g^{-1})	Total N content (mg g^{-1})	C/N	pH	EC	Clay and fine silt content (mg g^{-1})	POM (mg g^{-1})	POM C/N	SOC storage capacity (mg g^{-1})	SOC saturation level (%)
Bare fallow (low-C soil)	6.4 ± 0.1	0.8 ± 0.0	8.4 ± 0.1	6.39	54.2	368	1.8	22.4	13.5	36.8
Three crop rotation (medium-C soil)	12.5 ± 0.0	1.4 ± 0.0	9.0 ± 0.2	6.86	60.8	450	4.7	14.9	16.1	59.6
Direct seeding (high-C soil)	20.7 ± 0.0	2.1 ± 0.0	9.9 ± 0.2	7.63	67.2	501	8.9	16.4	17.7	92

2.3. Organic matter addition and incubation experiment

The amount of added plant residue was based on common management practice and thus based on the added OC to soils via the regular amounts of plant residue input (Wiesmeier et al., 2014a). The ground plant residues (oat and pea litter) were added once at the start of the incubation, and thoroughly mixed with 50 g of the respective soils. The added OM accounted for amounts of 0 mg g^{-1} (control) and 10 mg g^{-1} (equivalent to 0 and 13 Mg OC ha^{-1}) based on amounts of normally added OC via harvest residues in the area. The experiment was conducted in a 3 × 3 full factorial design with three plant residues (control, oats, and peas) and three soils (low, medium, and high-C) with five replicates, totaling 45 samples.

Each sample was incubated in polyvinyl chloride (PVC) cylinder of 50 mm in height with a 45.2 mm inner diameter (Fig. A1). Furthermore, a mono-layer mesh (100 % polyester, mesh size 55 μm) was fixed at the bottom of the cylinder with a ring (O-ring, nitrile rubber) to allow ventilation and prevent stagnating water. The cylinder was placed in a 473 ml glass jar (gas-tight, Mason Glass, KoRo) with a lid on a small metal grid to allow better gas exchange at the bottom. One tube fitting (stainless steel, Swagelok) with a septum (Standard Septa, Wagner&munz) was installed on the lid for gas sampling.

Adding water to the dry soils was considered the starting time point of the incubation. Prior to our incubation, we tested soils at water holding capacities (WHC) between 40 % and 70 % with an increment of 10 % to investigate the optimal WHC, which ensure that the soil should not be dry on the surface after 48 h of incubation. The moisture content of each sample was controlled every 2 days, and if needed, water was added to sustain constant water availability. The test yielded a moisture content of 50 % WHC as optimal water availability to sustain microbial activity in all studied soils. Thus, water was added as a fine droplet to adjust the soil moisture to 50 % of the maximal water-holding capacity. Furthermore, the incubation was carried out for 90 days in a dark thermostatic room of 22 ℃ with the jars partly opened to avoid anaerobic conditions.

After 90 days, the incubation experiment was stopped and sampled. Each soil sample was well mixed in the cylinder to ensure a homogeneous soil sample for all further analysis. An aliquot of each sample was stored at 4 ℃ for PLFA and enzyme analysis (fresh samples). Approximately 1 and 10 g of fresh soil sub-samples were obtained from each setup for PLFA and enzyme analysis, respectively. The remaining soil material of each sample was immediately frozen using liquid nitrogen to stop any biological activity and subsequently freeze-dried to yield dry soil material.

2.4. Soil respiration measurements

Table 2
^{13}C enrichment, C and N content, and the C/N ratio of oat and pea powders.

Plant powder	C content (mg g^{-1})	^{13}C atom %	N content (mg g^{-1})	C/N
Oat (*Avena sativa* L.)	440	2.18	15.9	27.8
Pea (*Pisum sativum* L.)	432	1.69	40.2	10.7

We measured soil CO_2 production and $^{13}CO_2$ signatures at seven time points during the 90 days of incubation. Gas sampling was conducted after 24 h, 72 h, 7 days, 14 days, 30 days, 60 days, and 90 days of incubation. Therefore, gas samples were taken from the headspace in each jar using a 25 ml gas-tight syringe (Model 1025 TLL, Hamilton) and injected into an evacuated vial through a septum (Exetainer 12 ml, flat bottom, Labco, UK). Prior to each gas sampling, the syringe was rinsed 3 times with argon (Ar) to remove any contamination.

At the sampling time, the jars were sealed, and 70 ml Ar was injected to avoid negative pressure in the jars due to the gas sampling. The inert gas ensured that the composition of the air in the jar remained constant. We created a higher pressure inside the vial than the air pressure by injecting a 12.5 ml gas sample into the evacuated vial to exclude the environmental gas interference in the sample.

At each gas sampling occasion, each setup's first gas sample (t_0) was taken immediately after injecting the Ar. Then, after the jars were sealed for a certain time (t_1), the second ($t_0 + t_1$), third ($t_0 + 2\ t_1$), and fourth ($t_0 + 3\ t_1$) gas samples of each jar were taken. The sealing time t_1 ranged between 40 min and 180 min, depending on the sampling day and the treatments.

The gas samples' $^{13}CO_2$ abundance and CO_2 concentration were measured using a gas chromatography (GC)-IRMS system (Delta plus, Thermo Fisher, Dreieich, Germany). The system enables injecting up to 400 μl of sample gas by trapping CO_2 with liquid nitrogen from repeated injections. The ^{13}C enrichment of the gas samples is given in atom-% ^{13}C (at%).

Using a linear regression model (Eq. (1)) of the CO_2 concentration according to the CO_2 concentration difference from the time of the four sampling points, we calculated the respired CO_2. The outliers (if any) were removed. All trend lines had $R^2 > 0.98$.

$$CO_2(ppm) = k\left(\frac{ppm}{min}\right) \times t(min) + A(ppm) \quad (1)$$

The slope $k = \frac{\Delta CO_2}{\Delta t}$, i.e., the rate with which CO_2 concentration change represents the respiration rate. The variable t is the time since the jar was sealed. A stands for the environmental CO_2 concentration calculated from the linear regression.

The respiration rate of CO_2 in the jar was calculated as follows (Eq. (2)):

$$Respiration\ CO_2\left(mg\ min^{-1}\right) = k\left(\frac{ppm}{min}\right) \times VHeadspace(mL) \times \frac{M_{CO_2}\left(\frac{mg}{mmol}\right)}{M_V\left(\frac{mL}{mmol}\right)} \times \left(\frac{10^{-6}}{ppm}\right) \quad (2)$$

VHeadspace is the available volume of the jar. M_{CO_2} is the molar weight of CO_2, and M_V is the gas molar volume at 22 ℃

The CO_2-C respiration rate was calculated using Eq. (3):

$$Respiration\ CO_2\text{-}C\left(mg\ min^{-1}\right) = Respiration\ CO_2\left(mg\ min^{-1}\right) \times \frac{M_C\left(\frac{mg}{mmol}\right)}{M_{CO_2}\left(\frac{mg}{mmol}\right)} \quad (3)$$

M_C is the molecular weight of C.

We calculated the CO_2-C respiration rate per gram of soil:

$$R_{CO_2\text{-}C}\left(mg\ min^{-1}\ g^{-1}Soil\right) = \frac{Respiration\ CO_2\text{-}C\left(mg\ min^{-1}\right)}{soil\ mass(g)} \quad (4)$$

where the soil mass is the dry weight of the soil sample per microcosm.

The CO_2-C respiration rate was normalized to each gram of SOC per gram of soil:

$$Normalized\ R_{CO_2\text{-}C}\left(mg\ min^{-1}\ g^{-1}SOC\right) = \frac{Respiration\ CO_2\text{-}C\left(mg\ min^{-1}\ g^{-1}Soil\right)}{SOC(mg\ g^{-1}Soil)} \times \left(\frac{10^3 mg}{g}\right) \quad (5)$$

The share of plant litter-derived C (f_{plant}) in CO_2 was calculated as follows:

$$f_{plant} = \frac{^{13}C_{sample} - {}^{13}C_{soil}}{^{13}C_{plant} - {}^{13}C_{soil}} \quad (6)$$

where $^{13}C_{sample}$, $^{13}C_{soil}$, and $^{13}C_{plant}$ represent the content of ^{13}C in at% in the gas sample, soil, and plant litter, respectively.

The native SOM-derived CO_2-C is calculated using Eq. (7):

$$Native\ SOM-derived\ CO_2\text{-}C(mg\ g^{-1}soil) = \left(1 - f_{plant}\right) \times R_{CO_2-C} \quad (7)$$

The priming is calculated as follows:

$$Priming(\%) = \frac{Respiration\ CO_2\text{-}C(treatment) - Respiration\ CO_2\text{-}C(control)}{Respiration\ CO_2\text{-}C(control)} \times 100\% \quad (8)$$

As no carbonates were detected as demonstrated in a previous study using the same soils from the same research site (Wu et al., 2022), no carbonate-derived CO_2-C emission had to be taken into consideration.

2.5. Compound-specific phospholipid fatty acid analysis and enzyme assays

2.5.1. Phospholipid fatty acid analysis

Soil material from the incubated samples was analyzed for their PLFAs. PLFA extraction was adapted from Frostegård et al. (1991). According to the presence of PLFAs in different groups of microorganisms, we classified the Gram-negative (G−) bacteria (16:1ω7c, cy17:0, 18:1ω7c, cy19:0 PLFAs), Gram-positive (G+) bacteria (i15:0, a15:0, i16:0, i17:0 PLFAs), actinobacteria (Ac) (10Me16:0, 10Me17:0 and 10Me18:0 PLFAs), and fungi (18:2ω6,9 PLFAs) (Lewandowski et al., 2015; Sommer et al., 2017). The markers a14:0, 14:1w5c, 14:0, 15:0, 16:0, 17:0, 18:3w3,6,9, 18:0, and 20:0 were classified as non-specified PLFAs.

Briefly, 6 g of incubated fresh soil sample was placed in a 50 ml centrifuge tube. The internal standard 1 (25 μl, 1 μg μl^{-1}, 19:0 phospholipid) was added. A single-phase mixture of chloroform, methanol, and citric buffer (0.15 M, pH 4.0) (1:2:0.8 v/v/v) was used to extract the lipids. The solution was transferred to a silica column, to which we added chloroform, acetone, and methanol in sequence to elute the neutral-, glycol-, and phospholipids, respectively. The phospholipids were hydrolyzed by 1 M sodium hydroxide solution in methanol, followed by methylation with 0.3 M BF_3 solution in methanol. The final products were extracted in hexane and dried using an N_2 stream. This sample was re-dissolved in toluene with 15 μl of 13:0 fatty acid methyl ester (1 μg μl^{-1}). The specific compound PLFAs were measured using gas chromatography-mass spectrometry (GC–MS), equipped with 15-m HP-1 methylpolysiloxane coupled with a 30-m HP-5 (5 % phenyl)-methylpolysiloxane column. Both columns have an internal diameter of 0.25 mm and a film thickness of 0.25 μm. The He flow was 2 ml min^{-1}, and the injection volume was 1 μl. Measurement temperatures were set at 80 ℃, increased to 164 ℃ at 10 ℃ min^{-1}, followed by an increasing rate of 0.7 ℃ min^{-1} to 230 ℃ until it reached 300 ℃ at 10 ℃ min^{-1}. The quantity of PLFA was calculated based on a calibration curve of external standards, followed by correcting internal standards (Gunina et al., 2014).

The $^{13}C/^{12}C$ ratios of the PLFAs were determined using an IRMS

(Delta Plus TM, Thermo Finnigan, Germany) coupled with a GC (Trace GC 2000, Thermo Finnigan, Germany). The ^{13}C enrichment was corrected for the effect of the derivative C based on Glaser and Amelung (2002). Additionally, the share of plant-derived ^{13}C in the PLFA in analogy to gas samples was calculated using Eq. (6). The plant litter-C incorporation was calculated using Eq. (9):

$$\text{plant litter} - \text{C incorporation}(\%) = \frac{^{13}C \text{ abundance in PLFAs}}{^{13}\text{C input in the soil}} \times 100\% \quad (9)$$

A PLFA-based F/B ratio was calculated using the abundance of total fungal PLFAs and bacterial PLFAs.

2.5.2. Enzyme assays

Enzyme activities involved in C, N, and P cycles were measured based on fluorimetric microplate assays (Marx et al., 2005; Marx et al., 2001). Based on the fluorogenic substrates, including 4-methylumbelliferone (MUF) and 7-amino-4-methyl coumarin (AMC) (Sigma-Aldrich), we analyzed the activities of six enzymes: β-glucosidase (BG), β-xylosidase (BX), β-cellobiohydrolase (BC), chitinase, leucine-aminopeptidase, and acid phosphatase. The activities of C-cycling enzymes BG, BX, and BC were detected using 4-methylumbelliferone-b-D-glucoside, 4-methylumbelliferone-7-b-D-xyloside, and -methylumbelliferone-b-D-cellobioside, respectively. The N-cycle-related enzymes chitinase and leucine-aminopeptidase were determined using L-tyrosine-7-amido-4-methyl-coumarin (AMC-T) and L-leucine-7-amino-4-methyl coumarin (AMC-L). 4-Methylumbelliferyl-phosphate (MUF-P) was used to determine the P cycle's acid phosphatase activity.

Briefly, around 1 g of soil (equivalent dry weight) was dispersed in 50 ml of deionized water using low-energy ultrasonication (50 J s^{-1}, 120 s) to create a suspension. Aliquots of 50 μl suspension and 50 μl buffer (MES (pH:6.8) buffer for MUF substrate and TRIZMA (pH:7.2) buffer for AMC substrate) were assigned to 96-well microplates (black pure Grade® microplates, Brand GmbH, Wertheim, Germany). Subsequently, 100 μl of fluorogenic substrate solution was added at concentrations of 20, 40, 60, 80, 100, 200, and 400 mmol substrate g^{-1} soil. The fluorescence was measured after 0-, 60-, and 120-min assay incubation with a Victor 3 1420–050 Multi-Label Counter (Perkin Elmer, USA) at an excitation of 355 nm and an emission of 460 nm. The fluorescence was converted to the amount of MUF or AMC based on the standard solutions. The enzyme activities were reported as MUF or AMC release in nmol/h g^{-1} dry soil and calculated using the standard curve (German et al., 2011). The kinetic parameters V_{max}, maximum enzyme activity, and K_m, substrate concentration (S) at which the reaction rate equals $V_{max}/2$, were estimated using the non-linear regression model (Michaelis–Menten kinetics) (Marx et al., 2001):

$$V = (V_{max} \times S)/(K_m + S)$$

The enzyme activity ratios can be used to examine the relative allocation to energy versus nutrient acquisition (Stone et al., 2014). Total activities of C-cycling enzymes (TAC), N-cycling enzymes (TAN), and P-cycling enzymes (TAP) were used to calculate the relative C- vs. P-acquiring enzyme activities (TAC/(TAC + TAP)) and the relative C- vs. N-acquiring enzyme activities (TAC/(TAC + TAN)) (Sinsabaugh et al., 2008).

2.6. Microbial necromass

To assess the amount of microbial necromass we analyzed the content of four amino sugars, namely, glucosamine (GlcN), mannosamine, galactosamine, and muramic acid (MurA). The extraction procedure was adapted from Liang et al. (2012).

Briefly, around 400 mg of incubated freeze-dried soil sample was weighed into a hydrolysis glass (Duran, Schott) and mixed with 10 ml of 6 M hydrochloric acid (HCl). Samples were hydrolyzed at 105 ℃ for 8 h and then cooled to room temperature. Subsequently, 50 μl of 0.5 mg ml^{-1} Myo-inositol (Sigma-Aldrich) was added to each flask as an internal standard. The solution was filtered and collected in a pointed flask. A rotary evaporator (Heidolph) was used to reduce the liquid volume. The dried residue was suspended with 3 ml of deionized water.

Additionally, the pH value was adjusted to 6.6–6.8 using 1 M potassium hydroxide (KOH) solution for ion precipitation. The precipitates were separated by centrifugation at 3500 rpm for 20 min at 7 ℃. Then, the supernatant was transferred to a glass tube and dried under a nitrogen stream. Each sample received 300 μl derivation reagent containing 32 mg ml^{-1} hydroxylamine hydrochloride and 40 mg ml^{-1} 4-dimethylamino-pyridine in pyridine-methanol (4:1 v/v). The samples were vortexed thoroughly and heated at 78 ℃ for 35 min in a water bath. Overall, 1 ml acetic anhydride was given to each reaction vial after cooling to room temperature. The samples were re-vortexed thoroughly and heated at 78 ℃ in the water bath for 25 min. When the samples cooled to room temperature, 2 ml dichloromethane (DCM) was added to each sample. Overall, 1 ml of 1 M HCl was added to each sample and vortexed thoroughly to wash the samples. The samples were left to sit undisturbed to separate the two phrases. Then, the upper phase was discarded. Furthermore, the samples were washed three times with H_2O and dried under a gentle nitrogen stream. For the measurement, the residue was dissolved in 300 μl ethyl acetate/n-hexane (1:1 v/v) and transferred to GC vials with a small insert.

The measurement was carried out on a TRACE 1310 Gas Chromatograph (Thermo Scientific™), equipped with a fused silica column (ZB-5HT Inferno, L 60 m, ID 0.25 mm, FT 0.25 μm, Phenomenex Inc, USA). Helium was the carrier gas with a constant flow of 1 ml min^{-1}. The injection volume was 1 μl. First, the temperature was set at 120 ℃, held for 4 min, then ramped to 250 ℃ at 30 ℃ min^{-1} for 10 min, and finally to 280 ℃ at 5 ℃ min^{-1} for 10 min.

The microbial necromass C content was estimated based on the biomarker muramic acid and glucosamine, representing the maximum C content in the microbial necromass pool. The bacterial and fungal necromass C was calculated using Eq. (10) and Eq. (11), respectively, according to Appuhn and Joergensen (2006).

$$Bacterial\ necromass\ C\left(mg\ g^{-1}soil\right) = MurA(mg\ g^{-1}soil) \times 45 \quad (10)$$

$$Fungal\ necromass\ C\left(mg\ g^{-1}soil\right) = (mol\ GlcN - 2 \times mol\ MurA) \times molar\ weight\ GlcN \times 9 \quad (11)$$

The contribution of fungal or bacterial necromass C to SOC was calculated using the following:

$$Microbial\ necromass\ C\ contribution(\%) = \frac{Microbial\ necromass\ C}{Total\ SOC} \times 100\%$$

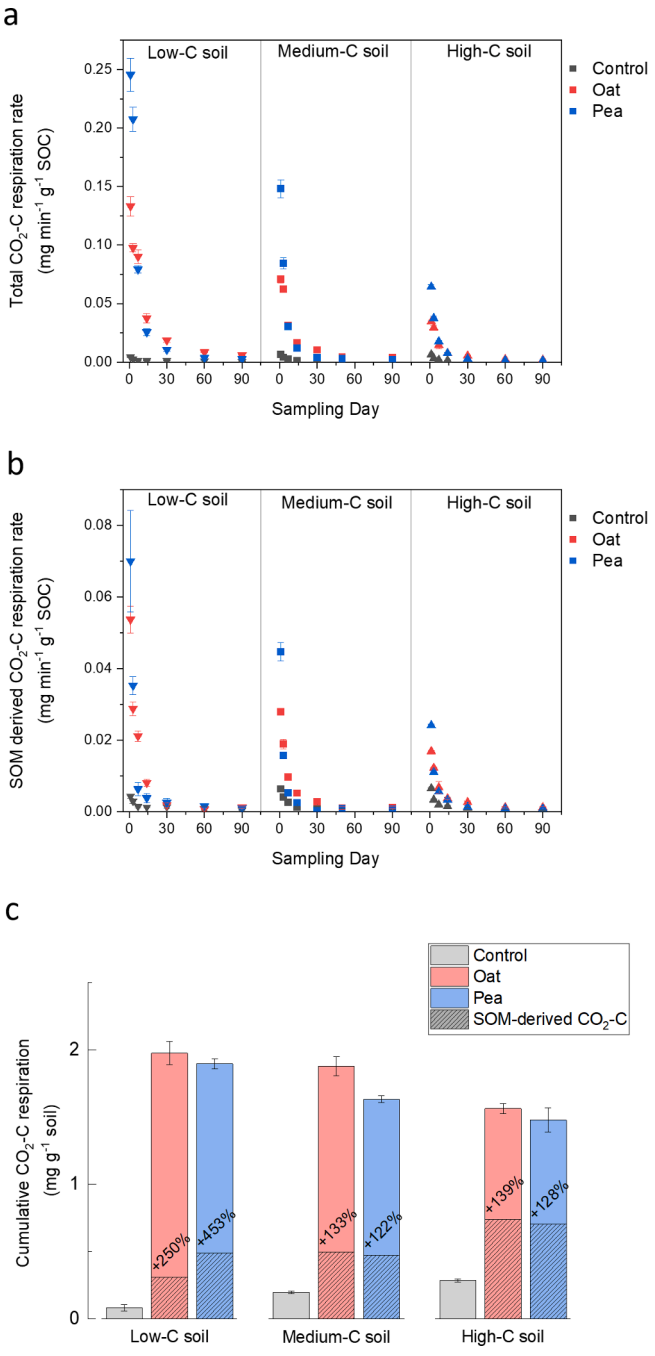

Fig. 1. a) Total CO_2-C respiration rate of low-, medium-, and high-C soil of oat and pea treatments. b) Total CO_2-C respiration rate of low-, medium-, and high-C soil of the control. c) Cumulative CO_2-C respiration of low-, medium-, and high-C soil. The numbers above the shade bars represent the priming effect. The gray, red, and blue dots and bars represent control, oat, and pea treatment, respectively. The shade bars stand for the native SOM-derived CO_2-C. Standard deviations are displayed with error bars.

2.7. Statistical analysis

Statistical analysis was carried out in Origin 2019 (OriginLab) for the datasets. First, the normality of the variance of the parameters was tested for normality using the Shapiro – Wilk test. Then, the data that passed the parametrical test were analyzed using a one-way analysis of variance (ANOVA) with Tukey's honestly significant difference test as the post hoc test. When the normality test failed, a log transformation was applied to the raw data, and the normality was tested again. Finally, for the non-normally distributed data, Kruskal – Wallis ANOVA was applied with Dunn's test as the post hoc test.

3. Results

3.1. Soil respiration

Soil CO_2-C respiration rates (Fig. 1) followed the OM loading (high-C soil > medium-C soil > low-C soil) in the control samples (without plant litter addition). However, this pattern was reversed due to the addition of plant litter. Adding pea litter led to higher soil respiration rates at the beginning of the incubation compared to adding oat litter. The total respired CO_2-C for the control samples was 0.09 ± 0.03, 0.21 ± 0.01, and 0.31 ± 0.01 mg g^{-1} for the low-, medium- and high-C soils, respectively. However, after plant litter addition, these values were 2.12 ± 0.10, 2.03 ± 0.07, and 1.69 ± 0.04 mg g^{-1} soil for oat litter addition, and 2.03 ± 0.05, 1.76 ± 0.03, and 1.60 ± 0.10 mg g^{-1} soil for soils with pea litter.

The litter addition stimulated mineralization (priming) of native SOM-derived C in all three soils, with the magnitude of soil priming varying according to the initial soil C loading. Oat litter addition in the low-C soil increased native SOM mineralization by 3.6-fold compared to control soils, whereas pea litter addition increased it by 5.7-fold. Soil priming was relatively lower in the medium-C soil, where increases were 2.3- and 2.2-fold, and in the high-C soil, with 2.4- and 2.3-fold increases, for oat and pea litter addition, respectively. The proportion of CO_2-C respiration derived from native SOM was 1 %–9 % higher in the pea litter treatment than in the oat litter treatment.

Considering respired to added plant-derived C, a higher proportion of added plant litter was mineralized in soils with lower C loading. For oat litter, 38 %, 32 %, and 20 % was respired in low-C, medium-C, and high-C soil, respectively. These numbers were 33 %, 28 %, and 19 % for pea litter. The total C recovery of added C over all samples was 101 ± 3 %.

3.2. Total organic carbon budget

Plant litter addition led to an increased SOC content after 90 days of incubation in all three soils (Fig. 2), which was relatively similar among all soils. However, compared to the present native SOC, the relative increase in SOC was negatively related. Thus, the low-, medium-, and high-C soil showed an increase in SOC content of 33 %, 15 %, and 9 % after 90 days of incubation with oat litter addition and 33 %, 14 %, and 8 % with pea litter addition, respectively.

3.3. Phospholipid fatty acids (PLFAs)

Compared to the control soils, plant litter addition resulted in a higher fungi-to-bacteria (F/B) ratio in all three soils. However, the shift of the F/B ratio (Fig. 3) was negatively related to the initial soil C loading. The change in the F/B ratio compared to the controls followed the order low-C soil > medium-C soil > high-C soil. Furthermore, oat litter addition significantly increased the F/B ratio (0.04–0.11) compared with pea litter addition, where the F/B ratio increased to 0.12 for the low-C soil, 0.11 for the medium-C soil, and 0.04 for the high-C soil.

The incorporation of oat and pea plant litter-C into different microbial groups associated with the three soils revealed different microbial consumption patterns (Fig. 4). The pea litter amendment led to higher total incorporation in microbial PLFAs than oat litter in all three soils.

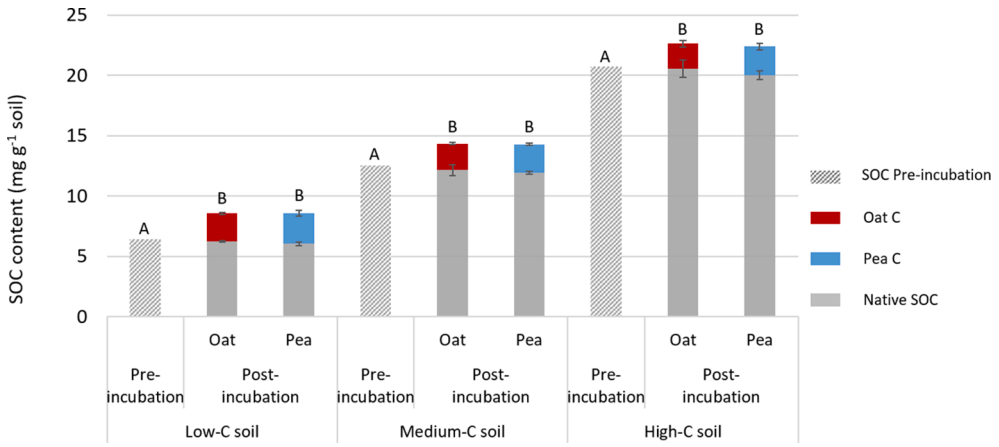

Fig. 2. Total carbon content in low-, medium-, and high-C soils pre- and post-incubation. Standard deviations are displayed with error bars. For a given soil, the capital letters represent significant differences between treatments.

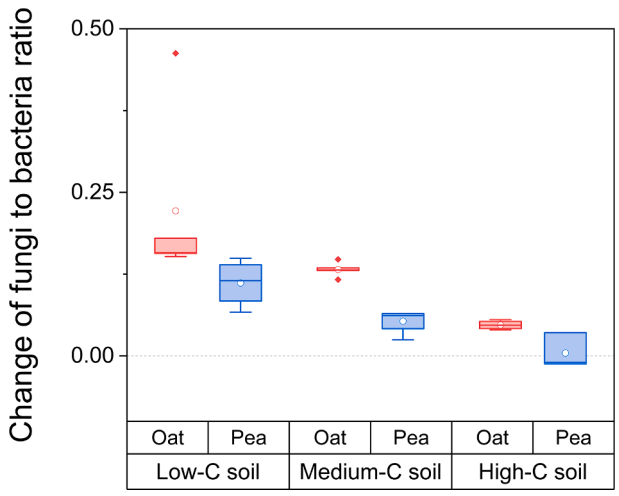

Fig. 3. Change in fungi-to-bacteria ratio (F/B) of oat treatment and pea treatment of low-, medium-, and high-C soil, calculated based on PLFA biomarker contents. The box plot represents the first quartile, the median, the mean, the outliers, and the third quartile range of the data. The change in the fungi-to-bacteria ratio was calculated by subtracting the F/B of the control from the F/B of the treatment.

This trend was more pronounced in the low- (1.2 %) and medium-C soils (1.4 %) than in the high-C soil (0.8 %). Overall, total oat-derived C incorporation in PLFAs was significantly higher ($p < 0.05$) in the high- and medium-C soils than in the low-C soil, with the high-C soil further higher than the medium-C soil. For incorporation of pea-derived C into microbial biomass, no significant differences were detected between the three soils; however, slightly lower incorporation of pea-derived C into PLFAs was shown in low-C soils. Most plant litter-C was incorporated into bacteria (actinobacteria, and G+ and G− biomarkers), varying from 51 % to 66 % of incorporated litter-C, which demonstrated that bacteria are the dominant microbial group incorporating fresh plant-derived C. This incorporation of plant C into bacterial PLFA was more pronounced with pea addition compared to oat addition.

In contrast, oat litter addition resulted in higher plant litter-C incorporation in saprotrophic fungi than in soils with pea amendment. Saprotrophic fungi contributed less than 22 % of the plant-C incorporation in PLFAs. The plant litter-C incorporated in the other PLFAs was between 18 % and 29 %.

3.4. Microbial necromass

Fig. 5a presents the microbial necromass calculated based on the amino sugar content. The microbial residue C in control soils significantly differed among the low-, medium-, and high-C soils, with 5.33 ± 2.47, 8.98 ± 2.57, and 10.54 ± 3.61 mg g^{-1} soil, respectively, thus following the soil C loading. The addition of oat litter increased the microbial residue C content by 2.77 ± 0.32, 1.43 ± 2.64, and 4.95 ± 3.94 mg g^{-1} for the low-, medium-, and high-C soils, respectively. Pea amendment slightly increased microbial residue C content in the low- (1.87 ± 0.19 mg g^{-1} soil) and medium-C soils (+0.77 ± 0.17 mg g^{-1} soil) but reduced microbial residue C content in the high-C soil (1.02 ± 1.31 mg g^{-1} soil). The content of bacterial necromass C showed significant differences between oat and pea treatments for all three soils. However, the fungal necromass C content significantly differed between oat and pea treatments in the low- and high-C soils but not in the medium-C soil. Microbial necromass C contributed more than 80 % of the SOC in the low-C soil, a lower value of about 70 % in the medium-C soil, and approximately 50 % in the high-C soil (Fig. 5b). Fungal C residues were more dominant than bacterial ones. Therefore, fungal residues contributed substantially more to the overall SOC pool. The fungal C residues also contributed more than 60 % to SOC in all soils, particularly in soils with oat litter addition, whereas bacterial residues contributed less than 8 %. Conversely, pea addition increased the contribution of bacterial residue C to SOC compared with the unamended control soils, which ranged from 10 % to 15 %; however, the contribution was still on a lower level than that of fungal residue C.

3.5. Enzyme vectors

Fig. 6 shows the enzyme activities translated into vectors for soils under either C or nutrient limitations (here N and P). The distance between the data points and the coordinate origin shows the strength of the relative C limitation. Interestingly the high-C soil presented a higher relative C limitation than the medium-C and low-C soils. The data points in the left upper area of the diagonal line show the P > N limitation, whereas those in the right lower part are under the N > P limitation. The control samples demonstrated that the low-C soil is more N and P-limited than the other two soils. Additionally, plant litter addition shifted the enzyme vectors toward the diagonal line and/or the

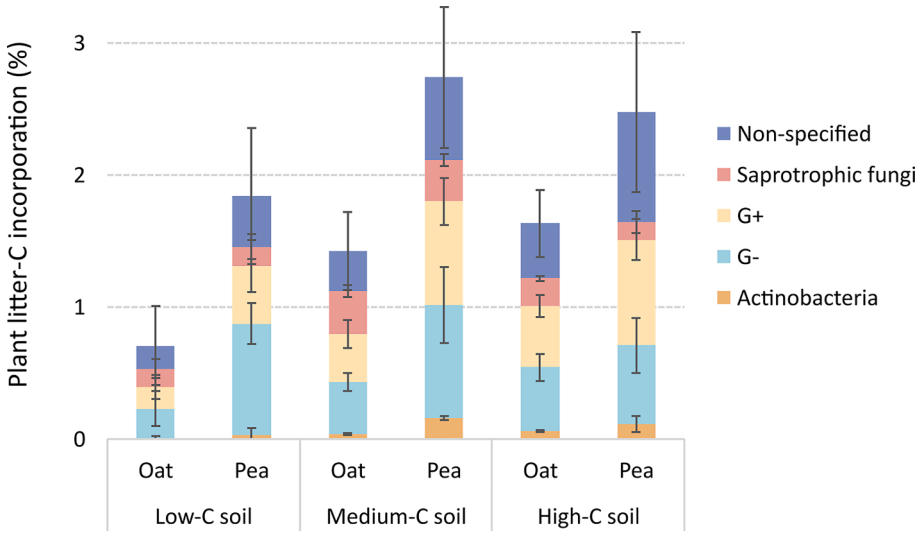

Fig. 4. Plant litter-C incorporated in the microbial group actinobacteria, Gram-negative bacteria (G−), Gram-positive bacteria (G+), saprotrophic fungi, and non-specified PLFAs. Standard deviations are displayed with error bars.

coordinate origin, indicating the alleviation of the C and/or N and P limitation in all soils. The pea treatment alleviated relative limitations more than the oat treatment.

4. Discussion

4.1. C saturation level determines OC dynamic

Besides soil properties, including mineralogy and texture, soil management, and thus organic matter input, are the main determinants of the total amount of OC sequestered in agricultural soils. For soils with comparable texture, the soil C loading, which results from the soil "management legacy", is shown to be the primary regulator of the sequestration of plant litter. In the present study, the overall C storage capacity of the three soils is comparable (Table 1), and thus, management with different OC inputs determines soil C storage and retention. At the average C saturation level of around 50 % in arable soils of South East Germany (Wiesmeier et al., 2014b), the three soils studied here nicely represent the low-, medium-, and high-C saturation level. In the absence of inputs of fresh plant-derived OM (the control soils), the magnitude of soil respiration directly mirrors the soil C content (as shown in Fig. 1b); the higher the SOC content, the higher the released CO_2 from heterotrophic respiration. Generally, increasing fresh OM input results in a corresponding increase in CO_2 release (Don et al., 2013; Mendoza et al., 2022; Rui et al., 2016; Wang et al., 2013). In this 90 days incubation study, we are able to demonstrate that soil C loading, which reflects the management legacy, directly affects this relationship (Fig. 1). Soils with very low-C loading show a higher CO_2 release after adding plant litter than well-managed OC-rich soils.

By studying soils varying in their C loading due to specific long-term soil management practices, we also demonstrated that the intricate connection of the fate of added fresh plant litter and native OM is closely related to the specific soil C loading. It was expected that the soil with the lowest C loading and therefore, the assumed greatest C retention potential (Stewart et al., 2007) would accommodate the highest C retention from plant litter. However, although low-C soils can gain considerable C, we demonstrated that a higher proportion of the plant litter was mineralized in the soil with the lowest initial C loading after 90 days of incubation. The highest total CO_2 release (Fig. 1) pointed to a rather vulnerable native SOM in the C-depleted soil, with a 3.6- and 5.7-fold increase in CO_2 release from native SOC. This increased release of native OC was due to enhanced microbial priming from the freshly added oat and pea litter. This points to the fact that besides the amount of freshly added C, the actual soil C storage and its legacy determine the C sequestration potential of a soil. Increasing the C input to soils with low-C loading may initially lead to less efficient C retention. However, increasing C storage over time by continuous C addition increases the efficiency of the retention of added C (Fig. 2). In general a positive feedback of C retention was demonstrated as a result of litter OM addition on the overall C storage.

Irrespective of the initial C loading and C mineralization, all studied soils retained C in response to the addition of easily bioavailable plant-derived OM (Fig. 2). Due to the lower natural C content the overall gain in added C in soils with lower C loading was high. Nonetheless, the mineralization rates of freshly added C in soils with low C stocks was also high (Fig. 1). The relative C sequestration potential, which implies the gain of added C to native C, remains greater in soils with lower C saturation levels (Fig. 2) (Mendoza et al., 2022; Stewart et al., 2008; Wu et al., 2022).

4.2. Microbial activities determine the OC dynamic

Soil C loading can influence the microbial growth strategy with microorganisms of either fast or slow growth rate (Chen et al., 2014; Fontaine et al., 2004). We assume that it is more likely that microorganisms with a fast growth rate (r-strategists) are fostered in soils with low-C availability. However, in soils with higher C saturation levels, microorganisms with slow growth rates (k-strategists) may thrive since higher amounts of SOC foster stronger niche separation (Fig. 4). The assumed link of higher C mineralization rates to higher growth rates is also supported by previous studies (Buckeridge et al., 2020b; Zheng et al., 2019). Moreover, the different nutrient availability of oat vs. pea litter regulated the microbial activity and thus, the overall consumption of added plant litter. The relative C limitation of the microbial activity was more marked in soils with higher C loading, whereas the relative nutrient limitation was more obvious in soils depleted in C (Fig. 6). Low-C loading drives microorganisms to mine higher amounts of plant litter for nutrients (Fontaine et al., 2004) to meet their stoichiometric

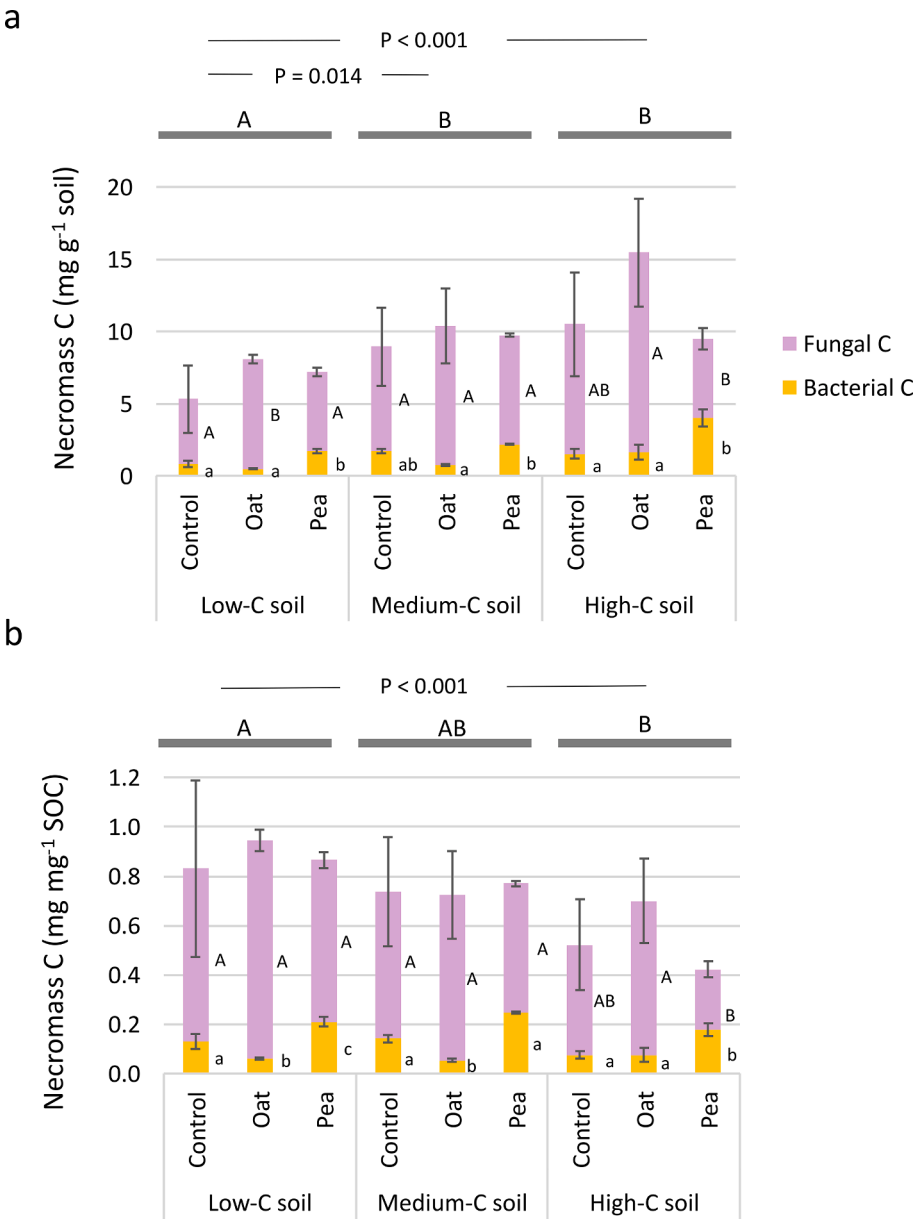

Fig. 5. a) Microbial residue c content in low-, medium-, and high-c soils of control, oat, and pea treatments as calculated from the amino sugar content (eq. (10) and Eq. (11)). b) Contribution of fungal C and bacterial C to SOC in control, oat, and pea treatments of low-, medium-, and high-C soils. The capital letters above the bars indicate significant differences in total necromass C of each soil. Standard deviations are displayed with error bars. For a given soil, the capital and lowercase letters represent significant differences between fungal and bacterial Cs of the treatments in each soil, respectively.

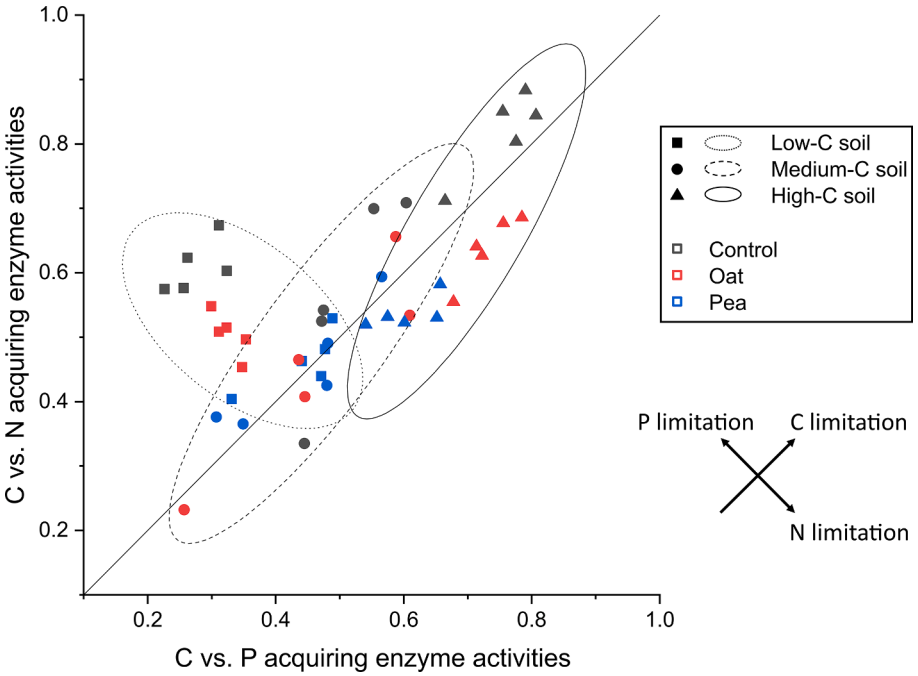

Fig. 6. C- vs. N- and C- vs. P-acquiring enzyme activities in low-, medium-, and high-C soils for control, oat, and pea treatments. The ellipses are confidence ellipses of low-, medium-, and high-C soils. The diagonal line demonstrated the C, N and P balanced condition.

demand. As shown by the enzyme activity (Fig. 6), N and P are major constraints to microorganisms in soils with lower C loading, and the availability of C majorly constrains microorganisms in soils with high C loading. Plant litter addition accelerates fungal growth in C-deficient soils, whereas bacterial growth is fostered in soils with sufficiently high C loading. This result agrees with previous findings, which show that nutrient availability limits fungal and C limits bacterial growth (Rousk and Baath, 2007; Wang et al., 2014). Plant litter amendment with higher N content (here, pea litter) created more balanced conditions with weaker stoichiometry constraints, thus reducing the need for microorganisms to mine for nutrients. This trend resulted in lower consumption of plant litter-derived OM, which contributes more to C retention after 90 days. However, considering the C availability from both native and freshly added OM, the bioavailability of OM for microorganisms using either one of the two pools also depends strongly on the spatial OM distribution (Kravchenko et al., 2019; Lehmann et al., 2020; Steffens et al., 2017). In soils with low C loading, more microorganisms and available native soil C might be spatially disconnected; however, proximity to available native soil C may foster priming in the high-C soil (Fig. 1). This result shows that a prerequisite of priming might be the spatial accessibility of the native OM, which is higher in the higher C-content soils.

4.3. Necromass in OC dynamic

In this study, the contribution of microbial necromass C to SOC decreased with the increasing C saturation level of the studied soils (Fig. 5). This indicated a higher retention of unprocessed freshly added plant litter, probably as POM, in soils with higher C loading. It was previously demonstrated that higher soil C saturation levels go along with increasing amounts of POM in the soil (Cotrufo et al., 2019), and presumably lower contribution of microbial necromass and MAOM.

Microbial consumption of plant-derived OM and the buildup of microbial biomass, and ultimately microbial necromass, lead to distinct ratios between microbial residues and plant-derived OM between the soils. Thus, differences in the amount of OM input and microbial decomposition are marked in the ratio between POM and microbial necromass. In this study, organic matter-depleted soils (low-C soil) with longer management of very low to neglectable OM inputs showed a very high contribution of microbial necromass to the overall soil C storage (Fig. 5b) (Liang et al., 2019; Wang et al., 2021). In contrast, soils with a continuously high plant OM input demonstrate a lower contribution of microbial necromass to the overall soil C storage, especially due to higher loads of mainly plant-derived POM. This lower contribution of microbial residues to overall C storage is also demonstrated by the increasing amount of the C/N from low-C soils to higher C loading soils, which is rich in less degraded plant-derived POM (Khan et al., 2016) (Table 1).

It can be assumed that microbial necromass and especially fungal residues, if associated with mineral surfaces as MAOM, is comparably more persistent than rather labile plant-derived OM (Cotrufo et al., 2019; Hannula and Morriën, 2022; Wang et al., 2021). The lowest specific respiration rates of respired CO_2-C per unit SOC in the control soils demonstrated this persistence (Fig. 1), with a dominant contribution of microbial necromass to the overall soil C (Fig. 5). The addition of plant litter particularly facilitated an increase in fungal biomass (Fig. 3) after 90 days, with more distinct increases in the F/B ratio in the soils with lower C loading. This effect is especially pronounced with the addition of plant residues low in N, which in this study was the oat material with rather wide C/N ratios. We demonstrated that fungal necromass particularly increases owing to plant litter addition. Therefore, this might lead to the dominance of fungal OM, which is stored as more persistent OM due to the chemical composition of the fungal necromass itself (Buckeridge et al., 2022; Sylvia et al., 2005) and has lower bioavailability due to organo-mineral associations (Hannula and Morriën, 2022). Overall, fungi made better use of low N litter (oat),

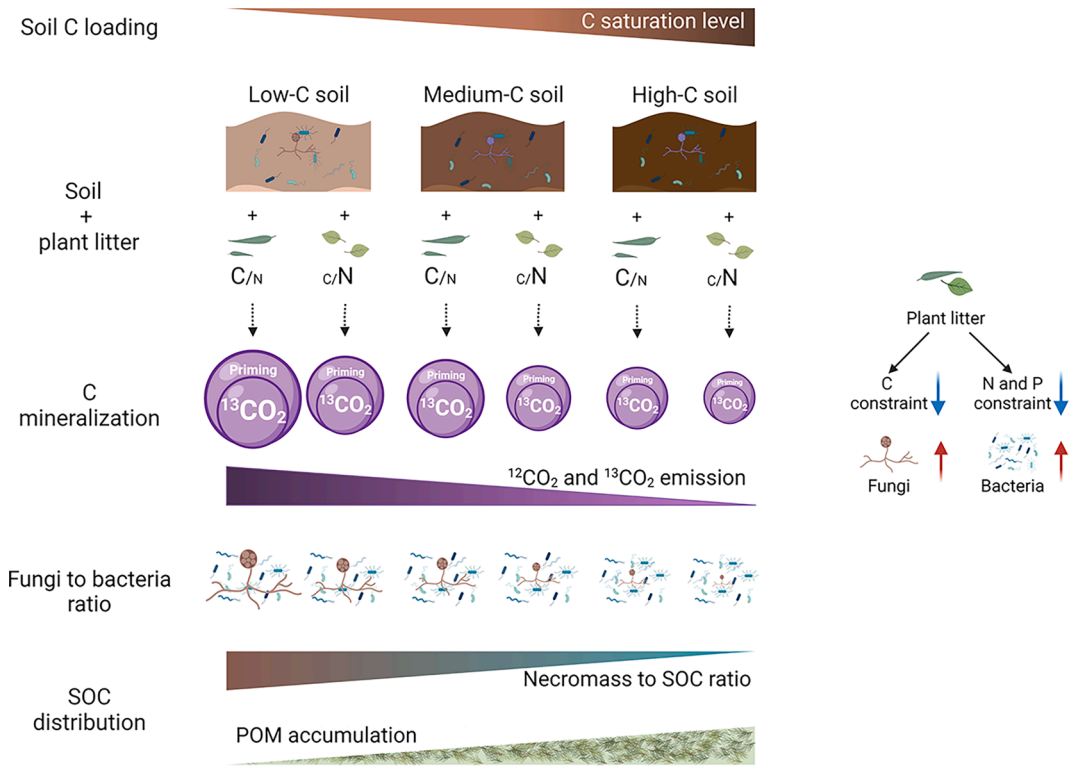

Fig. 7. C dynamics of soils with different C saturation levels.

whereas bacteria increased with high N litter addition (pea), as demonstrated by Rousk and Baath (2007) in a previous study. The different respiration rates may have indicated the differences in C use efficiency between fungi and bacteria, which can be assumed to be due to the lower efficiency of fungi in using C compared to bacteria (Anderson and Domsch, 1975; Rousk and Frey, 2015; Soares and Rousk, 2019).

However, microbial residues themselves are likely not a C sink that is persistent on a rather long timescale since both fungi and bacteria can and do consume microbial necromass to gain energy (Beidler et al., 2020; Buckeridge et al., 2020a). Consequently, microbial necromass could be considered as a rather active SOM pool used as a C and nutrient source by soil microorganisms. We demonstrate that adding plant-derived OM low in N leads to marked consumption of bacterial-derived necromass by fungi (Fig. 5). Therefore, the quantity of microbial necromass is determined by the N content of the active SOM pool, including microbial residues and plant litter input that regulates microbial activity through C and nutrient availability in the soil (Fig. 5).

4.4. Implications for soil organic carbon storage

It is essential to foster soil management strategies that ensure high soil POM contents fed by sustained plant OM input as a precursor for forming more persistent OM forms, i.e., MAOM (van Wesemael et al., 2019). This process will help avoid the vicious circle of soil losing C concomitantly with increased greenhouse gas release.

In soils with high soil C saturation levels, freshly added OM is retained in an efficient loop of microbial activity that uses both fresh and native OM while reducing overall CO_2 emissions. In soils with deficient C loading, microorganisms use the added fresh OM more inefficiently, which increases the use of native C due to priming for nutrients acquisition by the microorganisms. To enhance the "return on investment" for C addition to deficient soils, the C/N ratio of the added OM plays a major role. By adding OM with a lower N availability to C-depleted soils, the early-stage SOC retention is stimulated by an increased fungal activity, which reveals a lower C use efficiency. The C storage legacy of soil directly regulates the functioning and composition of the microbial communities that regulate the fate of freshly added OM and thus, the overall trajectory of soil C retention.

Bacteria benefit more from adding plant residues with higher N availability, which results in higher C use efficiency and reduced CO_2 emissions. Although the fresh OM input is less efficiently retained in soils lower in C (C-depleted soils), there is an increasing potential (self-enhancing positive feedback) of soils to retain SOC derived from added fresh litter over time with increasing C loading. This trend indicates that management has to focus on sustaining soil C levels to avoid rebuilding soil C stocks while suppressing further CO_2 emissions in the future. This knowledge offers some potential for ensuring the multi-functionality of soils especially facing drastic climate change and the need for mitigation. Thus, while currently well-managed medium- to high-C soils may act as C sinks, applying plant residues with higher N content to low-C soils may assist in converting those soils into valuable future C sinks more efficiently. The locally often limited amounts of available plant residues to be used as soil amendments can thus be used more efficiently for C retention. This approach might help ensure that correctly managed agricultural soils contribute to long-term terrestrial C storage.

5. Conclusion

In the present study we focused on the fate of freshly added plant

derived OC as regulated by different microbial consumption in soils with different soil carbon loading. Plant litter amendment to the soils changed the microbial community composition with a shift towards higher F/B ratios. This shift was more pronounced when adding lower-quality plant litter and in soils with low OM loading, indicating that fungi are especially limited by C availability in soils with low C loading. The addition of high-quality plant litter reduced C and nutrient limitations and thus allowed bacteria to thrive, which was more pronounced in high soils with high C loading. Further, plant litter amendments accelerated the C mineralization and fostered positive priming of inherited SOC in all three soils. However, the higher-quality plant litter amendment demonstrated less C mineralization than the lower-quality plant litter, with more material retained in the soils. Soils with higher OM-loading, regardless of the already high SOC saturation level, retained in total more freshly added OM even though priming of SOC was higher. Therefore, to obtain a better 'return on investment' of stored SOC in relation to added fresh C from OM amendments, soil management should consider sustaining soil carbon storage via balancing the input of fresh C with the current soil carbon loading.

CRediT authorship contribution statement

Tianyi Wu: Data curation, Formal analysis, Investigation, Methodology, Resources, Software, Visualization, Writing – original draft. **Florian Wichern:** Conceptualization, Supervision, Writing – original draft, Writing – review & editing. **Martin Wiesmeier:** Methodology, Resources, Validation, Writing – review & editing. **Franz Buegger:** Data curation, Formal analysis, Methodology, Writing – review & editing. **Lingling Shi:** Methodology, Software, Writing – review & editing. **Michaela A. Dippold:** Conceptualization, Methodology, Supervision, Writing – review & editing. **Carmen Höschen:** Funding acquisition, Project administration, Resources, Supervision, Writing – review & editing. **Carsten W. Mueller:** Conceptualization, Funding acquisition, Project administration, Resources, Supervision, Visualization, Writing – review & editing.

Declaration of competing interest

The authors declare that they have no known competing financial interests or personal relationships that could have appeared to influence the work reported in this paper.

Data availability

Data will be made available on request.

Acknowledgements

This work was supported by Deutsche Forschungsgemeinschaft (DFG) grant number HO 5121/1-1. We thank all technicians of the chair of soil science at TUM for supporting the laboratory work, and Xiaona Song and Jie Zhou at the University of Göttingen for helping with soil enzyme activity analysis. Fig. 7 is created with BioRender.com.

Appendix

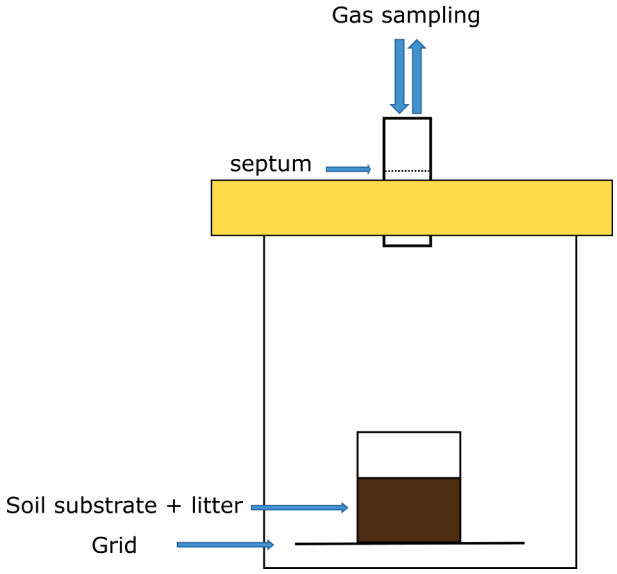

Fig. A1. Experimental setup.

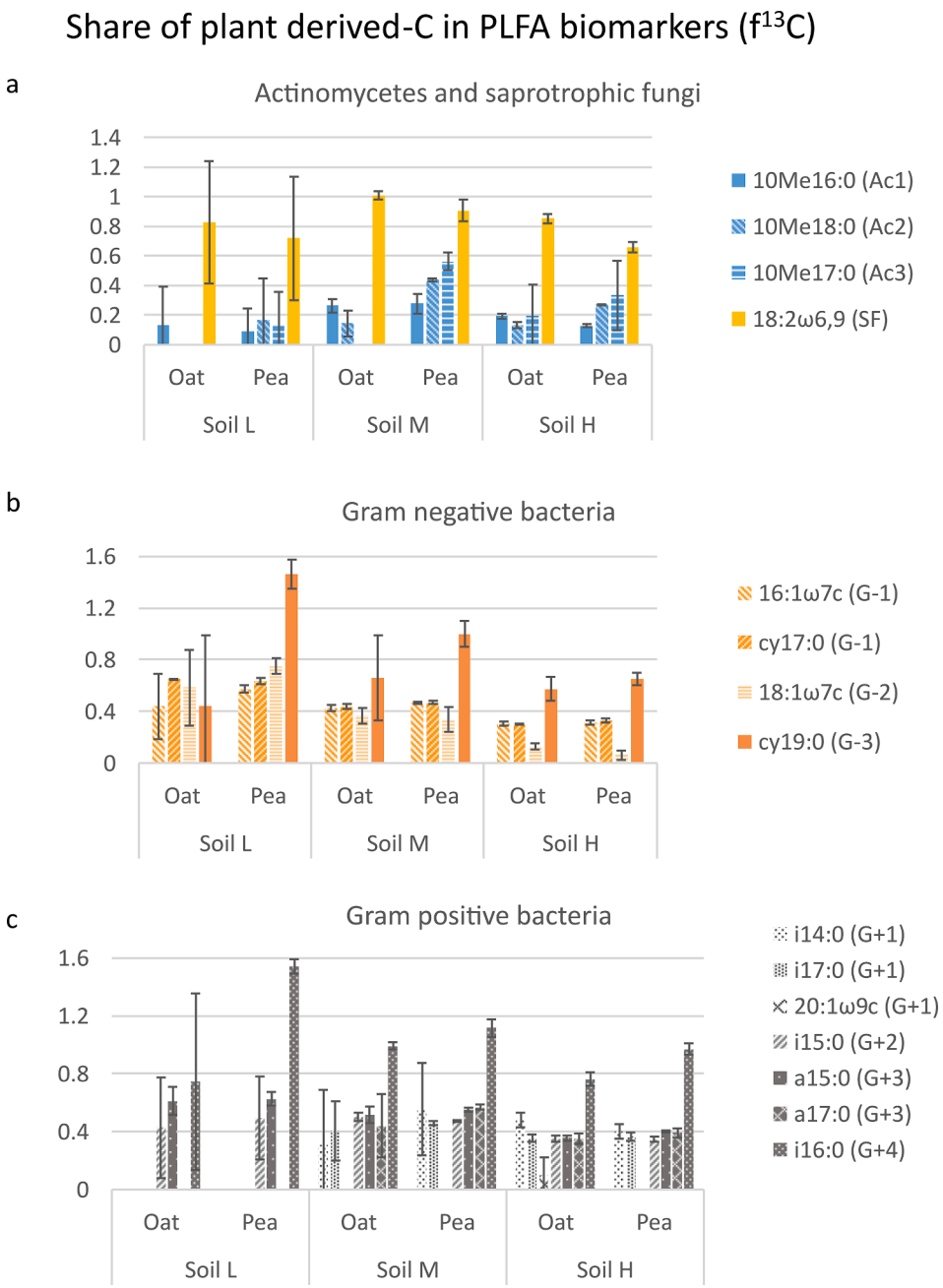

Fig. A2. Share of plant-derived C ($f^{13}C$) in actinobacteria, saprotrophic fungi, Gram-negative bacteria (G–), and Gram-positive bacteria (G+) of oat and pea treatments of low-, medium-, and high-C soils.

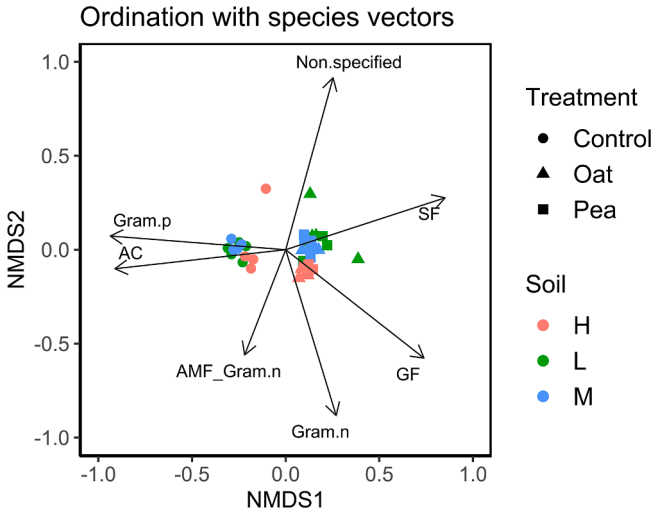

Fig. A3. Non-metric multidimensional scaling (NMDS) of the low- (L), medium- (M), and high-C (H) soils under control, oat, and pea treatments, ordinated with species vectors of actinobacteria (AC), marker 16:1ω5c (AMF), saprotrophic fungi (SF), Gram-negative or fungi (GF, marker 18:1ω9c), Gram-negative bacteria (Gram. n), Gram-positive bacteria (Gram.p), and non-specified (Non.specfied) markers is shown for all treatments.

References

Anderson, J., Domsch, K., 1975. Measurement of bacterial and fungal contributions to respiration of selected agricultural and forest soils. Can. J. Microbiol. 21 (3), 314–322.

Andrews, J.H., Harris, R.F., 1986. r-and K-selection and microbial ecology. Adv. Microb. Ecol. 99–147.

Angst, G., Mueller, K.E., Nierop, K.G., Simpson, M.J., 2021. Plant-or microbial-derived? a review on the molecular composition of stabilized soil organic matter. Soil Biol. Biochem. 156, 108189.

Angst, G., Mueller, K.E., Castellano, M.J., Vogel, C., Wiesmeier, M., Mueller, C.W., 2023. Unlocking complex soil systems as carbon sinks: multi-pool management as the key. Nat Commun 14 (1), 2967.

Appuhn, A., Joergensen, R., 2006. Microbial colonisation of roots as a function of plant species. Soil Biol. Biochem. 38 (5), 1040–1051.

Beidler, K.V., Phillips, R.P., Andrews, E., Maillard, F., Mushinski, R.M., Kennedy, P.G., Bardgett, R., 2020. Substrate quality drives fungal necromass decay and decomposer community structure under contrasting vegetation types. J. Ecol. 108 (5), 1845–1859.

Brown, K.H., Bach, E.M., Drijber, R.A., Hofmockel, K.S., Jeske, E.S., Sawyer, J.E., Castellano, M.J., 2014. A long-term nitrogen fertilizer gradient has little effect on soil organic matter in a high-intensity maize production system. Glob. Chang. Biol. 20 (4), 1339–1350.

Buckeridge, K.M., Mason, K.E., McNamara, N.P., Ostle, N., Puissant, J., Goodall, T., Griffiths, R.I., Stott, A.W., Whitaker, J., 2020a. Environmental and microbial controls on microbial necromass recycling, an important precursor for soil carbon stabilization. Commun. Earth Environ. 1 (1).

Buckeridge, K.M., Mason, K.E., McNamara, N.P., Ostle, N., Puissant, J., Goodall, T., Griffiths, R.I., Stott, A.W., Whitaker, J., 2020b. Environmental and microbial controls on microbial necromass recycling, an important precursor for soil carbon stabilization. Commun. Earth Environ. 1 (1), 36.

Buckeridge, K.M., Creamer, C., Whitaker, J., 2022. Deconstructing the microbial necromass continuum to inform soil carbon sequestration. Funct. Ecol.

Chen, R., Senbayram, M., Blagodatsky, S., Myachina, O., Dittert, K., Lin, X., Blagodatskaya, E., Kuzyakov, Y., 2014. Soil C and N availability determine the priming effect: microbial N mining and stoichiometric decomposition theories. Glob. Chang. Biol. 20 (7), 2356–2367.

Cotrufo, M.F., Wallenstein, M.D., Boot, C.M., Denef, K., Paul, E., 2013. The microbial efficiency-matrix stabilization (MEMS) framework integrates plant litter decomposition with soil organic matter stabilization: do labile plant inputs form stable soil organic matter? Glob. Chang. Biol. 19 (4), 988–995.

Cotrufo, M.F., Ranalli, M.G., Haddix, M.L., Six, J., Lugato, E., 2019. Soil carbon storage informed by particulate and mineral-associated organic matter. Nat. Geosci. 12 (12), 989–994.

Don, A., Schumacher, J., Freibauer, A., 2011. Impact of tropical land-use change on soil organic carbon stocks - a meta-analysis. Glob. Chang. Biol. 17 (4), 1658–1670.

Don, A., Rödenbeck, C., Gleixner, G., 2013. Unexpected control of soil carbon turnover by soil carbon concentration. Environ. Chem. Lett. 11 (4), 407–413.

Dungait, J.A.J., Hopkins, D.W., Gregory, A.S., Whitmore, A.P., 2012. Soil organic matter turnover is governed by accessibility not recalcitrance. Glob. Chang. Biol. 18 (6), 1781–1796.

Feng, W., Plante, A.F., Six, J., 2013. Improving estimates of maximal organic carbon stabilization by fine soil particles. Biogeochemistry 112, 81–93.

Fontaine, S., Bardoux, G., Abbadie, L., Mariotti, A., 2004. Carbon input to soil may decrease soil carbon content. Ecol. Lett. 7 (4), 314–320.

Frostegård, Å., Tunlid, A., Bååth, E., 1991. Microbial biomass measured as total lipid phosphate in soils of different organic content. J. Microbiol. Methods 14 (3), 151–163.

Gentile, R., Vanlauwe, B., Six, J., 2011. Litter quality impacts short-but not long-term soil carbon dynamics in soil aggregate fractions. Ecol. Appl. 21 (3), 695–703.

German, D.P., Weintraub, M.N., Grandy, A.S., Lauber, C.L., Rinkes, Z.L., Allison, S.D., 2011. Optimization of hydrolytic and oxidative enzyme methods for ecosystem studies. Soil Biol. Biochem. 43 (7), 1387–1397.

Glaser, B., Amelung, W., 2002. Determination of (13)C natural abundance of amino acid enantiomers in soil: methodological considerations and first results. Rapid Commun Mass Spectrom 16 (9), 891–898.

Gunina, A., Dippold, M.A., Glaser, B., Kuzyakov, Y., 2014. Fate of low molecular weight organic substances in an arable soil: from microbial uptake to utilisation and stabilisation. Soil Biol. Biochem. 77, 304–313.

Hall, S.J., Ye, C., Weintraub, S.R., Hockaday, W.C., 2020. Molecular trade-offs in soil organic carbon composition at continental scale. Nat. Geosci. 13 (10), 687–692.

Hannula, S.E., Morriën, E., 2022. Will fungi solve the carbon dilemma? Geoderma 413, 115767.

Hassink, J., 1997. The capacity of soils to preserve organic C and N by their association with clay and silt particles. Plant and Soil.

Hupe, A., Schulz, H., Bruns, C., Joergensen, R.G., Wichern, F., 2016. Digging in the dirt–inadequacy of belowground plant biomass quantification. Soil Biol. Biochem. 96, 137–144.

Kanders, M.J., Berendonk, C., Fritz, C., Watson, C., Wichern, F., 2017. Catch crops store more nitrogen below-ground when considering rhizodeposits. Plant and Soil 417, 287–299.

Khan, K.S., Mack, R., Castillo, X., Kaiser, M., Joergensen, R.G., 2016. Microbial biomass, fungal and bacterial residues, and their relationships to the soil organic matter C/N/P/S ratios. Geoderma 271, 115–123.

Kopittke, P.M., Berhe, A.A., Carrillo, Y., Cavagnaro, T.R., Chen, D., Chen, Q.-L., Román Dobarco, M., Dijkstra, F.A., Field, D.J., Grundy, M.J., He, J.-Z., Hoyle, F.C., Kögel-Knabner, I., Lam, S.K., Marschner, P., Martinez, C., McBratney, A.B., McDonald-Madden, E., Menzies, N.W., Mosley, L.M., Mueller, C.W., Murphy, D.V., Nielsen, U. N., O'Donnell, A.G., Pendall, E., Pett-Ridge, J., Rumpel, C., Young, I.M., Minasny, B., 2022. Ensuring planetary survival: the centrality of organic carbon in balancing the multifunctional nature of soils. Crit. Rev. Environ. Sci. Technol. 1–17.

Kravchenko, A.N., Guber, A.K., Razavi, B.S., Koestel, J., Quigley, M.Y., Robertson, G.P., Kuzyakov, Y., 2019. Microbial spatial footprint as a driver of soil carbon stabilization. Nat Commun 10 (1), 3121.

Lehmann, J., Hansel, C.M., Kaiser, C., Kleber, M., Maher, K., Manzoni, S., Nunan, N., Reichstein, M., Schimel, J.P., Torn, M.S., Wieder, W.R., Kögel-Knabner, I., 2020. Persistence of soil organic carbon caused by functional complexity. Nat. Geosci. 13 (8), 529–534.

Lewandowski, T.E., Forrester, J.A., Mladenoff, D.J., Stoffel, J.L., Gower, S.T., D'Amato, A.W., Balser, T.C., 2015. Soil microbial community response and recovery following group selection harvest: temporal patterns from an experimental harvest in a US northern hardwood forest. For. Ecol. Manage. 340, 82–94.

Liang, C., Read, H.W., Balser, T.C., 2012. GC-based detection of aldononitrile acetate derivatized glucosamine and muramic acid for microbial residue determination in soil. JoVE (journal of Visualized Experiments) 63, e3767.

Liang, C., Schimel, J.P., Jastrow, J.D., 2017. The importance of anabolism in microbial control over soil carbon storage. Nat Microbiol 2, 17105.

Liang, C., Amelung, W., Lehmann, J., Kastner, M., 2019. Quantitative assessment of microbial necromass contribution to soil organic matter. Glob Chang Biol 25 (11), 3578–3590.
Marx, M.C., Wood, M., Jarvis, S.C., 2001. A microplate fluorimetric assay for the study of enzyme diversity in soils. Soil Biol. Biochem. 33 (12–13), 1633–1640.
Marx, M.C., Kandeler, E., Wood, M., Wermbter, N., Jarvis, S.C., 2005. Exploring the enzymatic landscape: distribution and kinetics of hydrolytic enzymes in soil particle-size fractions. Soil Biol. Biochem. 37 (1), 35–48.
Mendoza, O., De Neve, S., Deroo, H., Li, H., Sleutel, S., 2022. Do interactions between application rate and native soil organic matter content determine the degradation of exogenous organic carbon? Soil Biol. Biochem. 164.
Nguyen, T.T., Cavagnaro, T.R., Thanh Ngo, H.T., Marschner, P., 2016. Soil respiration, microbial biomass and nutrient availability in soil amended with high and low C/N residue – influence of interval between residue additions. Soil Biol. Biochem. 95, 189–197.
Parkin, T.B., Doran, J.W., Franco-Vizcaíno, E., 1997. Field and laboratory tests of soil respiration. Methods for Assessing Soil Quality 49, 231–245.
Post, W.M., Emanuel, W.R., Zinke, P.J., Stangenberger, A.G., 1982. Soil carbon pools and world life zones. Nature 298 (5870), 156–159.
Rousk, J., Baath, E., 2007. Fungal and bacterial growth in soil with plant materials of different C/N ratios. FEMS Microbiol Ecol 62 (3), 258–267.
Rousk, J., Frey, S.D., 2015. Revisiting the hypothesis that fungal-to-bacterial dominance characterizes turnover of soil organic matter and nutrients. Ecol. Monogr. 85 (3), 457–472.
Rui, Y., Murphy, D.V., Wang, X., Hoyle, F.C., 2016. Microbial respiration, but not biomass, responded linearly to increasing light fraction organic matter input: consequences for carbon sequestration. Scientific Report 6, 35496.
Sanderman, J., Hengl, T., Fiske, G.J., 2017. Soil carbon debt of 12,000 years of human land use. Proc Natl Acad Sci U S A 114 (36), 9575–9580.
Scharlemann, J.P.W., Tanner, E.V.J., Hiederer, R., Kapos, V., 2014. Global soil carbon: understanding and managing the largest terrestrial carbon pool. Carbon Manage. 5 (1), 81–91.
Schimel, J.P., Schaeffer, S.M., 2012. Microbial control over carbon cycling in soil. Front Microbiol 3, 348.
Sinsabaugh, R.L., Lauber, C.L., Weintraub, M.N., Ahmed, B., Allison, S.D., Crenshaw, C., Contosta, A.R., Cusack, D., Frey, S., Gallo, M.E., Gartner, T.B., Hobbie, S.E., Holland, K., Keeler, B.L., Powers, J.S., Stursova, M., Takacs-Vesbach, C., Waldrop, M. P., Wallenstein, M.D., Zak, D.R., Zeglin, L.H., 2008. Stoichiometry of soil enzyme activity at global scale. Ecol Lett 11 (11), 1252–1264.
Six, J., Frey, S.D., Thiet, R.K., Batten, K.M., 2006. Bacterial and fungal contributions to carbon sequestration in agroecosystems. Soil Sci. Soc. Am. J. 70 (2), 555–569.
Soares, M., Rousk, J., 2019. Microbial growth and carbon use efficiency in soil: links to fungal-bacterial dominance, SOC-quality and stoichiometry. Soil Biol. Biochem. 131, 195–205.
Sommer, J., Dippold, M.A., Zieger, S.L., Handke, A., Scheu, S., Kuzyakov, Y., 2017. The tree species matters: belowground carbon input and utilization in the myco-rhizosphere. Eur. J. Soil Biol. 81, 100–107.
Steffens, M., Rogge, D.M., Mueller, C.W., Hoschen, C., Lugmeier, J., Kolbl, A., Kogel-Knabner, I., 2017. Identification of distinct functional microstructural domains controlling C storage in soil. Environ Sci Technol 51 (21), 12182–12189.
Stewart, C.E., Paustian, K., Conant, R.T., Plante, A.F., Six, J., 2007. Soil carbon saturation: concept, evidence and evaluation. Biogeochemistry 86 (1), 19–31.
Stewart, C.E., Plante, A.F., Paustian, K., Conant, R.T., Six, J., 2008. Soil carbon saturation: linking concept and measurable carbon pools. Soil Sci. Soc. Am. J. 72 (2), 379–392.
Stockmann, U., Padarian, J., McBratney, A., Minasny, B., de Brogniez, D., Montanarella, L., Hong, S.Y., Rawlins, B.G., Field, D.J., 2015. Global soil organic carbon assessment. Glob. Food Sec. 6, 9–16.
Stone, M.M., DeForest, J.L., Plante, A.F., 2014. Changes in extracellular enzyme activity and microbial community structure with soil depth at the Luquillo critical zone observatory. Soil Biol. Biochem. 75, 237–247.
Sylvia, D.M., Fuhrmann, J.J., Hartel, P.G., Zuberer, D.A., 2005. Principles and applications of soil microbiology. Pearson.
van Wesemael, B., Chartin, C., Wiesmeier, M., von Lützow, M., Hobley, E., Carnol, M., Krüger, I., Campion, M., Roisin, C., Hennart, S., Kögel-Knabner, I., 2019. An indicator for organic matter dynamics in temperate agricultural soils. Agr Ecosyst Environ 274, 62–75.
Wang, B., An, S., Liang, C., Liu, Y., Kuzyakov, Y., 2021. Microbial necromass as the source of soil organic carbon in global ecosystems. Soil Biol. Biochem. 162.
Wang, Q., He, T., Wang, S., Liu, L., 2013. Carbon input manipulation affects soil respiration and microbial community composition in a subtropical coniferous forest. Agric. For. Meteorol. 178–179, 152–160.
Wang, Q., Wang, S., He, T., Liu, L., Wu, J., 2014. Response of organic carbon mineralization and microbial community to leaf litter and nutrient additions in subtropical forest soils. Soil Biol. Biochem. 71, 13–20.
Wichern, F., Eberhardt, E., Mayer, J., Joergensen, R.G., Müller, T., 2008. Nitrogen rhizodeposition in agricultural crops: methods, estimates and future prospects. Soil Biol. Biochem. 40 (1), 30–48.
Wichern, F., Andreeva, D., Joergensen, R.G., Kuzyakov, Y., 2011. Stem labeling results in different patterns of 14C rhizorespiration and 15N distribution in plants compared to natural assimilation pathways. J. Plant Nutr. Soil Sci. 174 (5), 732–741.
Wiesmeier, M., Hübner, R., Dechow, R., Maier, H., Spörlein, P., Geuß, U., Hangen, E., Reischl, A., Schilling, B., von Lützow, M., Kögel-Knabner, I., 2014a. Estimation of past and recent carbon input by crops into agricultural soils of Southeast Germany. Eur. J. Agron. 61, 10–23.
Wiesmeier, M., Hubner, R., Sporlein, P., Geuss, U., Hangen, E., Reischl, A., Schilling, B., von Lutzow, M., Kogel-Knabner, I., 2014b. Carbon sequestration potential of soils in Southeast Germany derived from stable soil organic carbon saturation. Glob. Chang. Biol. 20 (2), 653–665.
Wiesmeier, M., Urbanski, L., Hobley, E., Lang, B., von Lützow, M., Marin-Spiotta, E., van Wesemael, B., Rabot, E., Ließ, M., Garcia-Franco, N., Wollschläger, U., Vogel, H.-J., Kögel-Knabner, I., 2019. Soil organic carbon storage as a key function of soils - a review of drivers and indicators at various scales. Geoderma 333, 149–162.
Wu, T., Ost, A.D., Audinot, J.-N., Wiesmeier, M., Wirtz, T., Buegger, F., Häusler, W., Höschen, C., Mueller, C.W., 2022. Association of fresh low-molecular-weight organic compounds with clay-sized mineral fraction in soils of different organic carbon loading. Geoderma 409.
Zheng, Q., Hu, Y., Zhang, S., Noll, L., Böckle, T., Richter, A., Wanek, W., 2019. Growth explains microbial carbon use efficiency across soils differing in land use and geology. Soil Biol. Biochem. 128, 45–55.
Zvomuya, F., Janzen, H.H., Larney, F.J., Olson, B.M., 2008. A long-term field bioassay of soil quality indicators in a semiarid environment. Soil Sci. Soc. Am. J. 72 (3), 683–692.

Study 3

Wu, T., Ost, A. D., Wichern, F., Buegger, F., Audinot, J. N., Wirtz, T., Höschen, C., & Mueller, C. W

Microtopography of soil aggregates determines the retention of freshly added organic matter

In preparation for publication

Microtopography of soil aggregates determines the retention of freshly added organic matter

- Two first authors (equal contribution): Tianyi Wu, Alexander Ost
- Co-authors: Carmen Höschen, Carsten W. Mueller, Tom Wirtz, Jean-Nicolas Audinot (order to be discussed)

Abstract

Limitations in analytical methods often impair our understanding of how soil structure features affect the persistence of soil organic matter at the micro to nanoscale. In this study, we introduced a novel analytical method, which combines the analysis of 3D structures with resolution down to nm scale and element mapping with the distribution of stable isotopes at sub-µm scale. This method revealed the impact of the topography of microaggregates on the retention of newly added OM. We made use of soil samples with the same mineralogy along a gradient in soil C and N contents, that were amended with two ^{13}C and ^{15}N labeled plant residues that differed in C/N ratio and incubated for 90 days. After the incubation we obtained soil microaggregates using a dry-sieving method, to ensure no sorption-desorption of mineral-associated organic matter (MAOM) due to the use of liquid, which yield macroaggregates (> 250 µm), large microaggregates (53-250 µm), and small microaggregates (< 53 µm). The small microaggregate fraction was further prepared using a liquid-free method for the spectromicroscopic imaging using nanoscale secondary ion mass spectrometry (NanoSIMS) and helium ion microscopy (HIM). The conventional isotope ratio mass spectrometer (IRMS) analysis revealed that microaggregates were highly enriched in ^{13}C and ^{15}N and thus retained a larger amount of freshly added OM than macroaggregates. We could not demonstrate any spatial correlation between the OM hot spots derived from the newly added plant residues and any measured inorganic

element distribution as shown by the 2D element mapping by NanoSIMS. Nevertheless, by applying our 4D analysis combining NanoSIMS and HIM we could demonstrate for the first time that at a sub-µm scale, the freshly added OM preferentially retained on mineral surfaces with incidence angles of 44.60° ± 23.25 throughout the analyzed soils and treatments. We thus demonstrate that the µm scale architecture of soil microaggregates directly affects the association of OM, and thus presumably determines the fate of fresh OM together with the persistence of MAOM. Our findings underscore the critical need for correlative microscopy at previously unresolved sub-µm spatial scales to better understand how soil microscale composition and architecture is linked with the fate of SOM.

1. Introduction

Promoting soil organic matter (SOM) storage and persistence in soil systems is of great interest to support healthy and functioning soils in the face of a rapidly changing climate (Kopittke et al., 2022). Besides the environmental benefits, higher SOM storage is often associated with better conditions for crop production, consequently improving food security worldwide (Lal, 2016). The mechanisms responsible for carbon (C) storage depend on various factors, including land use, soil types, and climate conditions. Nonetheless, sorption and protection within aggregates are recognized as major mechanisms contributing to SOM storage (Kögel-Knabner and Amelung, 2021). Traditionally, clay mineral surfaces have been considered a significant factor in promoting C storage, mainly through surface sorption, which is commonly analyzed using the measurement of the specific surface area by nitrogen (N2) adsorption (Mayer, 1994). With the advent of new microscopy and spectromicroscopy techniques, more direct measurements of the actual biogeochemical interfaces of OM and minerals were possible at the scale at which these processes occur (micro to nanoscale) (Lehmann and Kleber, 2015). However, limitations in these measurements, such as the influence of microscale surface topography on data quality, often preclude accurate measurements of organic matter storage in soils (Mueller et al., 2012). It is also clear that the microscale distribution of SOM on mineral surfaces and thus on soil microstructures and its drivers are of key interest to better understand and subsequently manage MAOM.

In this context, applying analytical techniques that account for the three-dimensional (3D) nature of soil and its components are crucial to gain more comprehensive interpretations of various key soil processes e.g. C storage, pollutant sorption, plant nutrient acquisition. Micro-CT has been a common technique for evaluating 3D soil

structure features such as porosity and soil-plant interaction (Munkholm et al., 2012; Roose et al., 2016; Schlüter et al., 2022). Nonetheless, the sub-micron isotopic distribution information is limited in the 2D image which relies on NanoSIMS measurement (Mueller et al., 2012; Lippold et al., 2023; Amelung et al., 2024). The combination of NanoSIMS with Helium Ion Microscopy (HIM) represents an approach with tremendous spatial resolution to overcome topography limitations in evaluating the soil microstructure influence on organic matter storage, as it enables overlap secondary electron images to reconstruct the soil topography in 3D, thus a four-dimensional (4D) analysis (Ost et al., 2021). Thus, combining HIM with NanoSIMS represents an interesting approach to better understand the interrelation of mineral assemblages microtopography with the microscale soil organic matter distribution.

To follow the fate of freshly added organic matter in such microscale soil assemblages we used isotopic labelling that was tracked using NanoSIMS. To circumvent possible desorption processes of fresh OM adsorbed on mineral surfaces, we developed a liquid-free sample preparation method of soil microaggregates to simplify sample preparation and to keep the 3D structure undisturbed. As the inherent OM coverage of soil minerals determines the fate of freshly added OM we used soils with different soil carbon loading for the experiment. We hypothesized that 1) the microtopography of soil aggregates, and 2) both initial soil organic matter content and the carbon-to-nitrogen (C/N) ratio of the added organic matter significantly influence the retention of freshly added OM in soil microaggregates.

2. Material and methods

2.1 Soil samples and plant residues

Three agricultural soils with a SOC gradient due to differences in management were used in this study to compare agricultural soils with different C loading. Soils were collected from a long-term experimental field in Puch (details are described by Wu et al. (2022)). All three soils are characterized as Luvisols derived from loess deposits (IUSS Working Group WRB, 2015) and share comparable soil mineralogy since their locations are close.

The composite sample of each soil was done by sampling the upper 10 cm of the Ap horizon at randomly selected locations (five spots per plot) and mixing thoroughly. The fresh soil samples were air-dried at room temperature and sieved at 2 mm mesh size. Macroscale plant residues were picked out by hand. Next, sub-samples were taken from each soil to determine of soil characterization (Table 1). According to the SOC content, we referred to the soil substrate as low-C, medium-C, and high-C soil in the following study. The initial SOC content is referred to as C content.

Table 1 Soil characteristics of low-C, medium-C, and high-C soil. Modified according to (Wu et al., 2024).

Soil	Soil management	Total C content (mg g^{-1})	Total N content (mg g^{-1})	C/N	Clay and fine silt content (%)	POM (%)
Low-C soil	Bare fallow	6.4 ± 0.1	0.8 ± 0.0	8.4 ± 0.1	36.8	0.2
Medium-C soil	Three crop rotation	12.5 ± 0.0	1.4 ± 0.0	9.0 ± 0.2	45.0	0.5
High-C soil	Direct seeding	20.7 ± 0.0	2.1 ± 0.0	9.9 ± 0.2	50.1	0.9

Oat and pea were chosen to study the OM retention of plant residue with different C/N ratios. Plants were cultivated in arable soil within a greenhouse and underwent ^{13}C and ^{15}N labeling. Specifically, ^{13}C labeling was achieved through multiple pulsed leave labeling using ^{13}C-glucose, while ^{15}N labeling was accomplished via the application of ^{15}N-labeled fertilizer to the soil. Four weeks post-planting, leaves were subjected to a ten-day multiple pulsed labeling using a 2% (w/v) ^{13}C-glucose solution. One leaf was enclosed in a 2 mL vial containing the sterile solution. After complete uptake, the vial received additional ^{13}C-glucose solution. After two weeks of growth, the leaf in the vial was removed and excluded in the experiment. Plant stems and the rest of the leaves were harvested, air-dried, and subsequently finely ground. The plant litter C and N analyses were given in Table 2.

Table 2 Plant litter C and N contents.

Plant powder	**C content (mg g^{-1})**	**^{13}C atom%**	**N content (mg g^{-1})**	**^{15}N atom%**	**C/N**
Oat (*Avena sativa* L.)	440	2.18	15.9	4.0	27.8
Pea (*Pisum sativum* L.)	432	1.69	40.2	2.0	10.7

2.2 Incubation experiment

In brief, a 3 x 3 design with three soils (low-, medium-, and high-C) and three plant residues (control, oats, and peas) with five replicates was performed in this experiment. The plant residues were added to 50 g soil samples in amounts of 0 mg g^{-1} (control), and 10 mg g^{-1} (equivalent to 0 and 13 Mg ha^{-1}) at the beginning of the experiment. Each sample was well mixed and placed in a polyvinyl chloride (PVC)

cylinder of 50 mm in height with a 45.2 mm inner diameter. To hold the sample in the cylinder and allow free drainage, a mono-layer mesh (100% polyester, mesh size 55 µm) was fixed at the bottom with a ring (O-ring, nitrile rubber). Then the cylinder was placed on a metal grid to allow better gas exchange and placed in a 473 ml glass jar (gas-tight, Mason Glass, KoRo) with a lid. The incubation experiment was considered as started once the water was added as fine droplets to the soils. The moisture of the samples was adjusted to 50% water holding capacity and controlled every 2 days by weighing. The incubation was carried out in a dark thermostatic room at 22℃ for 90 days. During the incubation, the jars were partly opened to avoid anaerobic conditions. After 90 days of incubation, each sample was mixed thoroughly and immediately frozen in liquid nitrogen to stop any biological activity. Subsequently the samples were freeze-dried to yield dry soil material.

2.3 Aggregate fractionation

A dry separation procedure, adapted from Felde et al. (2021), was used to fractionate the soils into different soil aggregates without any slaking effects due to wet sieving. In brief, 10 g of freeze-dried sample was transferred to a modified Casagrande apparatus (Mennerich Geotechnik, Hannover, Germany) equipped with three sieves and a collecting tray at the bottom. The sample was separated by mechanical force with tap frequency of 2 Hz for 1000 cycles <53 µm, 53-250 µm, and > 250 µm.

2.4 Chemical analysis

Carbon and nitrogen content of all bulk soils were determined before the experiment in duplicate by dry combustion using a CN elemental analyzer (HEKAtech, Wegberg, Germany). The ^{13}C and ^{15}N enrichment, as well as the total carbon (C) and nitrogen (N) concentrations of the aggregates after the incubation were measured by an isotope

ratio mass spectrometer (IRMS, Delta V Advantage, Thermo Fisher, Dreieich, Germany), coupled to an elemental analyzer (EuroEA, Eurovector, Pavia, Italy). The enrichment is given in atom-% (at%).

Calculation

The share of plant litter-derived ^{13}C ($f_{plant\ C}$) and ^{15}N ($f_{plant\ N}$)) in the sample was calculated as follows:

$$f_{plant\ C} = {}^{13}C_{sample} - {}^{13}C_{control} \Big/ {}^{13}C_{plant} - {}^{13}C_{control}$$

Equation 1

$$f_{plant\ N} = {}^{15}N_{sample} - {}^{15}N_{control} \Big/ {}^{15}N_{plant} - {}^{15}N_{control}$$

Equation 2

where ${}^{13}C_{sample}$, ${}^{13}C_{Control}$, and ${}^{13}C_{plant}$ represent the content of ^{13}C in at% in the sample, control soil, and plant litter, respectively. ${}^{15}N_{sample}$, ${}^{15}N_{Control}$, and ${}^{15}N_{plant}$ represent the content of ^{15}N in at% in the sample, control soil, and plant litter, respectively.

The plant derived C in each aggregate fraction ($C_{plant\ derived}$) was calculated using the share of plant litter-derived ^{13}C ($f_{plant\ C}$), the C content of the aggregate fraction (C), and the proportion of the aggregate in the soil ($Aggregate\ fraction(\%)$).

$$C_{plant\ derived}(mg * g^{-1}) = f_{plant\ C} * C(mg * g^{-1}) * Aggregate\ fraction(\%)$$

The distribution of plant derived C in each fraction ($f\%$) was calculated according to the plant derived C in each aggregate fraction ($C_{plant\ derived}$), and the total plant derived C recovered from each fraction ($C_{revocered}$):

$$f\% = 100\% * {C_{plant\ derived}}/{C_{recovered}}$$

Equation 3

2.5 Surface and structure analysis

2.5.1 Sample preparation for microscopy analysis

After 90 days of incubation, we investigated the spatial distribution of specific elements on the surface and the architecture of microaggregate < 53 µm using a combined approach of NanoSIMS and HIM. A few µg of the soil sample (microaggregate < 53 µm) was transferred to the center of a gallium arsenide (GaAs) wafer with the size of 7 * 7 mm. Next, the sample with the wafer was stored at -18℃ for 20 min, then moved to room temperature. Due to the temperature difference, a condensed water film formed between wafer and samples, which led to the adhesion of the microaggregates on the wafer after air drying. Prior to analysis, a 15 nm gold coating using a sputter coater was applied to each sample to reduce possible charging effects during HIM and NanoSIMS analysis.

2.5.2 Structural analysis

HIM was used to acquire the physical information of the 3D architecture of the microaggregates. The Secondary Electron (SE) images were acquired in a ZEISS ORION Nanofab HIM with an add-on SIMS system. For all soil microaggregates, SE images were acquired with a 20 keV He+ ion beam of 0.5 pA for a frame of 1024 × 1024 pixels using an average of 4 lines at 10 µs/pixel (Field of View (FOV) of 20 µm for the SE image series). The SE images of each microaggregate was acquired every 15° at 45° tilt and every 24° at 54° tilt. Afterwards, the software Meshlab was used for 3D structure reconstruction of the microaggregates.

2.5.3 Curvature analysis

The curvature analysis was done according to Ost et al. (2021). A density of around 230 3D data point per μm^2 were measured on each microaggregate. The local curvature σk for each 3D point k was then calculated with respect to its 230 closest neighbors using the following equation (Wilke, 2002):

$$\sigma_k = \frac{1}{N}\sum_{i=1}^{N} \theta_{k,i}$$

Equation 4

where N is the number of considered nearest neighbors (here 230) and θk,i is the angle between the normal vector of 3D point k and the normal vector of the its nearest neighbor.

2.5.4 Surface element distribution

Microscale spatial distribution of elements on the surface of soil microaggregates was measured using a Cameca NanoSIMS 50L (Cameca, Gennevilliers, France). The Cesium source (Cs^+) (16 keV, 2 pA) was used as primary ion beam on the sample surface to detect the secondary ion distribution at 256 × 256 pixels, 1 ms/pixel, sum over 60 planes per image, FOV 15 µm. For each NanoSIMS measurement, seven masses, 16 (^{16}O), 24 ($^{12}C^{12}C$), 25 ($^{12}C^{13}C$), 26 ($^{12}C^{14}N$), 27($^{12}C^{15}N$), 43 ($^{27}Al^{16}O$) and 72 ($^{56}Fe^{16}O$), were located simultaneously. The distribution of Si, Al, Fe, Ca, Mg, K, and Na was revealed by the oxygen source (O^-). Microaggregates and primary particles of control group was measured before each samples of corresponding treatments and its $^{13}C^{12}C/^{12}C^{12}C$ and $^{12}C^{15}N/^{12}C^{14}N$ ratio were used as reference to normalize the enrichment of microaggregates of treatments. NanoSIMS data analysis method was adapted from Schweizer et at. (2018) using the OpenMIMS plugin in

ImageJ for dead time correction and Ilastik (1.3.3rc2) for pixel classification and segmentation.

To visualize OM distribution, a single RGB image was created for each measurement analyzed by Cesium source, combining O, C, and N in red, green, and blue, respectively.

2.5.5 4D analysis

The element distribution from NanoSIMS analyses were projected onto their corresponding 3D models using Meshlab (Cignoni et al., 2008). In brief, reference points were chosen manually to align the SIMS information to their 3D model. The element distribution was projected onto the 3D structure and a SIMS texture map was created. All black pixels, indicating no secondary ions were detected, were removed. The SIMS texture map was added to the 3D reconstruction texture map with a 60% transparency to generate a 4D presentation of a measurement, a microaggregate in our case. This 4D presentation demonstrated topography information from HIM and element distribution from NanoSIMS. When no NanoSIMS signal was acquired, only topography texture was shown in the 4D presentation.

2.6 Statistical analysis

Statistical analysis was carried out in Origin 2021 (Origin, Version 2021, OriginLab Corporation, Northampton, MA, USA.) for the datasets. First, the normality of the variance of the parameters were tested for normality using the Shapiro−Wilk test. Then, the data that passed the parametrical test were analyzed using a one-way analysis of variance (ANOVA) with Tukey's honestly significant difference test as the post hoc test. When the normality test failed, a log transformation was applied to the

raw data, and the normality was tested again. Finally, for the non-normally distributed data, Kruskal−Wallis ANOVA was applied with Dunn's test as the post hoc test.

3. Results

3.1 Aggregate size distribution

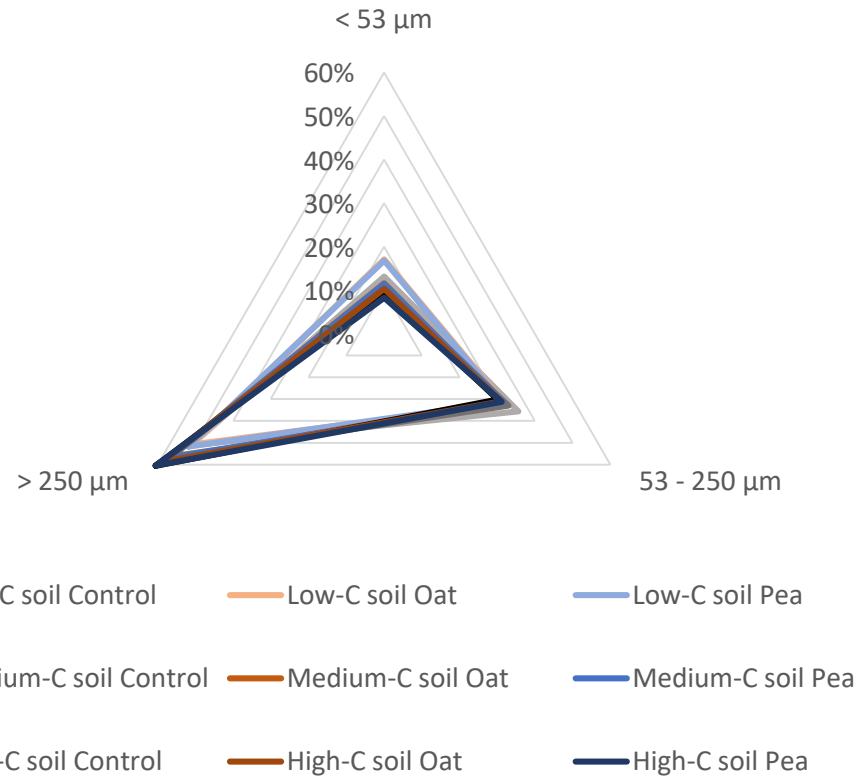

Figure 1 Aggregate size distribution of aggregate size > 250 µm, 53-250 µm, and < 53 µm of low-C, medium-C, and high-C soil of control, oat, and pea treatment.

Among all treatments and all soils, the aggregate size distribution was not significantly different. Over half of the soil dry weight was accounted for in the macroaggregate with a size > 250 µm, ranging from 51-61% for all treatments. Aggregates between 53-250 µm contributed 30-36 weight% to soils. The lowest dry weight proportion in the three aggregate sizes was microaggregate < 53 µm, which took up only 8-17% of the soils.

3.2 Plant-derived C and N distribution in the aggregates

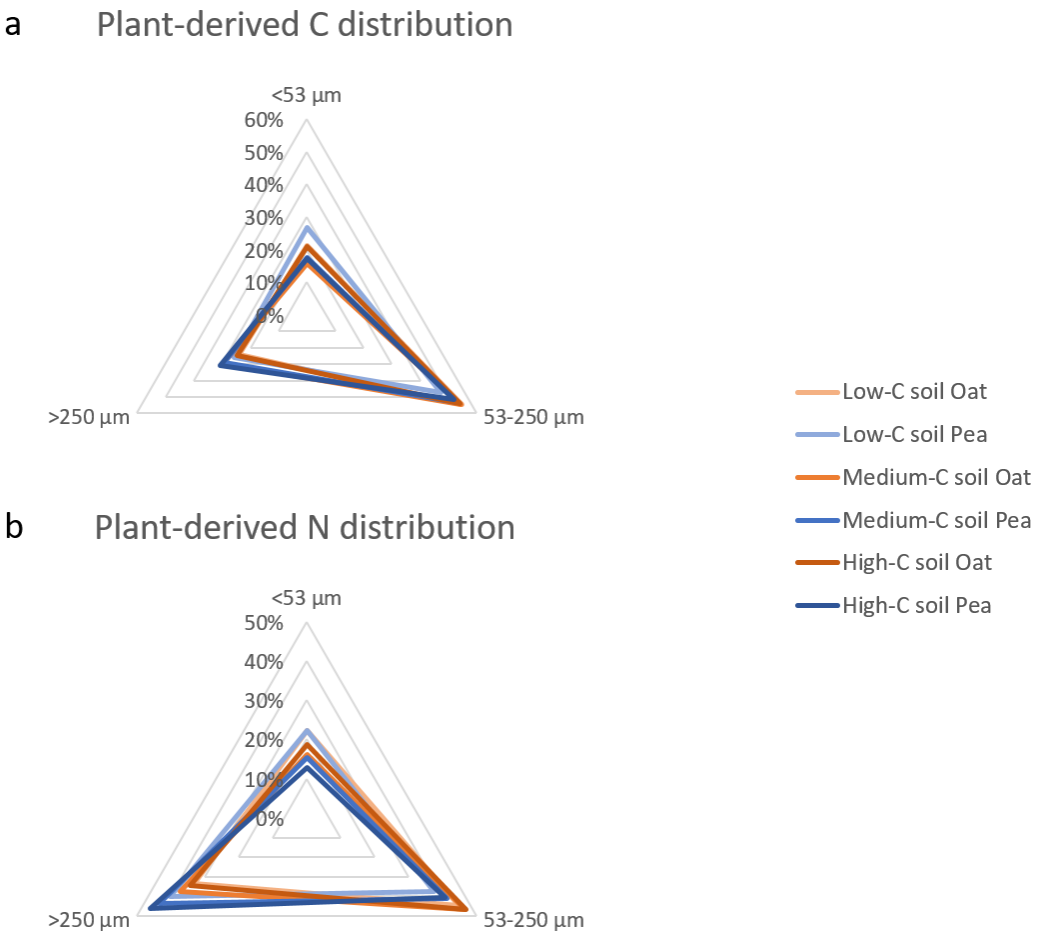

Figure 2 Plant-derived C (a) and N (b) distribution in aggregate size > 250 µm, 53-250 µm, and < 53 µm of low-C, medium-C, and high-C soil of control, oat, and pea treatment.

In our studied soils, large microaggregates (53-250 µm) were demonstrated to be the largest plant-derived OM pool among the different aggregate size classes after 90 days of incubation, retaining 47-77% of the plant-derived C.

Among the three aggregate size fractions in, the microaggregate fraction of 53-250 µm contained the highest proportion of plant-derived C, ranging from 47% to 55%. Except for the pea treatment of the low-C soil, the microaggregate fraction of < 53 µm

of both pea and oat treated low-C, medium-C, and high-C soil contained a lower proportion of plant-derived C than aggregates of > 250 µm. Microaggregates < 53 µm shared between 16% to 27% of plant-derived C, thus less than aggregates > 250 µm (24%-30% in all soils). In all three soils, the proportion of oat-derived C was higher than pea-derived C (55% vs. 47% in low-C soil, 55% vs. 53% in medium-C soil, and 54% vs. 52% in high-C soil) in microaggregates of 53-250 µm. In low-C soil, the addition of pea litter resulted in a higher plant-derived C recovery in both microaggregates < 53 µm (27%) and macroaggregates > 250 µm (26%) compared to the recovery of plant C from oat litter (21% in microaggregate < 53 µm and 24% in aggregate > 250 µm). The medium-C soil retained 16% and 18% of the plant-derived C in microaggregates < 53 µm in oat and pea treatment, respectively. In macroaggregates > 250 µm of the medium-C soil a similar proportion of plant-derived C was retained from oat (30%) and pea (29%) amendments. In high-C soil, 21% and 25% of oat C was distributed in microaggregates < 53µm and macroaggregates > 250 µm, respectively. While 17% and 31% of pea derived C were recovered in microaggregates < 53µm and macroaggregates > 250 µm in the high-C soil.

Plant-derived N was mainly distributed in larger aggregate size fractions of 53-250 µm and > 250 µm. Only 13 to 22% of plant derived N was recovered in microaggregates < 53 µm. Oat amendment led to 9%-13% higher proportion of plant derived N distributed in microaggregates of 53-250 µm compared to macroaggregates >250 µm. In microaggregates of 53-250 µm, 45%, 46%, and 47% of plant derived N was recovered in low-C, medium-C, and high-C soil, respectively. The proportion of oat-derived N in macroaggregates > 250 µm was 33% for low-C soil, 37% for medium-C soil, and 34% for high-C soil. Contrary to the oat amendment, the amendment of pea litter resulted in more plant-derived N retained in macroaggregates of >250 µm

compared to microaggregates of 53-250 µm. The proportion of pea-derived N in microaggregates of 53-250 µm vs. macroaggregates of > 250 µm was 37% vs. 40% for low-C soil, 41% vs. 44% for medium-C soil, and 41% vs. 46% for high-C soil.

3.3 ^{13}C and ^{15}N enrichment

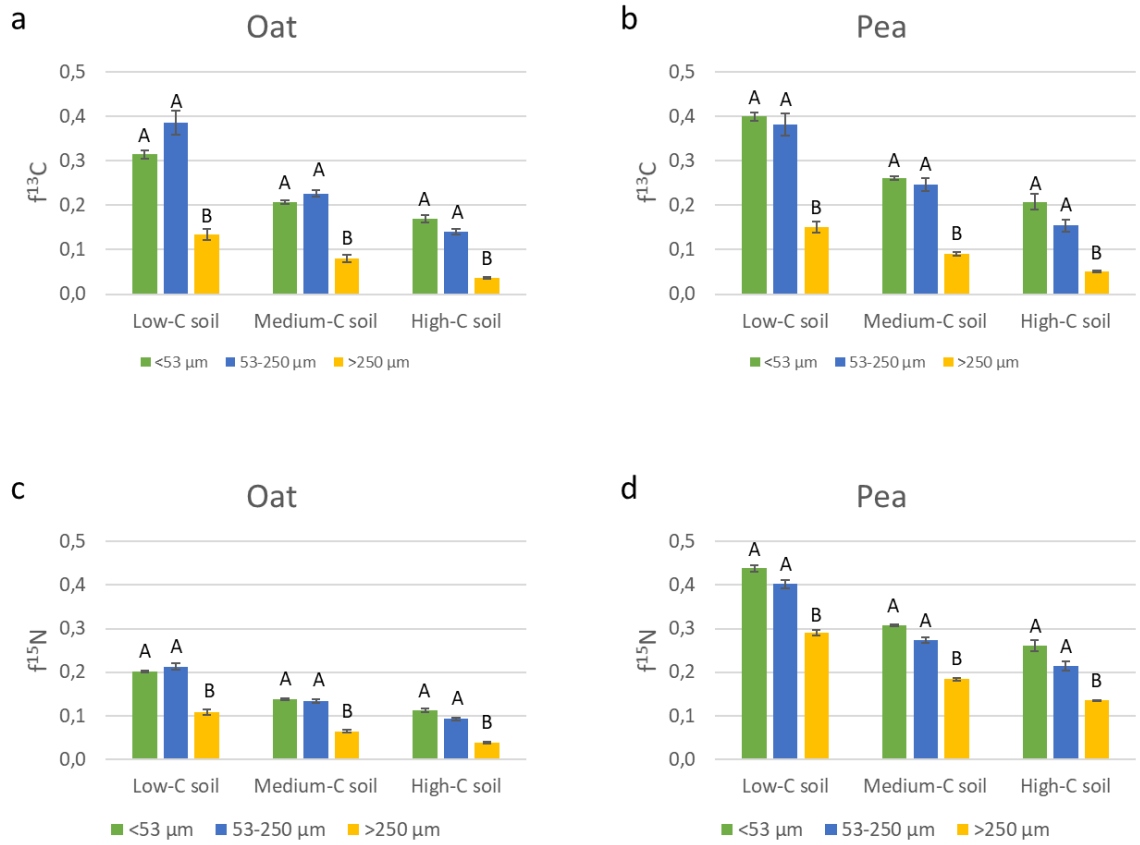

Figure 3 The share of plant-derived (a) ^{13}C of oat treatment, (b) ^{13}C of pea treatment, (c) ^{15}N of oat treatment, and (d) ^{15}N of pea treatment in aggregate size < 53 µm, 53-250 µm, and > 250 µm of low-C, medium-C, and high-C soil. Different uppercase letters indicate significant differences (P < 0.05) among the different aggregate sizes under same soil and treatment.

Based on the isotope enrichment it can be stated that in all studied soils, microaggregates (< 53µm and 53-520 µm) showed higher retention of plant derived C from both freshly added plant litter types compared to macroaggregates (> 250 µm).

In each aggregate size fraction, the contribution of plant-derived OM following low-C soil > medium-C soil > high-C soil, correlated negatively with the SOC content. In each soil under same treatment, plant-derived C and N demonstrated significant difference between microaggregates and macroaggregates.

In oat treatment, the highest $f^{13}C$ and $f^{15}N$ values were found in microaggregates of 53-250 µm (0.39 ± 0.03 and 0.21 ± 0.01), followed by microaggregates of < 53 µm (0.31 ± 0.01 for $f^{13}C$ and 0.20 ± 0.00 for $f^{15}N$) in low-C soil. In medium-C soil, the contribution of plant-derived C was higher in microaggregates of 53-250 µm compared to microaggregates < 53µm (0.23 ± 0.01 vs. 0.21 ± 0.00), but the $f^{15}N$ values were not significantly different between these two microaggregate size fractions (0.14 ± 0.00 for microaggregate < 53µm and 0.13 ± 0.00 for microaggregate 53-250 µm). For the fraction of plant-derived OM in the high-C soil a negative relationship with the aggregate size was demonstrated. The $f^{13}C$ and $f^{15}N$ of microaggregates < 53µm were 0.17 ± 0.01 and 0.11 ± 0.00, respectively, higher than these of microaggregates of 53-250 µm (0.14 ± 0.01 and 0.09 ± 0.00). In the macroaggregate fractions > 250 µm lowest contribution of plant-derived OM was recovered among the three soils amended with oat litter. The fraction of oat-derived C was less than 0.13 in macroaggregates > 250 µm of all soils (0.13 ± 0.01, 0.08 ± 0.01, and 0.04 ± 0.00 in low-C, medium-C, and high-C soil, respectively) and the fraction of oat-derived N was below 0.11 (0.11 ± 0.01 in low-C soil, 0.06 ± 0.00 in medium-C soil, and 0.04 ± 0.00 in high-C soil).

In the pea treatment, for microaggregates of < 53 µm the highest $f^{13}C$ value were demonstrated in all three soils (0.40± 0.01 for low-C soil, 0.26 ± 0.00 for medium-C soil, and 0.21 ± 0.02 for high-C soil). A significant difference was detected between the aggregate size fractions in high-C soil but not between microaggregates < 53 µm

and 53-250 µm of the low-C and medium-C soil. The fraction of pea-derived C in microaggregates of 53-250 µm was 0.38± 0.03 for low-C soil, 0.25 ± 0.01 for medium-C soil, and 0.15 ± 0.01 for high-C soil, which was 2.5 fold, 2,7 fold, and 3.0 fold of their $f^{13}C$ in aggregate > 250 µm. The fraction of pea-derived N followed the order low-C > medium-C > high-C soil in each aggregate size, and microaggregate <53 µm > microaggregate 53-250 µm > aggregate > 250 µm in each soil.

3.4 Element distribution at sub-micron scale

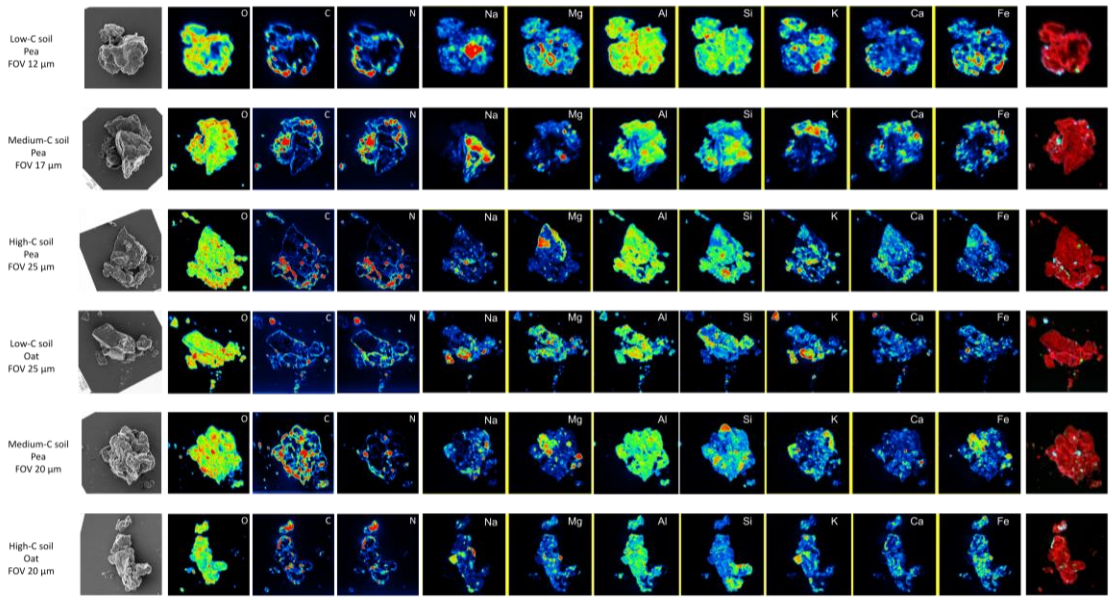

Figure 4 From up to bottom, 6 particles of low-C pea treatment, medium-C soil pea treatment, high-C soil pea treatment, low-C soil oat treatment, medium-C soil oat treatment, and high-C soil oat treatment were shown in each line. The HIM image, O, C, N, Na, Mg, Al, Si, K, Ca, Fe distribution, and RGB image were demonstrated from left to right. In RGB images, red, green, and blue represent O, C, and N, respectively.

The secondary electron images of 6 microaggregates derived from the three different soils and the two plant litter amendments were taken using HIM. Secondary ions O, C, and N were measured via NanoSIMS by using the Cs source, while for secondary

ions Na, Mg, Al, Si, K, Ca, and Fe the O source was used. The enriched OM presented a heterogeneous distribution on the microaggregates, as shown in RGB images in Figure 4. The distribution of secondary ions related to organic matter (^{12}C, ^{13}C and $^{12}C^{14}N$ and $^{12}C^{15}N$) was not co-localized with secondary ions related to inorganic soil constituents.

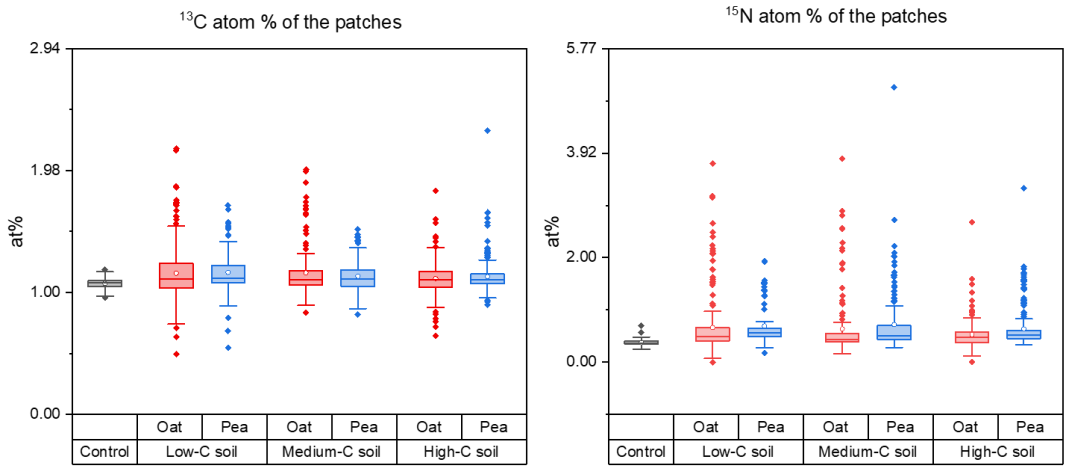

Figure 5 Boxplot of ^{13}C and ^{15}N atom-% of each OM patches of control, low-C, medium-C, and high-C soil of oat and pea treatment.

The boxplot (Figure 5) demonstrated that both enriched and non-enriched OM patches were detected in soil microaggregates of low-C, medium-C, and high-C soil of oat and pea treatment. The ^{13}C ranged between natural abundance (1.11 at%) and 1.16 at% for all six microaggregates and the 15N enrichment was between 0.54 and 0.73 at%. Based on the enrichment of OM patches of microaggregates, no significant differences between the three soils and two treatments were found.

3.5 Curvature analysis

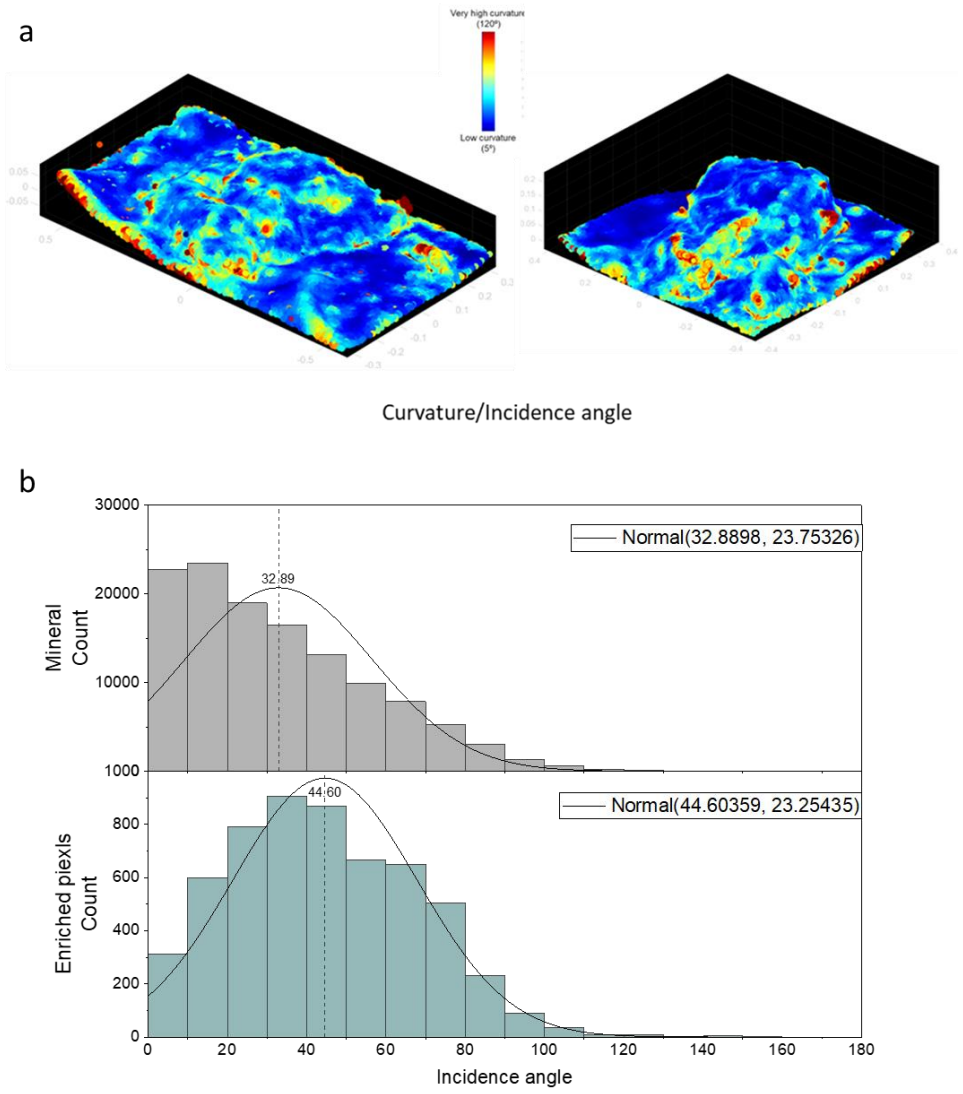

Figure 6 (a) Curvature and incidence angle of a microaggregate. (b) Histogram and normal distribution line after distribution fit of incidence angle of mineral surface and ^{13}C and/or ^{15}N enriched pixels of microaggregates.

The topography of a RIO, including a soil microaggregate, was visualized in Figure 6a with curvature. The ^{13}C and/or ^{15}N enriched pixels located at a higher incidence angle than mineral surface of the microaggregates (Figure 6b). The highest counts for the incidence angle on mineral surface were between 10° - 20°, and then decrease as the incidence angle increases. However, the incidence angle distribution for enriched ^{13}C

and ^{15}N pixels demonstrated the peak between 30° - 50°. The average incidence angle of mineral surface was 32.89° ± 23.75, which was 12° higher for enriched pixels (44.60° ± 23.25). The curvature of enriched spots among all microaggregates did not show significant difference between low-C, medium-C, and high-C soil, nor oat and pea treatment (Figure 9).

4. Discussion

4.1 Microaggregates and macroaggregates in promoting plant-derived OM retention

The higher proportion of ^{13}C and ^{15}N retained in aggregates < 53 and 53-250 μm, especially for low C soils (Figure 2), points to a more important role of microaggregates in the sequestration of newly added organic matter compared to macroaggregates. As low-C soils retained a higher proportion of ^{13}C and ^{15}N in microaggregates than medium and high-C soils, the retention of plant-derived OM is especially pronounced in more C-depleted soils.

Based on the ^{13}C and ^{15}N hot spots in the soil microaggregates(Figure 4), it is possible to demonstrate that plant-derived N distributed differently from plant-derived C, indicating a different C and N sequestration process from newly added plant residue. The distribution differences of plant-derived C and N in aggregate size fractions could be due to microbial activities, as shown in the study by (Shabtai et al., 2023) that after 112 and 135 days of incubation, the plant litter-derived C/N decreased due to the change in respiration, carbon use efficiency, and decomposer populations.

4.2 Organic matter hot spot and the role of inorganic element

Our 2D element mapping did not demonstrate any preferential colocation of newly formed MAOM (13N and 15N) with Na, Mg, Al, Si, K, Ca, or Fe (Figure 4), unlike in other studies that pointed out the Fe, Al, Ca, or Mn contribute to OM storage (e.g. (Lalonde et al., 2012; Rennert et al., 2014; Rowley et al., 2023; Shabtai et al., 2023)). As the correlation of inorganic element distribution with the newly added OM hot spot could be influenced by sample preparation methods, we have prepared the samples using liquid-free method. We fractionated the aggregates using a dry-sieving method in order to avoid any disturbance from ultrasonic energy, water, or external force, such

as density fractionation, wet sieving, and dry crushing (Krause et al., 2020; Felde et al., 2021). The dry-sieving method followed by liquid-free microaggregate fixation on the wafer highly preserved the post-incubated microstructure and the element distribution of the microaggregates. This to the maximum extent, avoids the disturbance of liquid on the aggregate, such as aggregate re-aggregation and MAOM re-distribution during the sample preparation procedure.

The lack of correlation between OM and inorganic elements has been pointed out by Lehndorff et al. (2021), who concluded no systematic link between OM and soil minerals at 1 x 1 µm resolution with electron probe micro analysis. Due to the relative low resolution (1 µm) and the larger aggregate size (20-53 µm), the correlation between OM and inorganic elements might be hidden. Nevertheless, our result is supported by incubation experiments using ^{13}C labeled organic matter additions. The studies with incubation times within the range of months causally associated ^{13}C with Fe and Al (Wilhelm et al., 2022; Almeida et al., 2023; Inagaki et al., 2023), although significant correlations between C with Fe and Al are observed at the nanoscale (Asano et al., 2018). The association between Ca addition and SOC were demonstrated in acidic grassland soils (Rowley et al., 2023) and microbial transformed OM in soils (Shabtai et al., 2023), however, we did not find strong evidence of co-location of initial Ca in the soil microaggregates and OM hot spots.

4.3 Microtopography of soil aggregates in promoting OM retention

Combining micro scale topography with the mapping of enriched OM on the surface of microaggregates, we were able to demonstrate (Figure 7) that the retention of fresh OM in organo-mineral assemblages is regulated by the architecture of the microscale mineral microstructures (Figure 6). Here, we show for the first time that newly added OM is preferentially retained on soil surface with an incidence angle around 44.60° for

the three studied soils and two plant litter additions. Pioneer work by Vogel et al. (2014) showed that especially the surfaces of microaggregates with their considerably nanoscale topography provide essential reactive interfaces for the sequestration of fresh OM in organo-mineral clusters. We further expressed the surface roughness into curvature by applying 3D analysis of a microaggregate. The curvature at each measured spot is presented as a concert number, which overcome the limitation of 2D measurement that precluded precise evaluations of microtopography.

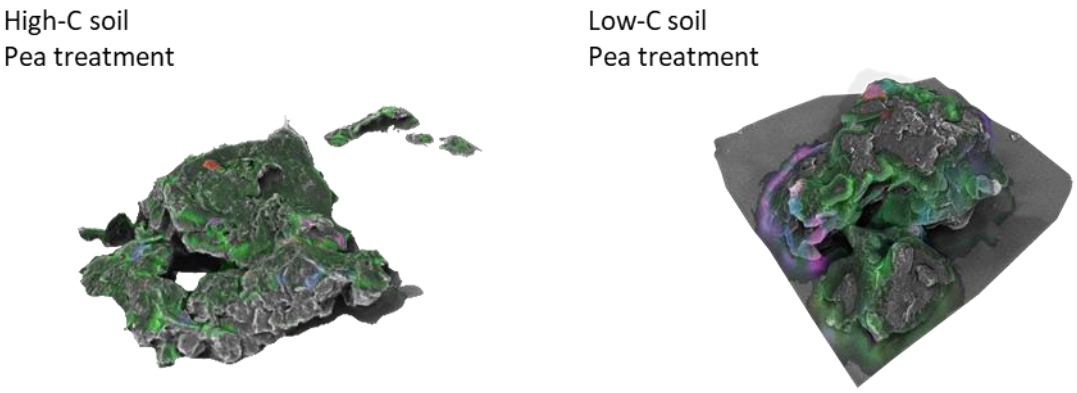

Figure 7 4D models of HE, high-C soil incubated with pea, and LE, low-C soil incubated with pea.

5. Conclusions/outlook

Our result showed that after 90 days of incubation of three agriculture soils with different plant litter inputs, the macroagregates (>250 µm) shared the highest weight proportion while the microaggregates (53-250 µm and < 53 µm) had higher ^{13}C and ^{15}N enrichment, which was 2.5 to 3.5 fold of the enrichment in macroaggregates. The 2D element mapping acquired by NanoSIMS analysis did not demonstrate strong co-localization between newly added OM (^{13}C and ^{15}N) and inorganic phases (Na, Mg, Al, Si, K, Ca, and Fe) in the sub-micron scale in any microaggregate. Notably, our 4D analysis, which combines 3D microstructure and the ^{13}C and ^{15}N distribution of the microaggregate, demonstrated that the newly added OM preferentially retained on the surface with incidence angle 44.60° ± 23.25, regardless of soil and treatment.

Appendix

C and N distribution in the aggregates

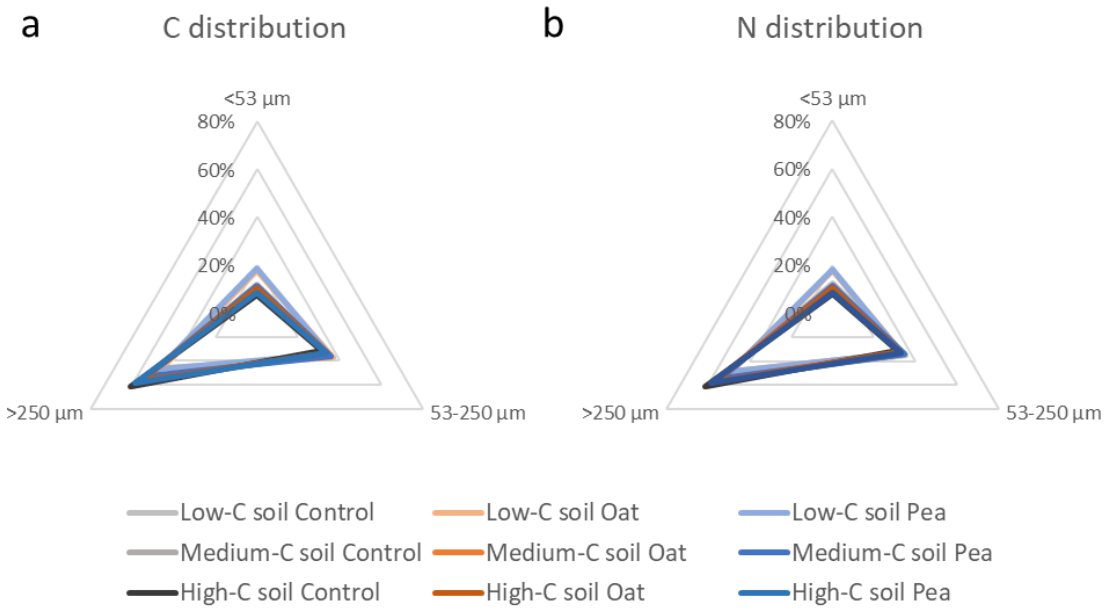

Figure 8 C (a) and N (b) distribution in aggregate size > 250 µm, 53-250 µm, and < 53 µm of low-C, medium-C, and high-C soil of control, oat, and pea treatment.

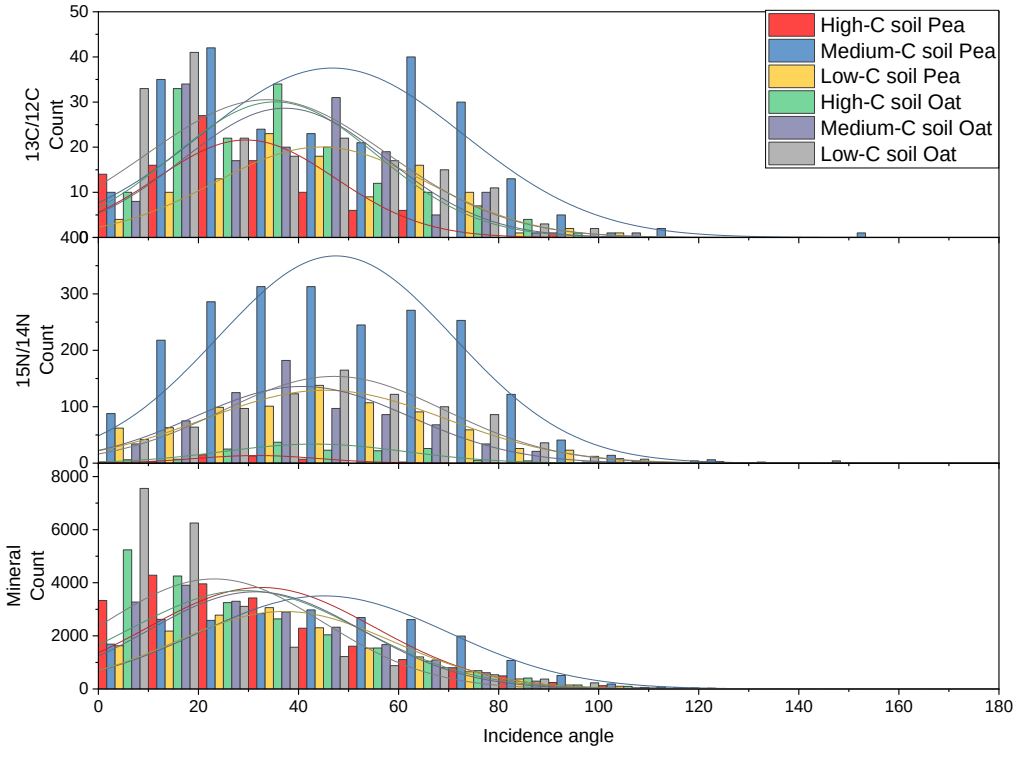

Figure 9 Histogram with normal distribution line of $^{13}C/^{12}C$, $^{15}N/^{14}N$, and mineral of six microaggregates (low-C, medium-C, and high-C soil with pea and oat treatment).

Almeida, L.F., Souza, I.F., Hurtarte, L.C., Teixeira, P.P., Inagaki, T.M., Silva, I.R., Mueller, C.W., 2023. Molecular diversity and the fate of biochemical fractions of eucalypt tissues in soil. Geoderma 432, 116404.

Amelung, W., Tang, N., Siebers, N., Aehnelt, M., Eusterhues, K., Felde, V.J., Guggenberger, G., Kaiser, K., Kögel‐Knabner, I., Klumpp, E., 2024. Architecture of soil microaggregates: Advanced methodologies to explore properties and functions. Journal of Plant Nutrition and Soil Science 187, 17-50.

Asano, M., Wagai, R., Yamaguchi, N., Takeichi, Y., Maeda, M., Suga, H., Takahashi, Y., 2018. In search of a binding agent: Nano-scale evidence of preferential carbon associations with poorly-crystalline mineral phases in physically-stable, clay-sized aggregates. Soil Systems 2, 32.

Cignoni, P., Callieri, M., Corsini, M., Dellepiane, M., Ganovelli, F., Ranzuglia, G., 2008. Meshlab: an open-source mesh processing tool, Eurographics Italian chapter conference. Salerno, pp. 129-136.

Felde, V.J., Schweizer, S.A., Biesgen, D., Ulbrich, A., Uteau, D., Knief, C., Graf‐Rosenfellner, M., Kögel‐Knabner, I., Peth, S., 2021. Wet sieving versus dry crushing: Soil microaggregates reveal different physical structure, bacterial diversity and organic matter composition in a clay gradient. European Journal of Soil Science 72, 810-828.

Inagaki, T.M., Possinger, A.R., Schweizer, S.A., Mueller, C.W., Hoeschen, C., Zachman, M.J., Kourkoutis, L.F., Kögel-Knabner, I., Lehmann, J., 2023. Microscale spatial distribution and soil organic matter persistence in top and subsoil. Soil Biology and Biochemistry 178, 108921.

Kögel-Knabner, I., Amelung, W., 2021. Soil organic matter in major pedogenic soil groups. Geoderma 384, 114785.

Kopittke, P.M., Berhe, A.A., Carrillo, Y., Cavagnaro, T.R., Chen, D., Chen, Q.-L., Román Dobarco, M., Dijkstra, F.A., Field, D.J., Grundy, M.J., He, J.-Z., Hoyle, F.C., Kögel-Knabner, I., Lam, S.K., Marschner, P., Martinez, C., McBratney, A.B., McDonald-Madden, E., Menzies, N.W., Mosley, L.M., Mueller, C.W., Murphy, D.V., Nielsen, U.N., O'Donnell, A.G., Pendall, E., Pett-Ridge, J., Rumpel, C., Young, I.M., Minasny, B., 2022. Ensuring planetary survival: the centrality of organic carbon in balancing the multifunctional nature of soils. Critical Reviews in Environmental Science and Technology, 1-17.

Krause, L., Klumpp, E., Nofz, I., Missong, A., Amelung, W., Siebers, N., 2020. Colloidal iron and organic carbon control soil aggregate formation and stability in arable Luvisols. Geoderma 374, 114421.

Lal, R., 2016. Soil health and carbon management. Food and Energy Security 5, 212-222.

Lalonde, K., Mucci, A., Ouellet, A., Gélinas, Y., 2012. Preservation of organic matter in sediments promoted by iron. Nature 483, 198-200.

Lehmann, J., Kleber, M., 2015. The contentious nature of soil organic matter. Nature 528, 60-68.

Lehndorff, E., Rodionov, A., Plümer, L., Rottmann, P., Spiering, B., Dultz, S., Amelung, W., 2021. Spatial organization of soil microaggregates. Geoderma 386, 114915.

Lippold, E., Schlüter, S., Mueller, C.W., Höschen, C., Harrington, G., Kilian, R.d., Gocke, M.I., Lehndorff, E., Mikutta, R., Vetterlein, D., 2023. Correlative imaging of the rhizosphere— a multimethod workflow for targeted mapping of chemical gradients. Environmental Science & Technology 57, 1538-1549.

Mayer, L.M., 1994. Surface area control of organic carbon accumulation in continental shelf sediments. Geochimica et Cosmochimica Acta 58.

Mueller, C.W., Kölbl, A., Hoeschen, C., Hillion, F., Heister, K., Herrmann, A.M., Kögel-Knabner, I., 2012. Submicron scale imaging of soil organic matter dynamics using NanoSIMS – From single particles to intact aggregates. Organic Geochemistry 42, 1476-1488.
Munkholm, L.J., Heck, R.J., Deen, B., 2012. Soil pore characteristics assessed from X-ray micro-CT derived images and correlations to soil friability. Geoderma 181, 22-29.
Ost, A.D., Wu, T., Hoschen, C., Mueller, C.W., Wirtz, T., Audinot, J.-N., 2021. 4D surface reconstructions to study microscale structures and functions in soil biogeochemistry. Environmental Science & Technology 55, 9384-9393.
Rennert, T., Händel, M., Höschen, C., Lugmeier, J., Steffens, M., Totsche, K., 2014. A NanoSIMS study on the distribution of soil organic matter, iron and manganese in a nodule from a S tagnosol. European Journal of Soil Science 65, 684-692.
Roose, T., Keyes, S.D., Daly, K., Carminati, A., Otten, W., Vetterlein, D., Peth, S., 2016. Challenges in imaging and predictive modeling of rhizosphere processes. Plant and soil 407, 9-38.
Rowley, M.C., Nico, P.S., Bone, S.E., Marcus, M.A., Pegoraro, E.F., Castanha, C., Kang, K., Bhattacharyya, A., Torn, M.S., Peña, J., 2023. Association between soil organic carbon and calcium in acidic grassland soils from Point Reyes National Seashore, CA. Biogeochemistry 165, 91-111.
Schlüter, S., Leuther, F., Albrecht, L., Hoeschen, C., Kilian, R., Surey, R., Mikutta, R., Kaiser, K., Mueller, C.W., Vogel, H.-J., 2022. Microscale carbon distribution around pores and particulate organic matter varies with soil moisture regime. Nature Communications 13, 2098.
Shabtai, I.A., Wilhelm, R.C., Schweizer, S.A., Höschen, C., Buckley, D.H., Lehmann, J., 2023. Calcium promotes persistent soil organic matter by altering microbial transformation of plant litter. Nature Communications 14, 6609.
Vogel, C., Mueller, C.W., Hoschen, C., Buegger, F., Heister, K., Schulz, S., Schloter, M., Kogel-Knabner, I., 2014. Submicron structures provide preferential spots for carbon and nitrogen sequestration in soils. Nat Commun 5, 2947.
Wilhelm, R.C., Lynch, L., Webster, T.M., Schweizer, S., Inagaki, T.M., Tfaily, M.M., Kukkadapu, R., Hoeschen, C., Buckley, D.H., Lehmann, J., 2022. Susceptibility of new soil organic carbon to mineralization during dry-wet cycling in soils from contrasting ends of a precipitation gradient. Soil Biology and Biochemistry 169, 108681.
Wilke, W., 2002. Segmentierung und Approximation großer Punktwolken. Technische Universität.
Wu, T., Ost, A.D., Audinot, J.-N., Wiesmeier, M., Wirtz, T., Buegger, F., Häusler, W., Höschen, C., Mueller, C.W., 2022. Association of fresh low-molecular-weight organic compounds with clay-sized mineral fraction in soils of different organic carbon loading. Geoderma 409.
Wu, T., Wichern, F., Wiesmeier, M., Buegger, F., Shi, L., Dippold, M.A., Höschen, C., Mueller, C.W., 2024. Organic carbon loading of soils determines the fate of added fresh plant-derived organic matter. Geoderma 443.

Study 4

* Co-authored study

Ost, A. D., Wu, T., Hoschen, C., Mueller, C. W., Wirtz, T., & Audinot, J. N.

4D surface reconstructions to study microscale structures and functions in soil biogeochemistry

Environmental Science & Technology 55(13) (2021) 9384-9393

https://doi.org/10.1021/acs.est.1c02971

Environmental Science & Technology

pubs.acs.org/est

Article

4D Surface Reconstructions to Study Microscale Structures and Functions in Soil Biogeochemistry

Alexander D. Ost,* Tianyi Wu, Carmen Höschen, Carsten W. Mueller, Tom Wirtz, and Jean-Nicolas Audinot

Cite This: *Environ. Sci. Technol.* 2021, 55, 9384–9393

Read Online

ACCESS | Metrics & More | Article Recommendations | Supporting Information

ABSTRACT: The development of high-resolution microscopy and spectroscopy techniques has allowed the analysis of microscopic 3D objects in fields like nanotechnology and life and soil sciences. Soils have the ability to incorporate and store large amounts of organic carbon. To study this organic matter (OM) sequestration, it is essential to analyze its association with soil minerals at the relevant microaggregate scale. This has been previously studied in 2D. However, 3D surface representations would allow a variable angle and magnification analysis, providing detailed insight on their architecture. Here we illustrate a 4D surface reconstruction workflow able to locate preferential sites for OM deposition with respect to microaggregate topography. We used Helium Ion Microscopy to acquire overlapping Secondary Electron (SE) images to reconstruct the soil topography in 3D. Then we used nanoscale Secondary Ion Mass Spectrometry imaging to chemically differentiate between the OM and mineral constituents forming the microaggregates. This image was projected onto the 3D SE model to create a 4D surface reconstruction. Our results show that organo-mineral associations mainly form at medium curvatures while flat and highly curved surfaces are avoided. This method presents an important step forward to survey the 3D physical structure and chemical composition of microscale biogeochemical systems correlatively.

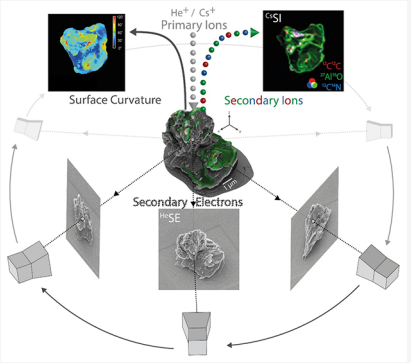

KEYWORDS: *SIMS, correlative microscopy, photogrammetry, surface reconstruction, biogeochemistry, organic matter sequestration*

1. INTRODUCTION

Correlative Microscopy (CM) has become of major importance nowadays in various domains such as nanotechnology, life, and even soil sciences. Microscopy and spectroscopy techniques are combined first to overcome limitations from each technique[1] and second to move beyond the boundaries of microscopy by data treatment.[2] Analyzing a Region of Interest (ROI) with different techniques with regards to structural and chemical properties provides complementary information and a deeper understanding about the sample.[3,4] When Secondary Ion Mass Spectrometry (SIMS) is combined with scanning or transmission electron microscopy techniques (SEM and TEM)[5] and, more recently, Helium Ion Microscopy (HIM),[6−8] CM offers high sensitivity chemical information correlated with morphology. Furthermore, correlating images obtained by different techniques using, e.g., an image overlay or the Laplace fusion method benefits the interpretation of multimodal information.[2]

SIMS is a qualitative technique for chemical surface analysis. Primary ions (e.g., Ne^+, Ga^+, Cs^+, O^-) are accelerated toward the sample, provoking the emission of secondary ions, which are collected, filtered according to their mass-to-charge ratio, and detected.[9−11] Advantages of SIMS are high sensitivity, access to the full periodic table (starting with hydrogen), distinguishability of isotopes and a high dynamic range (i.e., detectable secondary ion concentrations varying from matrix to trace elements). SIMS can be used in different modes e.g. depth profiling and imaging.

SIMS has been widely used for 3D SIMS reconstruction.[12] Sequential 2D SIMS images are obtained while eroding the surface progressively under the energetic primary ion bombardment and are then assembled into a 3D stack. However, this method does not take into account the original surface topography and its evolution during the sputtering process, since different materials and features exposed to the ion beam at different angles are sputtering at different rates.[13] The outcome is a three-dimensional block representing the ROI without any morphological information and prone to artifacts. In order to make a topography correction, AFM measurements can be performed before, as well as after,[14,15] and in-between SIMS measurements.[13,16] However, high aspect ratio particles are particularly challenging for conventional AFM due to too high scanning speed resulting in

Received: May 7, 2021
Accepted: June 9, 2021
Published: June 24, 2021

https://doi.org/10.1021/acs.est.1c02971
Environ. Sci. Technol. 2021, 55, 9384−9393

collision with the sample.[17] For this kind of samples, a photogrammetry approach has been established for 3D surface reconstruction from secondary electron (SE) images from either SEM or HIM in order to have additional information about the ROI's topography allowing a 3D view from all possible angles.[18−20]

Photogrammetry has become popular in the recent years for 3D reconstruction of macroscopic objects from images taken by a camera[21] in domains such as geography and even for soil erosion studies.[22] In general, partially overlapping images are taken around an object at different polar and azimuthal angles. The images are implemented into a photogrammetry software: features on the images are first detected and then matched at the overlapping areas from one image to another creating a point cloud by a triangulation process where matches from at least two images are required. The position of the cameras is computed and then a textured mesh is generated representing the object of interest. Therefore, the overlap from one image to another should be high to ensure enough data point detection for matching.

In recent years, Eulitz and Reiss[19] and Gontard et al.[20] have shown that this photogrammetry approach can be successfully applied to SE images of microscopic ROI's using commercial photogrammetry software specialized in reconstruction of macroscopic objects from optical images.

Vollnhals and Wirtz[18] were the first ones to extend this methodology to SE images obtained on a HIM with a specific pattern of tilt and repeating stage rotation angles. Additionally, they acquired analytical information on the same ROI by performing in situ SIMS at normal incidence and projected this SIMS information onto the 3D photogrammetric surface representations.

We note that for this photogrammetry reconstruction combined with SIMS only surface information is acquired whereas for traditional SIMS 3D reconstruction, the sample is eroded layer by layer so that volumetric chemical information is provided.[23]

Soils comprise a heterogeneous dynamic porous system that consists of mineral and organic materials of variable sizes and composition. Chemical, biological, and physical processes determine the structure and thus the function of soils, e.g., nutrient cycling, habitat for microorganisms, and soil organic carbon storage. The formation of soil aggregates, assemblages of soil minerals and organic components bound together by cementing (e.g., carbonates) and gluing agents (e.g., microbial residues) is an important control for soil functionality. Soil microaggregates (<250 μm),[24] as the smallest assemblage of mineral and organic soil constituents, are of great importance for a wide range of soil functions, besides cation exchange, soil physical stability, especially for long-term soil carbon sequestration.[25−28]

Understanding the complex 3D microscale distribution of elements and the spatial arrangement of both soil organic matter and mineral particles constituting soil microaggregates is a prerequisite to gain fundamental knowledge about the fate of soil carbon but also nutrients and pollutants in soil systems.

While Vollnhals and Wirtz[18] established the methodology of photogrammetry reconstruction combined with SIMS primarily to demonstrate its potential on basic microscopic objects (indium phosphide particles), we adapted it by appropriate workflows and applied this in the field of soil biogeochemistry.

We present here the workflow and applications of 4D surface reconstruction with two examples on soil microaggregates. Besides the illustration of the workflow and a qualitative description of a 4D surface reconstruction obtained by the analysis using the HIM-SIMS instrument, the link between the sample's chemical information delivered by nanoscale SIMS (NanoSIMS 50L) and its topography is evaluated. We provide a processing method for localization of preferential sites for organic matter (OM) sequestration with respect to the topography of soil microaggregates.

We demonstrate that correlative imaging, by a qualitative description and a deeper topographic analysis, offers the great opportunity to merge topographic and thus physical information with the distribution of elements and thus chemical data to better understand the link between soil microaggregate architecture and biogeochemical function. Furthermore, we compare two sample preparation procedures for the microscale analysis of soil microaggregates (wet and powder deposition), and make use of isotopic enrichment (^{13}C glucose) to trace the fate of freshly added OM during the formation of mineral-associated OM on the surface of microaggregates.

2. MATERIALS AND METHODS

2.1. Sample Preparation. The soil material was sampled from the upper 10 cm of the Ap horizon from a long-term agricultural research site in Puch, Germany (Cambisol according to WRB).[29] The soil was air-dried at room temperature, sieved through a 2 mm sieve and macroscopic plant residues were picked out by hand. We aimed at using state of the art approaches for the sampling and preparation of soil microaggregates, namely by the deposition of suspended microaggregates on a Si wafer and the separation of fine-sized microaggregates using sieving.[30,31] Thus, for the two presented microaggregate reconstructions, we used the most common soil sample preparation procedures and adapted them according to the intended chemical analysis.

In the first case, a 5 mL ethanol solution with a few mg of the soil sample was prepared, and some droplets were placed on a Si wafer. Due to the fine size of the deposited particles and microaggregates these were sticking to the Si carrier.

For the second microaggregate, the sample was derived from a 30 days soil incubation experiment with ^{13}C glucose (D-glucose-$^{13}C_6$, Sigma-Aldrich, ≥ 99 atom-% ^{13}C). Via dry aggregate size fractionation (adapted from Felde et al.[30]), a modified Casagrande apparatus (Mennerich Geotechnik, Hannover, Germany) equipped with three sieves was used to separate the soil material into the aggregate size fractions of <53 μm, 53−250 μm and >250 μm. As we aimed at the fine microaggregates known to store the highest relative amount of OM we used the <53 μm fraction for the microscale imaging approach. To circumvent the use of excessive water to prepare a soil suspension, we made use of condensed water films to support the fixation of microaggregates on the GaAs wafers. In brief, a few μg of the microaggregate <53 μm soil fraction was placed on a clean GaAs wafer. The wafer containing the sample was placed at −18 °C for 20 min, and subsequently, moved to room temperature. Due to the change in temperature fine water films condensed on the GaAs wafer and led to the adhesion of fine microaggregates on the surface of the wafer. This approach provides microaggregates that are fixed on the wafer and ready to be analyzed via electron microscopy and SIMS after air drying.

2.2. Helium Ion Microscopy (HIM). The Secondary Electron (SE) images were acquired in a ZEISS ORION

https://doi.org/10.1021/acs.est.1c02971
Environ. Sci. Technol. 2021, 55, 9384−9393

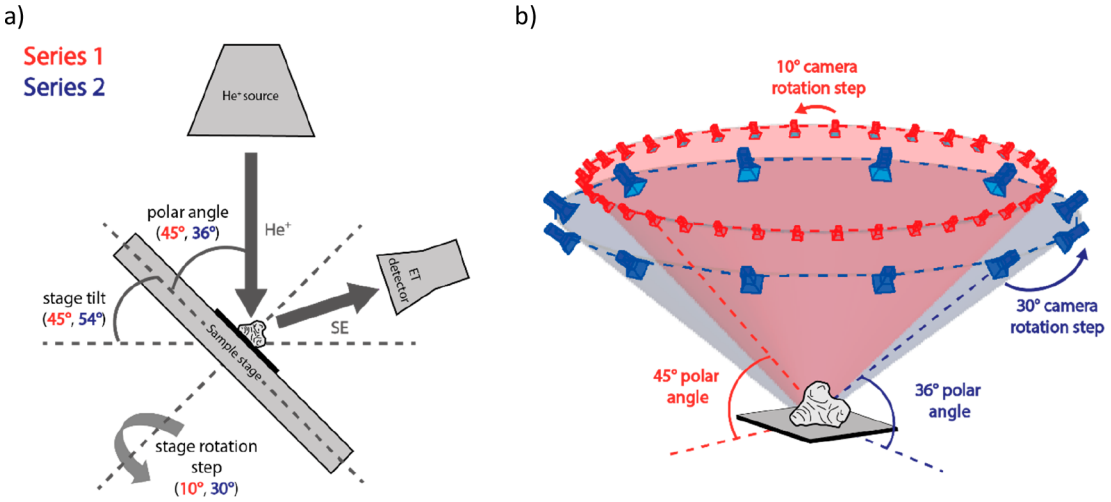

Figure 1. Sequential 2D SE image acquisition for 3D SE reconstruction. (a) The sample stage is tilted at 45° (i.e., 45° polar angle) and is rotated at 10° steps with SE image acquisitions in-between for a first SE image series (in red). In a second series (in blue), the process is repeated with a 54° stage tilt angle (i.e., 36° polar angle) and 30° rotation steps. In some cases, better results can be obtained by choosing image series at two different stage tilt (i.e., polar) angles while acquiring SE images with varying rotation angles. (b) The rotation process of the stage described in (a) is equivalent to a rotation of the camera (i.e., the He^+ source and the ET detector in the HIM) around the ROI at two different polar angles (Series 1 with red cameras: 45°, Series 2 with blue cameras: 36°) and rotation steps (Series 1:10°, Series 2:30°).

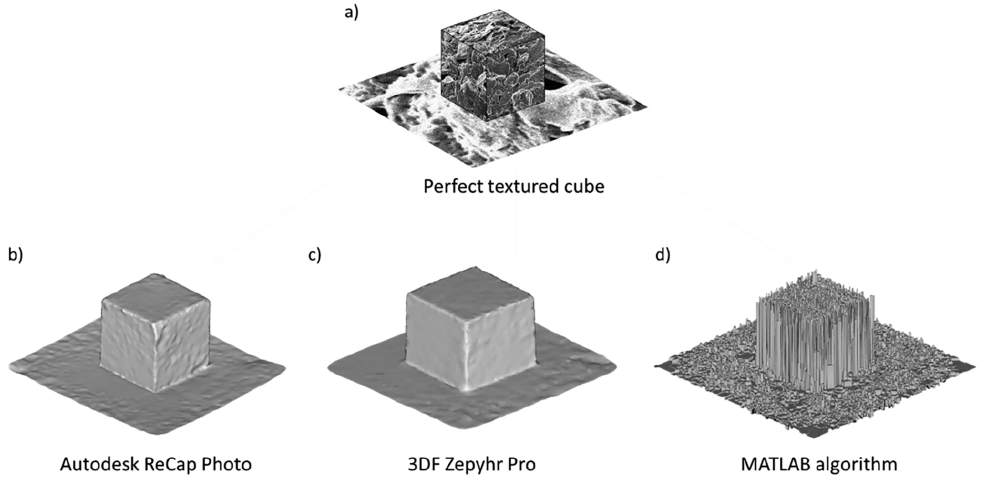

Figure 2. Photogrammetric 3D surface reconstructions from 36 images of a textured "perfect" cube on a base in (a) using the following software: (b) Autodesk ReCap Photo, (c) 3DF Zephyr Pro, and (d) a simulation algorithm created in MATLAB. Textures are not shown for the 3D reconstructions.

Nanofab HIM, which is equipped with an add-on SIMS system (therefore called "HIM-SIMS" instrument).[7] The primary beam (He^+ or Ne^+) is produced in a Gas Field Ion Source (GFIS) which consists of a cryogenically cooled sharp tip having an apex formed by only three atoms ("trimer"), acting as an ion source.[6] He (or Ne) atoms adsorbing on the tip are extracted and ionized by the high electric field applied between the tip and an extraction electrode. The ion beam is directed downward through the column to the sample. When impinging on the sample, the ions generate SE's emitted from the extreme surface, providing a high surface sensitivity. A spatial resolution of down to 0.5 nm is achieved using He^+.[7]

2.3. Photogrammetric 2D SE Image Acquisition. For 3D reconstruction using photogrammetry, 2D SE images were taken at well-defined positions, i.e., rotation and tilt angles of the stage allowing to record images all around the ROI (Figure 1a). This rotation of the stage is equivalent to a circular movement of the (He^+) source and the Everhart-Thornley (ET) detector around the ROI (Figure 1b). Optimal results were obtained by using a series of image acquisitions at a specific polar angle with respect to the sample surface (e.g., 45°) with small 10° stage rotation steps (in total 36 images for a complete turn). A series with another polar angle (e.g., 36°, equivalent to 54° stage tilt) at larger 30° rotation steps (in total 12 images) can be acquired in addition, because this can improve the reconstruction in certain cases,[18] where features located at slight overhangs of the ROI could not be registered at a 45° polar angle.

For both soil microaggregates, SE images were acquired with a 20 keV He^+ ion beam of 0.5 pA for a frame of 1024 × 1024 pixels using an average of 4 lines at 10 μs/pixel (Field of View (FOV) of 20 μm for the SE image series). The first presented soil microaggregate was reconstructed using 39 SE images (image acquisition every 15° at 45° tilt and every 24° at 54° tilt) and the second one using 35 SE images (image acquisition every 10° at 45° tilt).

https://doi.org/10.1021/acs.est.1c02971
Environ. Sci. Technol. 2021, 55, 9384−9393

2.4. Photogrammetric 3D SE Reconstruction. Three-dimensional reconstructions presented here were obtained using the software Autodesk ReCap Photo,[32] but were also reconstructed with 3DF Zepyhr Pro[33,34] for testing and comparison purposes. In Autodesk, images are simply implemented without having the possibility to play on internal parameters and influence on the final result. In 3DF Zephyr Pro, the reconstruction is done step-by-step by the user, i.e., search for features, matches in images, alignment of the camera positions, reconstruction of a dense point cloud, formation of a mesh, and finally addition of a colored texture.[34] Additionally, internal camera parameters (focal length, distortion, and optical center) can be implemented or chosen to be determined automatically.[35] In both software packages, the outcome is a textured 3D model which can be studied at all possible angles and magnifications.

For the first soil microaggregate, in total 24 906 data points were created ("vertices"), while for the second one, 55 094 vertices were reconstructed.

2.5. Ground Truth Comparison. In order to have an enhanced estimation of the reconstruction accuracy in general and potential issues related to the reconstruction process, a simplified mathematical algorithm for 3D reconstruction from 2D images was created in MATLAB proceeding in a comparable way step-by-step for the 3D reconstruction as for the commercial solutions. However, the fundamental difference between the algorithm and the commercial software is that the exact positions of the cameras are implemented by the user while for the commercial solutions a camera position estimation is performed.

Reconstructions of a cube were performed for the commercial software and the simulation algorithm and compared to the "perfect" cube ("ground truth comparison"). Therefore, a virtual cube was created in a 3D space and in total 36 images were taken around it at defined "camera" positions (45° polar angle and 10° azimuthal rotation step). The cube surface was textured to ensure a high amount of features and therefore to simplify the reconstruction process. The images were implemented into the simulation algorithm and both commercial software (Autodesk ReCap Photo and 3DF Zephyr Pro) to create a 3D model (Figure 2). In order to determine potential size-related shrinkages of the reconstructed structures, a cuboid was aligned to their shape. The cuboid height, length, and width were determined, while the deviation from the length and width from the cuboid height were calculated in %. The deviations using Autodesk ReCap Photo were 1.5% for the cuboid length and 2.5% for the width and using 3DF Zephyr Pro 25.1% (length) and 24.3% (width). The reconstruction using the simulation algorithm, though presenting a high amount of surface noise, gave an overall close to 0% deviation for both length and width.

The relatively high deviations for the commercial software can be explained in this case by an erroneous camera position estimation leading to local shrinkages and distortions in the 3D reconstructions, while the exact camera positions were implemented into the simulation algorithm. Structural deformations during the noise reduction and mesh reconstruction processes can not be excluded as well. However, in general the commercial software provides a more efficient and practical solution than the created simulation algorithm. Satisfactory 3D reconstructions with appropriate noise reduction, sharp edges, and smooth mesh reconstruction were obtained for both Autodesk ReCap and 3DF Zephyr Pro in less than 15 min, while the simulation algorithm needs approximately 1 h for the reconstruction and a smooth mesh creation still remains challenging due to the high amount of surface noise. Additionally, during the acquisition of serial SE images in the HIM around a ROI, a recentering of the sample stage onto the ROI is done resulting in a slight deviation from the actually designated "camera" positions of the SE image series. However, the MATLAB algorithm requires an exact implementation of the "camera" positions. Therefore, for SE images a "camera" position estimation as performed in the commercial solutions is still necessary to obtain a meaningful 3D reconstruction.

In summary, the commercial software provides satisfactory and high-quality 3D models, but possible local distortions due to an inaccurate camera position estimation should still be kept in mind. The resulting 3D reconstructions are available in the Supporting Information section.

2.6. Secondary Ion Mass Spectrometry (SIMS). Two different SIMS systems were used in the two presented analyses to take advantage of their unique capabilities. Before the analyses, the samples were covered by a 15 nm gold coating to reduce the charging effect during HIM-SIMS or NanoSIMS 50L acquisitions.

In the first case, the HIM add-on SIMS system (mentioned in 2.2) was used to allow in situ chemical imaging of the microaggregate's mineral phase at an ultrahigh spatial resolution. After imaging with HIM, we inserted the retractable secondary ion extraction box between the GFIS column and the sample and performed analytical SIMS measurements. Secondary ions were collected and transferred to the magnetic sector SIMS analyzer where up to four masses can be analyzed simultaneously.[8] A spatial resolution in SIMS imaging mode of sub 20 nm is reached for both, positive and negative ions, and a mass resolution of $m/\Delta m \approx 400$. The Ne^+ primary beam at normal incidence (25 keV, 2.5 pA) was used due to higher sputtering yields than with He^+ and therefore enhanced secondary ion signals,[36] while the secondary ions ^{23}Na, ^{24}Mg, and ^{39}K were imaged in 512 × 512 pixels at 5 ms/pixel (FOV 25 μm).

Second, a CAMECA NanoSIMS 50L, offering a poorer lateral resolution (50 nm)[37] than the HIM-SIMS (<20 nm), but a higher mass resolution for resolving compounds of organic carbon and nitrogen by depicting the distribution of specific isotopes (^{12}C, ^{13}C, ^{14}N, ^{15}N)[31] prone to mass interferences, was employed.

The Cs^+ ion beam (16 keV, 2 pA) of the NanoSIMS 50L instrument was used to image the spatial distribution of OM and mineral phases (256 × 256 pixels, 1 ms/pixel, sum over 65 planes per image, FOV 15 μm) by recording the negatively charged clusters $^{12}C^{12}C^-$, $^{12}C^{13}C^-$, $^{12}C^{14}N^-$, $^{12}C^{15}N^-$, and $^{27}Al^{16}O^-$ simultaneously at appropriate mass resolving power.

Thus, the choice of the HIM-SIMS instrument is motivated by the exploration of the spatial resolution to elucidate the soil mineral phase, whereas the NanoSIMS 50L thanks to its mass resolution and in combination with HIM offers an effective tool to study in depth OM distribution on mineral surfaces.

2.7. 4D Reconstruction. The SIMS images were projected onto their corresponding 3D SE surface representation using MeshLab.[38] MeshLab is a free and open source software for 3D visualization and analysis. Mutual points between the 2D SIMS image and the 3D SE representation were chosen manually ("2D-3D correspondences").[39] The 2D SIMS image was then aligned to the 3D SE representation with respect to

https://doi.org/10.1021/acs.est.1c02971
Environ. Sci. Technol. 2021, 55, 9384−9393

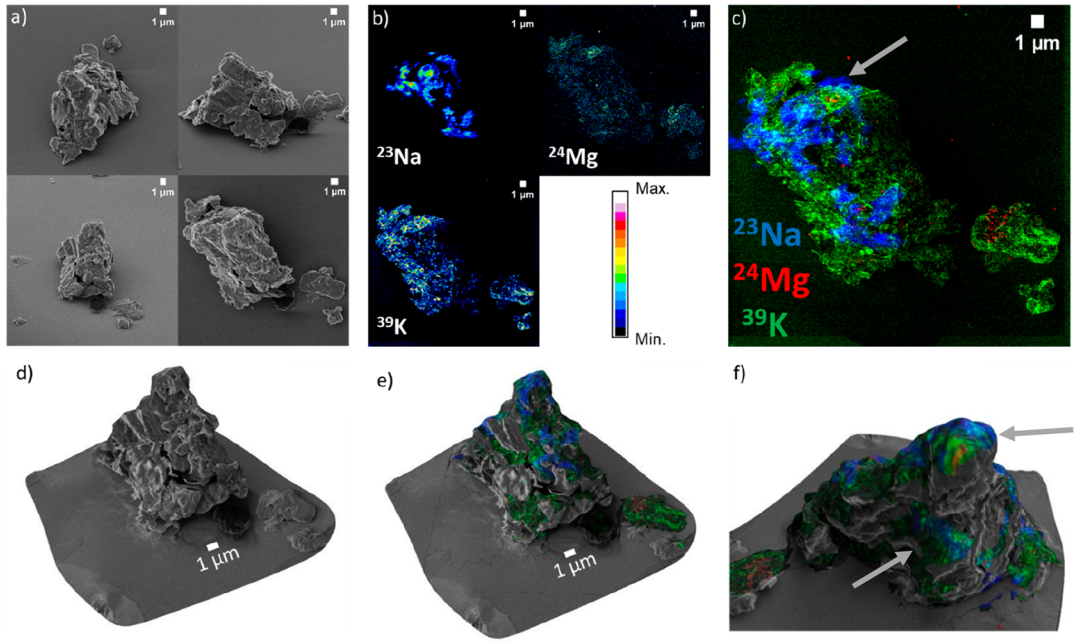

Figure 3. Workflow for a 4D reconstruction of a soil microaggregate. (a) Exemplary SE images: the upper images were acquired at 45° polar angle (45° stage tilt), while the rotation angles were 0° (top left) and 90° (top right). The lower left image corresponds to 36° polar angle (54° stage tilt) and 168° rotation and the lower right image was taken at normal incidence with respect to the wafer (i.e., polar angle 90°, stage tilt 0°). (b) SIMS images of ^{23}Na, ^{24}Mg, and ^{39}K. The scale bar indicates the secondary ion signal intensity for each mass. c) RGB SIMS composite image (Blue: ^{23}Na, Red: ^{24}Mg, Green: ^{39}K). d) 3D reconstruction of 39 SE images. (e) Projection of the RGB SIMS image from (c) onto the 3D SE representation from (d). In (d) and (e) the 3D, respectively, 4D model are shown at a view from a polar angle of 45°. (f) Zoomed view on the 4D reconstruction with an azimuthal rotation of 180° with respect to the view in (e). The arrow in (c) points to parts of the microaggregate which seem to be adjacent, but are actually vertically split as indicated by the two arrows in (f).

these correspondences. The image was projected onto the 3D representation and a texture map was created. Black pixels from this texture were removed since no secondary ions were detected there. The SIMS texture map generated in MeshLab was added to the texture map created from the SE images during the 3D reconstruction with a transparency of typically 60%. Hence, the final textured 4D representation allows one to observe topographical information from HIM and chemical information from SIMS throughout the reconstruction. Parts from the 3D representation where no SIMS signal was acquired, e.g., below overhangs ("shadow effect") or simply not containing the analyzed ion species, remain with only the topography texture.

3. RESULTS AND DISCUSSION

3.1. Methodological Description of 4D Reconstruction. *3.1.1. 4D Reconstruction Workflow.* The 4D reconstruction process is demonstrated stepwise in Figure 3. 39 SE images acquired in a series were used for this. Textured 3D meshes and animations of the soil microaggregate are available in the Supporting Information (SI) section.

Figure 3a illustrates three exemplary SE images used for the 3D reconstruction process taken at different stage tilt and rotation angles, while the lower right SE image was taken in top view. The topographical architecture of the soil microaggregate is enlightened at an unprecedented spatial resolution. The SIMS analysis shown in Figure 3b,c indicates a heterogeneous distribution of the mapped sodium (^{23}Na), magnesium (^{24}Mg), and potassium (^{39}K) on the same particle, as indicators for the mineral phase.

The chemical RGB SIMS image (Figure 3c) aligned and projected onto the 3D SE representation (Figure 3d) provides for the first time to our knowledge, the full 4D surface reconstruction of a soil microaggregate (Figure 3e). Figure 3f shows the zoomed-in 4D reconstruction with a 180° azimuthal rotation with respect to the representation in Figure 3e.

3.1.2. Reconstruction Evaluation and Recommendations. The overall convexity of the microaggregate favored a successful 3D SE reconstruction. The rough and inhomogeneous surface of the microaggregate (Figure 3a) facilitated the detection of a high number of features supporting the image matching process. However, pronounced topography is lacking on the Si wafer itself, which would favor in this case a flat representation of the wafer. Since features are missing on the Si wafer the software needs to interpolate the mesh over a long distance creating artifacts and erroneous unevenness on its surface.

As the working principle of common photogrammetry 3D reconstruction algorithms is based on feature detection and matching between images, ROI's with rough and inhomogeneous surfaces are rather easy to reconstruct. However, objects with a very smooth and featureless surface present a challenge for reconstruction using common photogrammetry software since the amount of detected and matched features in the images is extremely low.[20,40] Typically, images of macroscopic objects taken with an optical camera show a higher amount of detected features than SE images. The discrepancy of feature detection and matching amounts between optical and SE images is mainly due to the high amount of noise in SE images which can obstruct the feature detection algorithms considerably. Noise in the SE images can be reduced by increasing the number of average lines or frames during the image acquisition. Nevertheless, a compromise between time investment and improving image quality needs to be found.

https://doi.org/10.1021/acs.est.1c02971
Environ. Sci. Technol. 2021, 55, 9384−9393

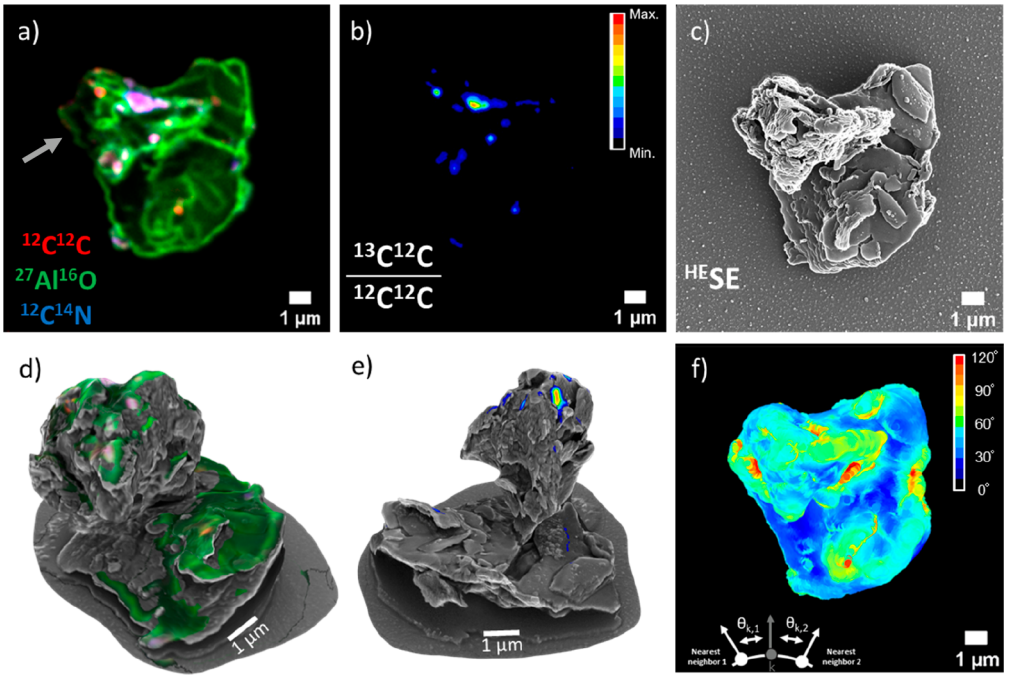

Figure 4. Topographic and compositional analysis of a soil microaggregate. (a) RGB SIMS image of the organic carbon and nitrogen compounds $^{12}C^{12}C$ (in red) and $^{12}C^{14}N$ (blue), and $^{27}Al^{16}O$ (green) representing the mineral phase of the microaggregate. The arrow points to an area with reduced secondary ion intensity resulting presumably from a restricted acceptance angle of the spectrometer. (b) Isotopic $^{13}C^{12}C/^{12}C^{12}C$ ratio image showing the areas enriched in ^{13}C. The scale bar indicates the ratio pixel intensity. (c) HIM 2D SE image in top view. The reaction of the implanted cesium with air led to the formation of little bubbles on the wafer of the Cs^+ irradiated area. (d) 4D surface reconstruction (side view at 45° polar angle) resulting from the overlay of the photogrammetric 3D SE reconstruction using 35 SE images and the RGB SIMS image from (a). (e) 4D surface reconstruction where the colored areas show the isotopic enrichment information from (b) (side view at 45° polar angle, 180° azimuthal rotation with respect to (d). (f) Visualization of the local particle's curvature determined from the average angles between the surface normal vectors of the considered nearest neighbors (top view). The curvature of the wafer was arbitrarily set to 0° in this representation. The scheme on the lower left side of (f) illustrates the determination of the local curvature: nearest neighbors i (1 and 2 in the scheme) of a 3D point k (in gray) are located first, then angles between their normal vectors $\theta_{k,i}$ and finally their average value is calculated.

Preliminary 3D SE reconstruction tests showed that on average at least 60 features should be detected per image and around 40 matches for consecutive images should be found to allow a meaningful 3D SE reconstruction. For this reconstruction, on average 124 features were detected per SE image with on average 87 matches for sequential images in the 45° tilt acquisition series. If no or only a few features are detected throughout the ROI in the SE images, then the photogrammetry software will interpolate 3D points arbitrarily during the mesh reconstruction process resulting in an erroneous 3D SE representation. Hence, a high amount of features on the ROI and minor defects surrounding the ROI (i.e., on the wafer) will simplify the feature detection and leads to a more authentic 3D SE reconstruction.

It is worth noticing that, although the number of detected and matched features might be high, camera positions can be estimated inaccurately leading to a distorted result. In this case, additional trials with manual changes of the internal camera parameters, i.e., focal length, lens distortion, and optical center might help to improve the result.

In fact, while common photogrammetry software is specialized in 3D reconstruction from optical camera images, no information about camera intrinsics is stored in SE images, i.e., focal distance, optical center, and lens distortion.[19] Therefore, an automatic calibration algorithm estimates the camera intrinsics and positions (i.e., the positions where the images were taken with respect to the object) from feature detection and matching among the images.[35] Hence, even if a high number of features were detected and matched in an image series, the resulting 3D SE representation can still be distorted or erroneous due to an incorrect determination of camera intrinsic parameters.

In the case of the 3D SE reconstruction in Figure 3d, the "camera" positions estimated by Autodesk ReCap Photo were generally in accordance with the designated "camera" positions defined by the stage tilt and rotations steps, hence an indicator for an authentic 3D reconstruction.

3.1.3. Advantages of 3D SE and SIMS Overlay. In Figure 3e, the SIMS image covers only areas of the particle where secondary ions were detected. Hence, small overhangs or areas, where no elements of interest could be detected, although subjected to the primary Ne^+ beam, e.g., the wafer or surrounding particles, remain in the SE texture exclusively. This can be well observed in Figure 3f: the top and some of the lower parts of the particle are covered with the SIMS information (indicated with two arrows), while the areas in-between present only the SE texture.

Thus, the superposition of the 3D SE model and SIMS images provides a more complete picture of an ROI compared to simple 2D images, because this representation of the SIMS information takes into account vertical ROI offsets. For instance, while in Figure 3c for the area indicated by the arrow, it seems that the secondary ion signal originates from adjacent parts of the microaggregate, in Figure 3f it becomes visible that this area is actually vertically split in space by areas

https://doi.org/10.1021/acs.est.1c02971
Environ. Sci. Technol. 2021, 55, 9384−9393

(marked with two arrows), where no secondary ions were detected due to their concave topography.

3.2. Applications of 4D Reconstruction for SIMS Analyses. *3.2.1. Imaging and Surface Reconstruction.* A more fundamental topographic analysis enabled by the 4D reconstruction is demonstrated on a 3D architecture of a soil microaggregate imaged using 35 HIM SE images superposed with the analytical information acquired with the NanoSIMS 50L. For the 3D SE reconstruction (available in the SI), on average 219 features were detected per SE image and 145 matches were found from one image to the next one in the series, indicating a more than sufficient amount of reconstructed 3D points for the surface model (see discussion in section 3.1.2). The reaction of the implanted cesium with air after the NanoSIMS 50L measurement[41] led to the creation of numerous spots all around the microaggregate, firmly supporting the feature detection and matching process on the wafer. Moreover, most of the "camera" positions calculated by the photogrammetry software were in agreement with the chosen stage tilt and rotation steps, i.e., no major distortions in the 3D model due to erroneous "camera" position estimations are assumed.

Analytical SIMS maps of $^{27}Al^{16}O$ (mineral phase), respectively $^{12}C^{12}C$ and $^{12}C^{14}N$ (organic matter), were acquired and combined into a single RGB image in Figure 4a (red: $^{12}C^{12}C$, green: $^{27}Al^{16}O$, blue: $^{12}C^{14}N$). The reduced secondary ion intensity on the upper left corner of the particle (marked with an arrow) in Figure 4a results presumably from a shadowing effect due to a restricted acceptance angle of the spectrometer.[18]

The $^{13}C^{12}C/^{12}C^{12}C$ ratio image was created and thus demonstrates areas enriched in ^{13}C on the surface of the microaggregate (Figure 4b).

A HIM SE acquisition was taken in the top view, i.e., at a normal incidence of the primary beam with respect to the wafer (Figure 4c). The formation of the above-mentioned spots spread on the wafer all around the microaggregate emerging after the Cs^+ irradiation can be well observed here.

4D surface reconstructions were compiled by performing the alignment and overlay between the reconstructed 3D SE model and first the RGB SIMS image (Figure 4d) and second the isotopic ratio information (Figure 4e). The representation of the SIMS information on the 3D SE surface model in Figure 4d,e, as discussed in section 3.1.3, represents an enhanced visualization of the SIMS information as the vertical distance between all the OM hotspots becomes visible.

3.2.2. Organic Matter 3D Distribution. On the basis of the 3D architecture model of the soil microaggregate a topographical analysis in relation to the distribution of the OM was performed. With this investigation, we intend to trace the inherent OM and the new OM, coming from isotopic labeling experiments, to better understand biogeochemical processes at the microscale.[37]

For the analysis of the 4D model, the surface curvature was used as a metric for topography variations,[42] since it allows one to characterize the microaggregate's topographical structure and distinguish between plain surfaces and local slopes, resulting from, e.g., micropores, cracks, or edges, and relate this information directly to the local chemical composition. The reconstructed surface model from Figure 4d was imported as a color-coded point cloud into MATLAB.

For the reconstructed microaggregate (counting only the reconstructed soil material and neglecting the wafer), a total surface of 197 μm^2 and a density of around 230 data points per μm^2 were measured. Hence, to estimate the local curvature for each 3D data point of the point cloud, 230 nearest neighbors for each 3D point were first determined. Additionally, by inspection of the point cloud, the consideration of 230 nearest neighbors per 3D point were assumed to be reasonable for a curvature calculation considering the density of the reconstructed point cloud and the overall microaggregate model size. Local surface normal vectors were computed and stored for each 3D point.

The local curvature σ_k for each 3D point k was then calculated with respect to its closest neighbors using the following definition:[42]

$$\sigma_k := \frac{1}{N}\sum_{i=1}^{N}\theta_{k,i} \tag{1}$$

where N is the number of considered nearest neighbors (here 230) and $\theta_{k,i}$ is the angle between the normal vector of 3D point k and the normal vector of the i^{th} nearest neighbor. In other words, the local curvature σ_k represents thus the average angle between the normal vector in the 3D point k and all the nearest neighbors' normal vectors. A color-coded visualization of the microaggregate's surface curvature is shown in the top view in Figure 4f.

The chemical information from the overlay of the 3D SE model and the RGB SIMS image (red: $^{12}C^{12}C$, green: $^{27}Al^{16}O$, blue: $^{12}C^{14}N$) was then associated with each 3D data point, in addition to the curvature information. The grayscale information from the SE was excluded for this analysis. The curvature σ_s for a specific ion species s (e.g., $^{12}C^{12}C$) is then defined as the average of all the curvatures of 3D points containing the ion species s:

$$\sigma_s := \frac{1}{n}\sum_{j=1}^{n}\sigma_{s,j} \tag{2}$$

where n is the number of all the 3D data points containing the ion species s and $\sigma_{s,j}$ is the curvature of a 3D point j, calculated previously using (1), containing chemical information on species s. For the 3D points containing $^{27}Al^{16}O$, we took only plain areas of the microaggregate into account to estimate the "background" curvature for the mineral phase, distributed throughout the entire microaggregate. The $^{27}Al^{16}O$ distribution nicely represents the clay minerals in such a sample, and thus the major component of these soil microaggregates. We found that the curvature $\sigma^{^{27}Al^{16}O}$ for all the 3D data points containing $^{27}Al^{16}O$ (mineral phase) for plain areas corresponded to 14.1°, while for 3D points presenting $^{12}C^{12}C$ and $^{12}C^{14}N$, showing OM distributed as hotspots, the curvatures $\sigma^{^{12}C^{12}C}$ and $\sigma^{^{12}C^{14}N}$ were 37.4° and 38.5°, respectively. Interestingly, by performing the same analysis on the 4D model from Figure 4e, the areas in the microaggregate enriched with ^{13}C, presented a very similar average curvature value $\sigma^{^{13}C^{12}C/^{12}C^{12}C}$, namely 37.2°. The standard deviation of the curvature for $^{27}Al^{16}O$ was around 4° and for the OM compounds close to 10° in each case.

Thus, for this soil microaggregate, the OM deposited on areas characterized on average by almost triple of the surface curvature compared to mineral plains of the microaggregate. This demonstrates that in the case of the studied microaggregate areas with low topography but also areas with high topography (highly curved), e.g. edges, in the microaggregate's mineral phase show no freshly added OM as indicated by the

https://doi.org/10.1021/acs.est.1c02971
Environ. Sci. Technol. 2021, 55, 9384−9393

absence of ^{13}C. Isotopically enriched OM, originating from the amendment of ^{13}C enriched substrates in the incubation experiment, were associated with the microaggregate surfaces on average in areas with a very similar surface curvature as the preexisting OM in the microaggregate.

Results show that topography and chemical composition are drivers of soil OM distribution which is in accordance with the findings of previous studies on soil organo-mineral structures.[37]

3.3. An Imaging Approach Extending Our Conceptual Understanding of Organo-Mineral Associations. *3.3.1. Benefits for Soils.* The microaggregate in Figure 3e, originating from the wet deposition sample preparation procedure, demonstrates the architecture of soil microaggregates as composed of distinct minerals with different chemical composition at a nonprecedent spatial resolution. This high spatial resolution is crucial to correlate the fate of OM with the buildup of microaggregates and thus mineral-associated OM. The mineral skeletal structure of the microaggregate and thus the mineral phase is represented by the ^{23}Na, ^{24}Mg, and ^{39}K distributions (Figure 3b). The spatial distribution of sodium, magnesium, and potassium demonstrates distinctly different microscale patterns that clearly resemble the different primary and pedogenic minerals that make up the microaggregate. As illite, chlorite, quartz, and kaolinite are the main mineral constituents of this soil material (data not shown), we demonstrate that the resembled structures represent these clay-sized minerals differentiated by the distinct proportion of the measured elements.

For the analysis of the microaggregate obtained by dry sieving, the 3D SE surface reconstruction in Figure 4d and the corresponding $^{27}Al^{16}O$ (Figure 4a) SIMS information greatly enhances the view on the soil microstructure as it correlatively visualizes the soil mineral phase and its positioning in the 3D arrangement of the microaggregate architecture. By combining the demonstrated correlation with the microscale distribution of OM phases from chemical images representing carbon and nitrogen, the 3D reconstruction allows one to differentiate between specific mineral particles vs microscale physical structure (surface curvature) for the association of OM with the mineral surfaces.

Thus, the demonstrated approach offers the potential to elucidate how chemical surface properties and physical microscale soil structure foster the formation of mineral associated OM. It allows one to correlate distinct soil mineral species with their specific function in the context of the microaggregate architecture at the relevant scale for biogeochemical processes.

3.3.2. Perspectives. The methodology of 4D surface reconstruction combining 3D topography and 1D analytical information obtained by EM and SIMS has been extended and applied successfully in soil biogeochemistry. In contrast to a traditional 2D image, our representation shows the specimen in its entirety and its surface topography information can be used to correlate it directly with the local chemical composition, which allows one to greatly enhance the conceptual view on soil microaggregate architecture and function. Thus, we were able to demonstrate that organo-mineral associations mainly form at medium curvatures pointing to specific surface properties of microaggregates that foster the formation of mineral-associated OM. Both inherited and freshly added OM is recovered at comparable topographic positions on the microaggregate.

The established approach provides the framework for detailed microstructural analyses of biogeochemical samples, reaching from soils to sediments. For applications in soil biogeochemistry, 4D reconstructions offer the possibility to delineate topographic (e.g., surface curvature) and chemical properties of mineral and organic particles including microaggregates that determine the cycling and distribution of for instance organo-mineral associated OM or microbial OM at the relevant process scale.

Finally, 4D reconstruction is not limited to the mentioned analysis techniques (HIM-SIMS, HIM-NanoSIMS 50L) but can be used more generally for correlative microscopy combining 3D topography (e.g., optical microscopy, electron microscopy) and analytical information (e.g., time-of-flight SIMS, X-ray photoelectron, or Raman spectroscopy) for mapping the distribution of chemical components inside the sample.

■ ASSOCIATED CONTENT

Supporting Information

The Supporting Information is available free of charge at https://pubs.acs.org/doi/10.1021/acs.est.1c02971.

Ground truth comparison, including File S1, 3D reconstruction of the cube with Autodesk ReCap Photo (.stl); File S2, 3D reconstruction of the cube with 3DF Zephyr Pro (.stl); and File S3, 3D reconstruction of the cube with the MATLAB simulation algorithm (.stl); *methodological description of 4D reconstruction*, including File S4, video (.avi format) of rotating 3D SE representation of the soil microaggregate; File S5, 3D SE model of the soil microaggregate (.obj) with corresponding texture (.jpg) and material file (.mtl); File S6, video (.avi) of rotating 4D reconstruction of the soil microaggregate; and File S7, 4D model of the soil microaggregate (.obj) with corresponding texture (.jpg) and material file (.mtl); and *applications of 4D reconstruction for SIMS analyses*, including File S8, video (.avi format) of rotating 3D SE representation of the soil microaggregate; File S9, 3D SE model of the soil microaggregate (.obj) with corresponding texture (.jpg) and material file (.mtl); File S10, video (.avi) of rotating 4D reconstruction of the soil microaggregate (organic matter: 12C, 14N), File S11, 4D model of the soil microaggregate (.obj) with corresponding texture (.jpg) and material file (.mtl) (organic matter: 12C, 14N), File S12, video (.avi) of rotating 4D reconstruction of the soil microaggregate (ratio $^{12}C^{13}C/^{12}C^{12}C$), and File S13, 4D model of the soil microaggregate (.obj) with corresponding texture (.jpg) and material file (.mtl) (ratio $^{12}C^{13}C/^{12}C^{12}C$) (ZIP)

Description of the SI files (PDF)

■ AUTHOR INFORMATION

Corresponding Author

Alexander D. Ost − *Advanced Instrumentation for Nano-Analytics (AINA), Materials Research and Technology Department (MRT), Luxembourg Institute of Science and Technology (LIST), 4422 Belvaux, Luxembourg; University of Luxembourg, 4365 Esch-sur-Alzette, Luxembourg;* Present Address: Luxembourg Institute of Science and Technology (LIST), L-4422 Belvaux, Luxembourg.;

https://doi.org/10.1021/acs.est.1c02971
Environ. Sci. Technol. 2021, 55, 9384−9393

orcid.org/0000-0002-7465-2541; Phone: +352 275 888 3550; Email: alexander.ost@list.lu

Authors

Tianyi Wu − *Soil Science, TUM School of Life Sciences, Technical University of Munich, 85354 Freising, Weihenstephan, Germany*

Carmen Höschen − *Soil Science, TUM School of Life Sciences, Technical University of Munich, 85354 Freising, Weihenstephan, Germany*

Carsten W. Mueller − *Department of Geosciences and Natural Resource Management Geography, University of Copenhagen, 1350 Copenhagen, Denmark*

Tom Wirtz − *Advanced Instrumentation for Nano-Analytics (AINA), Materials Research and Technology Department (MRT), Luxembourg Institute of Science and Technology (LIST), 4422 Belvaux, Luxembourg*

Jean-Nicolas Audinot − *Advanced Instrumentation for Nano-Analytics (AINA), Materials Research and Technology Department (MRT), Luxembourg Institute of Science and Technology (LIST), 4422 Belvaux, Luxembourg;* orcid.org/0000-0002-4966-7653

Complete contact information is available at: https://pubs.acs.org/10.1021/acs.est.1c02971

Notes

The authors declare no competing financial interest.

■ ACKNOWLEDGMENTS

The authors gratefully acknowledge support by the Luxembourg National Research Fund (FNR) under grant no. INTER/DFG/17/11779689, and the Deutsche Forschungsgemeinschaft (DFG) through grant no. HO 5121/1-1.

■ REFERENCES

(1) Wirtz, T.; Philipp, P.; Audinot, J. N.; Dowsett, D.; Eswara, S. High-resolution high-sensitivity elemental imaging by secondary ion mass spectrometry: From traditional 2D and 3D imaging to correlative microscopy. *Nanotechnology* **2015**, *26*, 434001.

(2) Vollnhals, F.; Audinot, J. N.; Wirtz, T.; Mercier-Bonin, M.; Fourquaux, I.; Schroeppel, B.; Kraushaar, U.; Lev-Ram, V.; Ellisman, M. H.; Eswara, S. Correlative Microscopy Combining Secondary Ion Mass Spectrometry and Electron Microscopy: Comparison of Intensity-Hue-Saturation and Laplacian Pyramid Methods for Image Fusion. *Anal. Chem.* **2017**, *89*, 10702−10710.

(3) Hollricher, O.; Schmidt, U.; Breuninger, S. RISE Microscopy: Correlative Raman-SEM Imaging. *Microsc. Today* **2014**, *22*, 36−39.

(4) Reddick, L. E.; Alto, N. M. Correlative light and electron microscopy (CLEM) as a tool to visualize microinjected molecules and their eukaryotic sub-cellular targets. *J. Visualized Exp.* **2012**, 1.

(5) Moore, K. L.; Lombi, E.; Zhao, F. J.; Grovenor, C. R. M. Elemental imaging at the nanoscale: NanoSIMS and complementary techniques for element localisation in plants. *Anal. Bioanal. Chem.* **2012**, *402*, 3263−3273.

(6) Wirtz, T.; De Castro, O.; Audinot, J. N.; Philipp, P. Imaging and Analytics on the Helium Ion Microscope. *Annu. Rev. Anal. Chem.* **2019**, *12*, 523−543.

(7) Hlawacek, G.; Gölzhäuser, A. *Helium Ion Microscopy*; Springer Nature: Basel, Switzerland, 2016 DOI: 10.1007/978-3-319-41990-9.

(8) Dowsett, D.; Wirtz, T. Co-Registered in Situ Secondary Electron and Mass Spectral Imaging on the Helium Ion Microscope Demonstrated Using Lithium Titanate and Magnesium Oxide Nanoparticles. *Anal. Chem.* **2017**, *89*, 8957−8965.

(9) Williams, P. Secondary Ion Mass Spectrometry. *Annu. Rev. Mater. Sci.* **1985**, *15*, 517−548.

(10) Zalm, P. Secondary ion mass spectrometry. *Vacuum* **1994**, *45*, 753−772.

(11) van der Heide, P. *Secondary Ion Mass Spectrometry*; John Wiley & Sons, Inc.: Hoboken, NJ, 2014 DOI: 10.1002/9781118916780.

(12) Gillen, G.; Fahey, A.; Wagner, M.; Mahoney, C. 3D molecular imaging SIMS. *Appl. Surf. Sci.* **2006**, *252*, 6537−6541.

(13) Wucher, A.; Cheng, J.; Winograd, N. Protocols for Three-Dimensional Molecular Imaging Using Mass Spectrometry. *Anal. Chem.* **2007**, *79*, 5529−5539.

(14) Koch, S.; Ziegler, G.; Hutter, H. ToF-SIMS measurements with topographic information in combined images. *Anal. Bioanal. Chem.* **2013**, *405*, 7161−7167.

(15) Terlier, T.; Lee, J.; Lee, K.; Lee, Y. Improvement of the Correlative AFM and ToF-SIMS Approach Using an Empirical Sputter Model for 3D Chemical Characterization. *Anal. Chem.* **2018**, *90*, 1701−1709.

(16) Fleming, Y.; Wirtz, T.; Gysin, U.; Glatzel, T.; Wegmann, U.; Meyer, E.; Maier, U.; Rychen, J. Three dimensional imaging using secondary ion mass spectrometry and atomic force microscopy. *Appl. Surf. Sci.* **2011**, *258*, 1322−1327.

(17) Akhtar, I.; Rehman, M. A.; Choi, W.; Kumar, S.; Lee, N.; Cho, S. J.; Park, H. H.; Park, K. H.; Seo, Y. Three-dimensional atomic force microscopy for ultra-high-aspect-ratio imaging. *Appl. Surf. Sci.* **2019**, *469*, 582−592.

(18) Vollnhals, F.; Wirtz, T. Correlative Microscopy in 3D: Helium Ion Microscopy-Based Photogrammetric Topography Reconstruction Combined with in situ Secondary Ion Mass Spectrometry. *Anal. Chem.* **2018**, *90*, 11989−11995.

(19) Eulitz, M.; Reiss, G. 3D reconstruction of SEM images by use of optical photogrammetry software. *J. Struct. Biol.* **2015**, *191*, 190−196.

(20) Gontard, L. C.; Schierholz, R.; Yu, S.; Cintas, J.; Dunin-Borkowski, R. E. Photogrammetry of the three-dimensional shape and texture of a nanoscale particle using scanning electron microscopy and free software. *Ultramicroscopy* **2016**, *169*, 80−88.

(21) Hartley, R.; Zisserman, A., Eds.; *Multiple View Geometry in Computer vision*, 2nd ed.; Cambridge University Press: Cambridge, 2004 DOI: 10.1017/CBO9780511811685.

(22) Peter Heng, B. C.; Chandler, J. H.; Armstrong, A. Applying close range digital photogrammetry in soil erosion studies. *Photogramm. Rec.* **2010**, *25*, 240−265.

(23) Spampinato, V.; Dialameh, M.; Franquet, A.; Fleischmann, C.; Conard, T.; Van Der Heide, P.; Vandervorst, W. A Correlative ToF-SIMS/SPM Methodology for Probing 3D Devices. *Anal. Chem.* **2020**, *92*, 11413−11419.

(24) Tisdall, J. M.; Oades, J. M. Organic matter and water-stable aggregates in soils. *J. Soil Sci.* **1982**, *33*, 141−163.

(25) Edwards, A. P.; Bremner, J. M. Microaggregates in Soils. *J. Soil Sci.* **1967**, *18*, 64−73.

(26) Six, J.; Conant, R. T.; Paul, E. A.; Paustian, K. Stabilization mechanisms of soil organic matter: Implications for C-saturation of soils. *Plant Soil* **2002**, *241*, 155−176.

(27) Totsche, K. U.; Amelung, W.; Gerzabek, M. H.; Guggenberger, G.; Klumpp, E.; Knief, C.; Lehndorff, E.; Mikutta, R.; Peth, S.; Prechtel, A.; Ray, N.; Kögel-Knabner, I. Microaggregates in soils. *J. Plant Nutr. Soil Sci.* **2018**, *181*, 104−136.

(28) Chenu, C.; Plante, A. F. Clay-sized organo-mineral complexes in a cultivation chronosequence: Revisiting the concept of the "primary organo-mineral complex,. *Eur. J. Soil Sci.* **2006**, *57*, 596−607.

(29) IUSS Working Group WRB. *World Reference Base for Soil Resources—A Framework for International Classification, Correlation, and Communication*; FAO: Rome, 2006. https://research.wur.nl/en/publications/world-reference-base-for-soil-resources-2006-a-framework-for-inte.

(30) Felde, V.; Schweizer, S. A.; Biesgen, D.; Ulbrich, A.; Uteau, D.; Knief, C.; Graf-Rosenfellner, M.; Kögel-Knabner, I.; Peth, S. Wet sieving versus dry crushing: Soil microaggregates reveal different physical structure, bacterial diversity and organic matter composition in a clay gradient. *Eur. J. Soil Sci.* **2021**, *72*, 810.

(31) Mueller, C.W.; Weber, P.K.; Kilburn, M.R.; Hoeschen, C.; Kleber, M.; Pett-Ridge, J., Advances in the analysis of biogeochemical interfaces. *NanoSIMS to Investigate Soil Microenvironments*; Elsevier Inc., 2013 DOI: 10.1016/B978-0-12-407685-3.00001-3.
(32) ReCap Photo—Photogrammetry Guide, 2017. https://help.autodesk.com/sfdcarticles/attachments/ReCap_Photo-Photogrammetry_Guide_V1.pdf (accessed June 15, 2021).
(33) 3DFLOW 3DF Zephyr—User Manual, 2013 http://3dflow.net (accessed June 15, 2021).
(34) Marčiš, M.; Fraštia, M. Photogrammetric Measurement of a Wooden Truss. *Slovak J. Civ. Eng.* **2018**, *26*, 1−10.
(35) De la Escalera, A.; Armingol, J. M. Automatic chessboard detection for intrinsic and extrinsic camera parameter calibration. *Sensors* **2010**, *10*, 2027−2044.
(36) Pillatsch, L.; Vanhove, N.; Dowsett, D.; Sijbrandij, S.; Notte, J.; Wirtz, T. Study and optimization of SIMS performed with He+ and Ne+ bombardment. *Appl. Surf. Sci.* **2013**, *282*, 908−913.
(37) Vogel, C.; Mueller, C. W.; Höschen, C.; Buegger, F.; Heister, K.; Schulz, S.; Schloter, M.; Kögel-Knabner, I. Submicron structures provide preferential spots for carbon and nitrogen sequestration in soils. *Nat. Commun.* **2014**, *5*, 2947.
(38) Cignoni, P.; Callieri, M.; Corsini, M.; Dellepiane, M.; Ganovelli, F.; Ranzuglia, G. *MeshLab: An Open-Source Mesh Processing Tool*; Scarano, V. I., De Chiara, R., Erra, U., Eds.; *Eurographics Ital. Chapter Conf.*, 2008: pp 129−136 DOI: 10.2312/LocalChapterEvents/ItalChap/ItalianChapConf2008/129-136.
(39) Sottile, M.; Dellepiane, M.; Cignoni, P.; Scopigno, R. Mutual Correspondences: an Hybrid Method for Image-to-Geometry Registration. Puppo, E., Brogni, A., De Floriani, L., Eds.; *Eurographics Ital. Chapter Conf.*, 2010: pp 80−88. 10.2312/LocalChapterEvents/ItalChap/ItalianChapConf2010/081-088.
(40) Kudryavtsev, A., 3D Reconstruction in Scanning Electron Microscope: from image acquisition to dense point cloud. *Signal and Image Processing*; Université Bourgogne: Franche-Comté, 2017.
(41) Miethe, K.; Gries, W.H.; Pöcker, A. Ion Deposition Effects in and Around Sputter Craters Formed by Cesium Primary Ions. Benninghoven, A., Colton, R. J., Simons, D.S., Werner, H. W., Eds.; Second. *Ion Mass Spectrom*. SIMS V Springer: Berlin/Heidelberg, 1986; pp 347−349 DOI: 10.1007/978-3-642-82724-2_92.
(42) Wilke, W. *Segmentierung und Approximation großer Punktwolken*; Technical University of Darmstadt, 2002. http://tuprints.ulb.tu-darmstadt.de/255/.

https://doi.org/10.1021/acs.est.1c02971
Environ. Sci. Technol. 2021, 55, 9384−9393